Faculty of Aerospace Engineering
Delft University of Technology

L.Z.F. van Rossum

MSc Thesis

Development of a numerical model for the Sumatra subduction zone constrained by satellite gravimetry

with special focus on gravity sensitivity studies

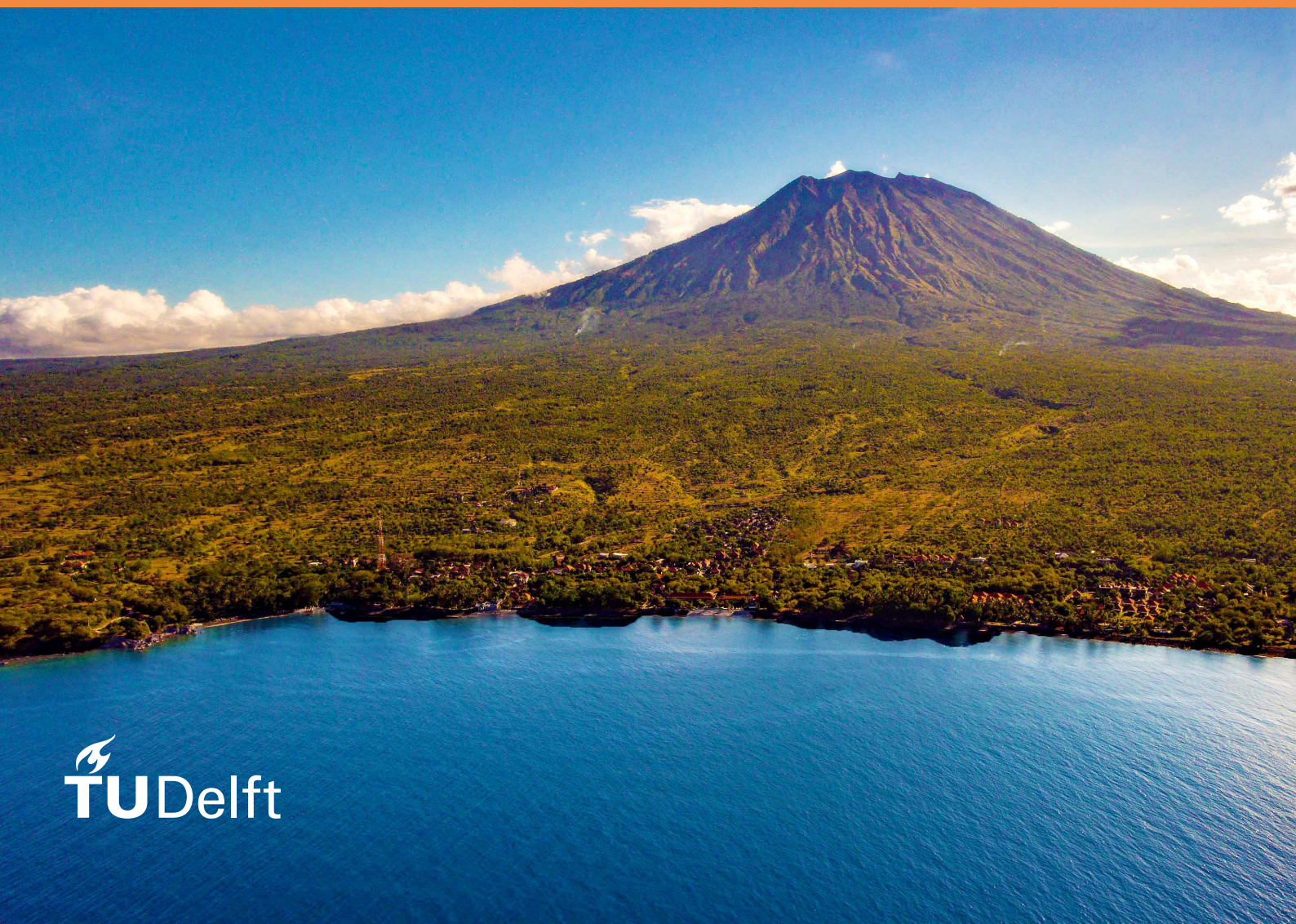

TU Delft

Development of a numerical model for the Sumatra subduction zone constrained by satellite gravimetry

with special focus on gravity sensitivity studies

Contributing to ESA 3D-Earth project

by

Leon Zhu Feng van Rossum

to obtain the degree of Master of Science,
at the Delft University of Technology,
to be defended publicly on Monday August 27, 2018 at 14:00.

Student number:	4087259	
Printed:	August 20, 2018	
Thesis committee:	Prof. Dr. L. L. A. Vermeersen	TU Delft, committee chairman
	Dr. Ir. B. C. Root	TU Delft, daily supervisor
	Dr. Ir. W. van der Wal	TU Delft, co-supervisor
	Dr. Ir. D. B. T. Broerse	TU Delft, committee
	Dr. Ir. J. M. Kuiper	TU Delft, committee

An electronic version of this thesis is available at http://repository.tudelft.nl/.

TU Delft

esa
European Space Agency

Preface

On the cover image the volcano Mt. Agung is displayed. Mt. Agung is located on the volcanic arc of the Sumatra subduction zone. Volcanoes and earthquakes are the two main phenomena through which we, humans at the Earth's surface, experience and are reminded of those deeper processes in the Earth. For this reason a volcano was chosen to be on the cover.

Continuing the Dutch legacy of researching the Sumatra subduction zone

Back in Dutch colonial times of the 1930's, Prof. Vening Meinesz boarded the submarine Hr.Ms. K XIII of the *Dutch East Indian Naval Forces* in Amsterdam, see Figure 1. He spent six months on the submarine and was able to make gravity measurements of the Sumatra subduction zone and beyond. "*Why was a submarine used?*" one might wonder, this was done to avoid disturbances from wave motion (Lowrie, 2007). As can be said about all professors, Prof. Meinesz was very ambitious, and therefore he wanted to maximize the number of measurements. Those measurements were taken while being submerged, which happened twice by day, and twice by night. Each measurement took about two hours. One can imagine that his crew of 18 had to endure six long months of hard work and little sleep.

Looking back on his demanding routine in the Indonesian Archipelago, Meinesz (1931) recalled: *"I can say that the spirit of companionship and comradeship never suffered, and I may record, with gratitude, that I received most helpful assistance from the Commander, Lieut. Mante, who submerged* ***every time*** *that the research made it desirable."*

I, the author of this master thesis, feel honoured to continued and advanced the work of this noble scientist, and I have done so in the same spirit of companionship, comradeship and with daily gratitude.

For me, it has been nine long months of hard work and little sleep, the latter only sometimes. I didn't work while being submerged, on the contrary, I worked while being elevated. Elevated, almost every single day, to the ninth floor of the beautiful faculty of Aerospace Engineering. Notwithstanding, I have submerged myself every time that the research made it desirable. Furthermore, I have tried to submerge myself every time to avoid disturbances from non-thesis motion.

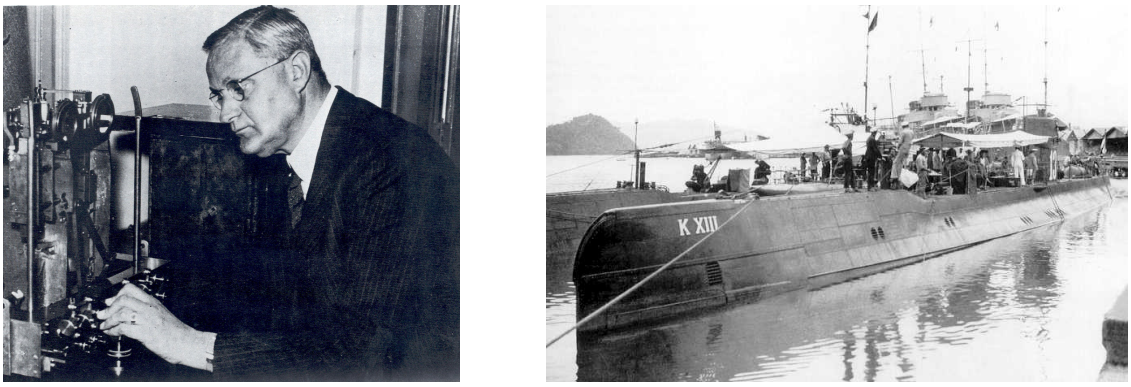

Figure 1: 1930's mission of Prof. Meinesz. Left: Vening Meinesz with his gravimeter (*from: the Utrecht University archive*). Right: Hr.Ms. K XIII in Surabaya (*from: DutchSubmarines.com*)

Growth as researcher and academic

This thesis project has pushed me to grow as a researcher and academic. Today, I will approach research fundamentally differently than I would have 9 months ago. Those lessons are applicable not only to engineering, but to any discipline that requires a data-driven approach. I want to highlight my most profound learning experience: shifting focus from creating perfect inputs to analysing the outputs. At the beginning of this project, I was striving to obtain perfect inputs: perfect slab models, density distribution grounded in high-impact literature, realistic and high-resolution boundary models (topography, sediment, crust, etc.), and many other inputs. Ultimately, it is not the input that matters, but the output. I was confronted with this realisation at my mid-term review presentation. While I was presenting an algorithm to derive the oceanic lithospheric age at the trench and to propagate it in dip-direction, I realized that there were no results yet for this algorithm. Possibly, those additions to my slab model resulted in negligible changes of the gravity signal and were therefore not worth investigating. Here, I learned the hard way that it is important to obtain outputs as early as possible, to enable early judgement of whether the intended adjustments are worthwhile. Eventually, this lesson became the pinnacle of my thesis, testing gravity sensitivities for different slab parameters and model additions.

Leon Zhu Feng van Rossum
Delft, Monday August 20, 2018

The successful warrior is the average man,
with laser-like focus.

Master Bruce Li

Acknowledgements

First of all, I want to express my gratitude to my daily supervisor, Dr. Ir. Bart Root. When I handed in my literature study, I made sure that I was just in time to still be able to omit the Dr. and just write Ir. Bart Root. Not possible any-more this time. It was a privilege to attend your PhD defence and enjoy drinks together that night, also with Wouter. I remember thinking: ”*this is a very good start of the thesis, after two weeks I’m already having beers with my supervisors*”. I couldn't have wished for a better supervisor. Thanks for the 27 thesis and 10 literature meetings, where your good mood always made me leave much more motivated than I was before. Thanks for the possibility to have an EGU poster presentation.

Thanks Wouter, for providing input and feedback on those pivotal moments. I initially came to you looking for a topic, and I’m very happy that you stayed involved from the sideline. I want to thank the committee members, Bert, Taco and Hans, for the time and effort you will dedicate in assessing my thesis work.

I had such a good time in the graduation room. I guess, I’m now one of the veterans. Thanks Datta, for giving me advice before my job offer negotiations, and for helping me get over my jet-lag by enforcing a strict 8:45-in-the-room discipline. Thanks Corné, Hanneke, Maaike, Rutger, Zimo, Tom, Goncalo, Gulia, Federico, Max, Ram, and all the others, for the lunches together, and the positive vibes in the graduation room.

Thanks to all my Aerospace Engineering friends for this amazing student time, especially the guys from the first day at the EJW: Wouter, Tijs, Dirk-Jan, and Coen. Amazing to still be in touch, let’s keep it that way. Delft has been good to me, thanks to so many individuals, too many to name here. I’ll keep it to the Aerospace Engineering sphere. Thanks guys from the Design Synthesis Exercise for the amazing journey we made together those ten weeks, and beyond.

Lastly, thanks to my loving family, my dad, Diman van Rossum, my mum Yu Qing Li-Marr, and my brother Emar van Rossum. It is such a blessing and privilege to call you family!

Table of Contents

List of Figures

List of Tables

List of Acronyms

DD	Density distribution
FSM	Fast Spectral Method
GDH1	Global Depth and Heat model
GGT	Gravity Gradient Tensor
GOCE	Gravity Field and Steady-State Ocean Circulation Explorer
GST	Gravity Sensitivity Tests
HS	Half-Space Cooling model
ICGEM	International Centre for Global Earth Models
LAB	Lithosphere-Asthenosphere Boundary
PSM	Parsons, Sclater and McKenzie model
SHC	Spherical Harmonics Coefficients

List of Symbols

General

λ	Longitude	deg (°)
μ	Standard gravitational parameter	$3.9860004415 \times 10^{14}\ m^3/s^2$
ϕ	Ellipsoidal latitude	deg (°)
G	Gravitational constant	$6.67384 \times 10^{-11}\ N \cdot m^2/kg^2$
R	Earth equatorial radius	$6378136.30\ km$

Gravity modelling

α_{bin}	Truncation limit for the Fast Spectral Method (FSM) binomial series expansion	
ψ_{min}	Minimum spatial resolution	km
I_1	Second gravity gradient tensor invariant	$mGal^2/km^2$
l_{max}	Maximum model SHC d/o	
l_{min}	Minimum model SHC d/o	

Slab modelling

δ_D	Dip angle	deg (°)
κ	Thermal diffusivity	m^2/s
ϕ_{sub}	Co-latitude of subduction direction	deg (°)
ρ_{iso}	Isostatic density	kg/m^3
θ_S	Strike angle	deg (°)
L	Oceanic lithospheric thickness	km
N_{discr}	Number of samples for discretization of the trench	
N_{discr}	Number of subset entries for ageing	
t_{comp}	Thickness of compensating layer	km
V_p	P-wave velocity	km/s

1 Introduction

A subduction zone is a convergent plate boundary between a continental and an oceanic plate. The oceanic plate is heavier, and therefore subducts under the continental plate (Vermeersen, 2015). The subducting part of the oceanic plate is also called subducting slab. The subducting slab consists mainly of oceanic lithosphere and oceanic crust (Toksöz and Nafi, 1975). Subduction zones are responsible for more than 80% of all large earthquakes (Hayes and Wald, 2009). The Sumatra subduction zone is identified as one of Earth's most complex subduction zones because of simultaneous occurrence of different tectonic features (seamounts, aseismic ridges, fracture zones) and its rapid and oblique movement. Moreover, Sumatra was struck by severe earthquakes during the last three decades, especially in 2004-2005 (M_w = 9.2, M_w = 8.7), 2007 (M_w = 8.5, M_w = 7.9), and 2010 (M_w = 7.8) (Hayes et al., 2013). Those were all subduction zone earthquakes, which turned this region into a prime research area for geoscientists. Interestingly enough, this increased attention in the tectonics of the Sumatra region was only after the 2004 earthquake and its resulting tsunami. Barely seven year earlier, Sumatra's subduction zone only got a brief mention in the textbook by Yeats et al. (1997), which contrasted with the elaborate chapters on San Andreas Fault, Cascadia subduction zone, and Japan Trench (McCaffrey, 2009).

Earthquake prediction is the holy grail in geoscience (Vere-Jones, 1995; Sieh, 2006). Better understanding of subduction zones will in the long run lead to better understanding of the causes for earthquakes. Therefore, development and understanding of realistic models for the Sumatra subduction zone is essential. The term *Sumatra subduction zone* does not only refer to the subduction zone in direct proximity of Sumatra, but to the subduction zone in its entire extend.

1.1. Seismic and tomographic models for subduction zone modelling

Characterization of subduction zones is traditionally based on seismic models e.g. EHB (Engdahl et al., 2007), and tomographic models, e.g. UU-P07 (Amaru, 2007). Both seismic and tomographic models are based on earthquake or active source measurements from seismic station networks. However, many areas are inaccessible for seismic measurements due to political, geographical, economic reasons, or simply because those regions are aseismic (Gutknecht et al., 2014). This results in regional gaps in earthquake measurements. It is important to note that areas with gaps in seismicity can have potential for large future earthquakes (Fowler, 2005). Especially subduction zone fore-arcs, which mainly lie under water, are challenging and expensive regions to research but large earthquakes can originate there (Bassett and Watts, 2015b). This is also true for the Sumatra subduction zone.

Ambiguities between different scientific models and theories have been identified for the Sumatra subduction zone (Hall and Spakman, 2015; Pesicek et al., 2010). Two unresolved features will be discussed. Firstly, considering the northern part of the Sumatra subduction zone (ϕ = 1−8° N), Pesicek et al. (2010) concludes that there is probably a slab fold, whereas Hall and Spakman (2015) and Richards et al. (2007) counter this proposal by introducing models which include a slab tear. A much earlier study by Fauzi et al. (1996), counters the existence of slab tear. Both the existence and causal

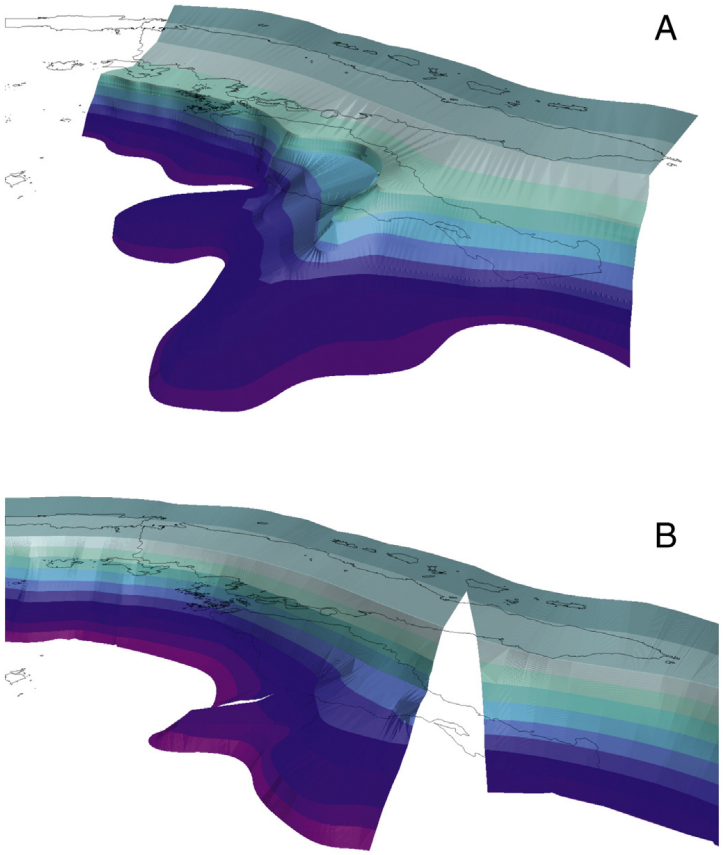

Figure 1.1: Simplified 3D figures showing the subducted slab beneath Sumatra to a depth of 600 km viewed from the north. Colour shades correspond to 50 km intervals. (**A**) Folded Sumatra slab based on Pesicek et al. (2008) (**B**) Sumatra slab with tear under the Toba volcanic centre based Hall and Spakman (2015)

mechanism of either a slab tear or a slab fold have not been confirmed. In Figure 1.1, both a slab fold and slab tear model are shown. Secondly, under Burma (ϕ = 20−23° N), Pesicek et al. (2010) expects a slab tear, Huang and Zhao (2006) a slab window, and Li et al. (2008) and Hall and Spakman (2015) modelled a continuous slab. Unfortunately, the regional datasets used by the different studies in this area do not overlap, the studies by Huang and Zhao (2006)and Li et al. (2008) extend Southward unto 25° N, whereas the study by Pesicek et al. (2010) extends Northward only until 23° N. Therefore, none of the hypothesis can either be rejected or accepted, as cross-checking with other studies is not possible. Limited literature is found on the region from Andaman Sea to Burma, because this region is known to be very complex and earthquake catalogue data is scarce, which results in slab models with high uncertainties. Even Hall and Spakman (2015) decided not to discuss this region due to its complexity. Therefore, investigation of the second unknown feature, the Burmese slab tear or window, is out of the scope of this project.

1.2. Gravity for subduction zone modelling

Positive velocity anomalies are observed for subduction zones in seismic and tomographic models, imaged at 700 km depth and beyond. These positive velocity anomalies are caused by subducted cool oceanic lithosphere (Vermeersen, 2015). Density anomalies in subduction zones are also observable as anomalies in gravity and gravity gradient observations. Gravity observations have long been known to contain valuable information about the Earth's interior, particularly about subduction zones. In 1931, Prof. Vening Meinesz spent six months on a submarine in the Indonesian Archipelago taking gravity measurements of the Sumatra subduction zone (Meinesz, 1931). Prof. Meinesz was already aware that gravity anomalies encompassed information on plate tectonics. The map of the measured gravity anomalies is given in Figure 1.2.

Recent satellite gravity mapping missions, like Gravity Field and Steady-State Ocean Circulation Ex-

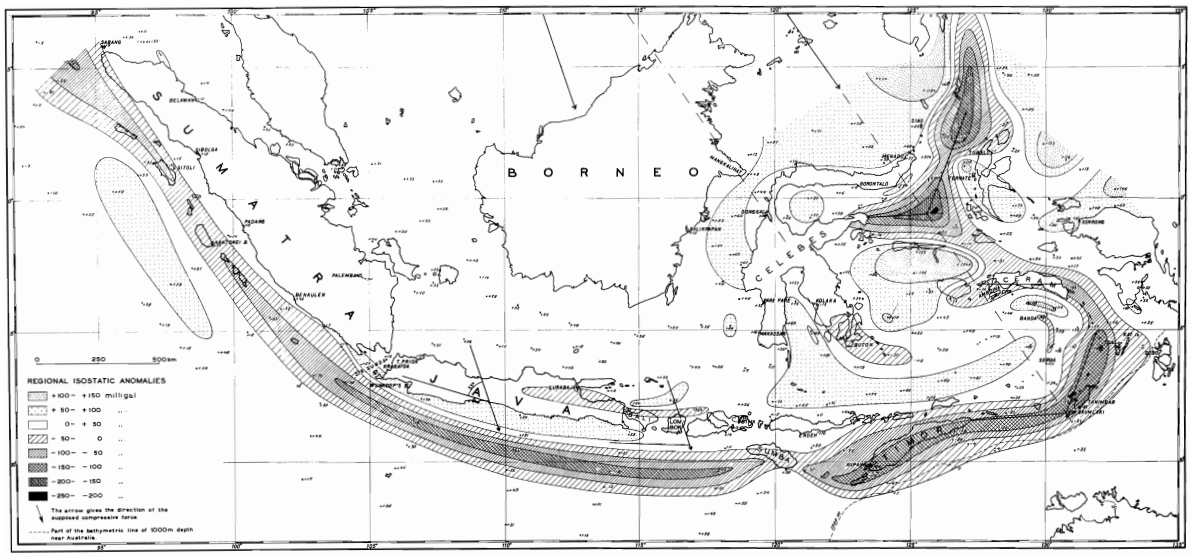

Figure 1.2: Gravity anomalies of the Sumatra subduction zone by Meinesz (1954)

plorer (GOCE), provide homogeneous and high-resolution gravity and gravity gradient information on areas normally inaccessible to earthquake measurements (Gutknecht et al., 2012). Are subduction zone features also observable in satellite gravity (gradient) data? The answer is clearly given by Mikhailov et al. (2004): "*Our results demonstrate that new satellite gravity data can be used to detect and discriminate geodynamic signals generated by subduction zone dynamics. In particular, to monitor locked asperities of subduction zones or to discriminate between different fault plane models*". Using either seismic, tomographic, gravity models, or combined models, scientists were able to create top-slab geometries of subduction zones, e.g. in Costa Rica or Sumatra (Gutknecht et al., 2012; Jacob et al., 2014; Broerse et al., 2015; Hall and Spakman, 2015; Wu et al., 2016).

Gravity data is non-unique. Seismic slab models use the valid assumption that earthquake locations occur on the interface between a subducting oceanic plate and over-riding continental plate. Making a line between those earthquake locations will result in an estimate of the top-slab surface, considering a certain error margin (~5 km) (Zhao et al., 1997). There is a unique correlation between the earthquake location and the top-slab surface. Unfortunately, this is not the case for gravity data. When modelling the Earth's interior, gravity data encompasses information of all the layers between the Earth's surface and its core. Gravity data does not provide a unique solution for the radial density distribution of the Earth. Different radial density structures might result in the same gravity signal. Therefore, incorporation of additional constraints is essential to overcome the problem of non-uniqueness in gravity modelling. If done correctly, new knowledge can be obtained about the Earth's interior based on gravity. The study by Rossi et al. (2017) is used as a case-study to confirm the importance of additional constraints and knowledge on the sensitivities of modelling parameters.

Rossi et al. (2017) used data from Gravity Field and Steady-State Ocean Circulation Explorer (GOCE), GOCO05s (Mayer-Gürr, 2015), to model the Tonga subduction zone using a top-slab model. Initially, this approach was also deemed suitable for the modelling of the Sumatra subduction zone. The thickness of the slab at the trench was fixed to 7 km, whereas an algorithm varied the crust depth, slab thickness at its base, crustal and slab densities such that resulting gravity signal matched GOCE gravity gradient observations. The study concluded that the slab thickness did not have a significant effect on the residuals with the observations, and selected a slab thickness of 7 km. This value is likely to be unrealistic, as it strongly contradicts conclusions from literature, where subducting slabs are modelled between 60-100 km thick, depending on the age of the incoming subducting oceanic lithosphere (Fowler, 2005; Lowrie, 2007; Köther et al., 2012; Gutknecht et al., 2012; Vermeersen, 2015; Goes et al., 2017; Zhang et al., 2017; Wilson, 2007). Rossi et al. (2017) concludes that the fit with gravity observations has been significantly improved with the inclusion of the slab model. Bassett and Watts (2015a) argues that it is very important to use other constraints (seismic models, tomographic models, etc.) in gravity modelling. Why could the approach of Rossi et al. (2017) not be applied in thesis?

When introducing enough degrees of freedom to a model and having limited or no constraints, there will always be a solution that confirms the hypothesis. The hypothesis in this case being that all the reduced satellite signal originates from the subducting slab. In this case, reduced signal refers to the observation signal without effects from topography and bathymetry. The outcome of this study is that it is possible to fit a slab model to gravity observations, however, there is no information on how accurate this slab model is or what this slab model adds to the knowledge of the Tonga subduction zone.

Rossi et al. (2017) assumes that the reduced gravity signal comes solely from the slab. However, apart from density anomalies, there are two other factors that influence the gravity signal in subduction zones: isostatic compensation (Watts, 2001), and forces in subduction zones (Forsyth and Uyeda, 1975). Firstly, isostatic compensation dictates that mass anomalies at a certain depth will be compensated by other masses anomalies in the same mass vertical column. It has been shown that both density contrasts and isostatic compensation affect the gravity anomalies of the subducting slab (Watts and Talwani, 1975; Davies, 1981). Moreover, Root et al. (2017) argues that isostasy is an essential part for modelling of the lithosphere and cannot be neglected. Secondly, subduction zones are subject to different driving (slab-pull, ridge-push) and resistive (mantle-drag, transform faults) forces in the subduction zone (Forsyth and Uyeda, 1975). Those forces induce dynamic processes, e.g. mantle wedge flows, which also have an influence on the gravity anomalies (Bassett and Watts, 2015a). A 3D slab geometry and density is required to model subduction zone dynamics (e.g. FEM) (Fowler, 2005).

1.3. Availability of tools and models

This thesis research is possible due to the availability of the necessary models and algorithms. First and foremost, the spectral gravity forward modelling algorithm provided by Root et al. (2016), provided a means to compute the gravity and gravity gradient signal of different Earth models using a spherical harmonics representation. Moreover, a combined slab model for the Sumatra subduction zone was provided by Broerse et al. (2015). The optimal SHC bandwidth needs to be known in order to isolate the desired signal in the observations. This knowledge will result in more efficient computations as only the SHC are used which are required to obtain the desired signal. This optimal SHC bandwidth will be investigated using a spectral analysis for both the combined model as Slab1.0.

It was encouraging to experience the corporative spirit in the geoscience community, in other words, the power of sharing. Numerous global models (Whittaker et al., 2013; Szwillus, 2018; Hayes et al., 2012b; Müller et al., 2008; Amante and Eakins, 2009) were freely available and easily accessible online. Most of them were well documented which allowed for smooth implementation.

1.4. Research aim and research questions

The research aim of this thesis is ultimately to improve the understanding of the Sumatra subduction zone. This was done by modelling the subducting slab and investigating the gravity sensitivities to different individual slab model parameters and features. Understanding the gravity sensitivity of different slab parameters and features serves three purposes. Firstly, knowing the sensitivities will allow for more informed adjustments of slab model when using gravity observations as an additional constraint in slab modelling. Secondly, the uncertainty of a gravity observation model can be translated to corresponding uncertainties in different slab parameters, and vice versa. For instance, when the gravity model has an uncertainty of A mGal, this translates into an uncertainty of B km for slab parameters C at a depth of D km. Knowing those uncertainties will allow for the estimation of the desired ranges and accuracies of the slab parameters, and create selection criteria for external input models. Thirdly, regional and local gravity observation anomalies can be linked to certain slab features, and vice versa, slab features can be used to fit regional and local gravity observation anomalies.

Moreover, isostatic compensation of the slab will be investigated. Pratt's hypothesis will be used to apply isostasy, which states that compensation is achieved by lateral density variations in a compensation layer (Fowler, 2005). Laterally varying the lithospheric densities to obtain isostatic equilibrium provides good first-order lithospheric densities (Root et al., 2017). Moreover, varying mantle densities has also been used to model isostasy (Root et al., 2014). Traditionally, the crust has been used a compensating layer (Lowrie, 2007). Literature uses different definitions for the compensating layer (crust, lithosphere or mantle), which will all be investigated.

This leads us to the main research questions of this thesis:

What slab parameters and slab features need to be included to generate a simple slab model?

What is the optimal spherical harmonic bandwidth that isolates the slab model signal?

What are the qualitative and quantitative sensitivities of the radial gravity and second gravity gradient invariant to different slab parameters and slab features?

What isostatic compensation method yields the most realistic compensation density values and provides a realistic gravity signal?

After those questions have been answered, the sensitivities can be used in further slab modelling and help to answer the larger research question:

Can a simple slab model incorporating the different slab parameters and features explain the corresponding gravity anomalies in XGM2016?

ESA 3D-Earth

This project falls within the context of the ESA 3D-Earth project. 3D-Earth wants to promote the usage of GOCE satellite gravity gradients for modelling of the Earth's interior. Within 3D-Earth the TU Delft proposed to carry out a case study on the subduction zone of Sumatra, from which this thesis proposal originated. It is important to mention that even though 3D-Earth is centred around the usage of ESA satellite data, this thesis project is not restricted by this requirement.

1.5. Structure of this thesis

The most important chapter of this thesis is Chapter 6, four out of five research questions get answered there. Chapter 2 gives the mathematical background for gravity modelling, provides a detailed analysis of the gravity models that are going to be used throughout this thesis, and discusses the used forward modelling algorithm. Chapter 3 and Chapter 4 will provide the reader with understanding of the slab modelling process. Different modelling methods have been developed and are discussed in those chapters. Chapter 5 creates the link between Chapter 6 and the first four chapters. Here, the focus starts to shift from discussing different methodologies to the analysis of the gravity results. Now that the methods and models have been fully introduced, Chapter 6 will provide extensive discussions and conclusions on the gravity sensitivity of different slab parameters and slab features. The thesis is wrapped up with conclusions and recommendations. The reader is expected to have basic knowledge on geoscience and gravity modelling, and the related terminology.

2

Gravity and Gravity Gradients Modelling

This section will contain all the information necessary to carry out the proposed gravity and gravity gradient 3D modelling of the Sumatra slab. Firstly, an introduction is given on the gravity, and gravity gradient, and gravity gradient invariants. Second, the relation between the maximum Spherical Harmonics Coefficients (SHC) degree of used models and their maximum spatial resolution will be discussed. Thirdly, XGM2016 and GOCO05s will be presented and some model validations will be given. Lastly, the spectral gravity forward modelling algorithm will be discussed, which is used to compute the SHC, and subsequently, the gravity and gravity gradient fields.

Throughout this thesis the spherical harmonic representation of the gravity field will be used, which is represented by the equation below (Barthelmes, 2013, Eq. 108). The spherical latitude will be used (ϕ) instead of the ellipsoidal (φ), where the gravitational potential (W_a) is given by:

$$W_a(r,\lambda,\phi) = \frac{GM}{R}\sum_{l=0}^{l_{max}}\sum_{m=0}^{l}\left(\frac{R}{r}\right)^{l+1} P_{lm}(\sin\phi)\left[C_{lm}^{W}\cos m\lambda + S_{lm}^{W}\sin m\lambda\right] \tag{2.1}$$

Where r, λ, and ϕ are the spherical coordinates (radius, longitude, latitude), R the Earth's radius, GM the standard gravitational constant, l and m the degree and order, and C_{lm}^{W} and S_{lm}^{W} are the Spherical Harmonics Coefficients (SHC). The attenuating effect on the gravitational potential by increasing altitude of the computation point ($r > R$) is evident through the term $(R/r)^{l}$. Thus, when computing the gravitational potential at satellite altitude, the higher order SHC will be heavily attenuated (Barthelmes, 2013).

Although considered textbook knowledge, Newton's law of universal gravitation is given here to support later discussions (Brackenridge et al., 2000):

$$F_g = G\frac{m_A\, m_B}{r^2} \tag{2.2}$$

Where F_g is the gravitational force between two masses m_A and m_B separated by a distance r, and G is the gravitational constant.

2.1. Gravity Gradients and Invariants

In this section the expressions for the gravity gradient tensor and gravity gradient tensor invariants are given. For datasets which have the same resolution for the gravity field and gravity gradient field, gravity gradients provide higher frequency anomalies than the gravity field does (Mikhailov et al., 2007). In other words, gravity gradients provide a higher sensitivity with respect to regional density anomalies, which in turn leads to potentially more accurate characterization of subduction zones (Švarc et al., 2016).

The Japanese and Andean/Chilean subduction zones have a North-South orientation. Therefore, usage of the North-North and East-East gravity gradients (T_{xx} , T_{yy}) is evident. The absence of studies

using gravity gradients for Sumatra is expected to be related to the fact that the Sumatra subduction zone is curved. For this reason, the usability of the invariants will be investigated. Invariants incorporate all components of the Gravity Gradient Tensor (GGT) while being direction-independent.

Density variations can be found both in the gravity field and the Marussi tensor. However, those reflect different geological features according to Braitenberg et al. (2011). A less dramatic difference between the Marussi tensor and the gravity field is presented by (Alvarez et al., 2012). He states that both contain information on the same geological features, however, in a different way. Firstly, the vertical gravity gradient (T_{zz}) contains information on mass heterogeneities, however, the Marussi tensor losses sensitivity with depth. Secondly, gravity fields are useful for relatively small density contrasts and deeper structures.

2.1.1. Gravity Gradient Tensor

The gravitational potential is given as follows (Pedersen and Rasmussen, 1990):

$$U(\mathbf{r_0}) = -G \int_V \frac{\rho(\mathbf{r})}{R} dV \tag{2.3}$$

Where $\mathbf{r_0}$ is the observation point, $\mathbf{r}$ the integration point, $R = |\mathbf{r_0} - \mathbf{r}|$, ρ the excess density, V the volume of the body, and G the gravitational constant. Taking the double gradient of the gravitational potential gives the Marussi tensor, from now on called GGT:

$$\text{GGT} = \nabla^2 U = \nabla g = \begin{bmatrix} \frac{\partial^2 U}{\partial x^2} & \frac{\partial^2 U}{\partial x \partial y} & \frac{\partial^2 U}{\partial x \partial z} \\ \frac{\partial^2 U}{\partial y \partial x} & \frac{\partial^2 U}{\partial y^2} & \frac{\partial^2 U}{\partial y \partial z} \\ \frac{\partial^2 U}{\partial z \partial x} & \frac{\partial^2 U}{\partial z \partial y} & \frac{\partial^2 U}{\partial z^2} \end{bmatrix} = \begin{bmatrix} \frac{\partial g_x}{\partial x} & \frac{\partial g_x}{\partial y} & \frac{\partial g_x}{\partial z} \\ \frac{\partial g_y}{\partial x} & \frac{\partial g_y}{\partial y} & \frac{\partial g_y}{\partial z} \\ \frac{\partial g_z}{\partial x} & \frac{\partial g_z}{\partial y} & \frac{\partial g_z}{\partial z} \end{bmatrix} = \begin{bmatrix} T_{xx} & T_{xy} & T_{xz} \\ T_{yx} & T_{yy} & T_{yz} \\ T_{zx} & T_{zy} & T_{zz} \end{bmatrix} \tag{2.4}$$

Where g_x, g_y, g_z are the components of the gravitational acceleration vector. Those are obtained by taking the gradient of the gravitational potential (∇U).

The gradients contain information about the rate of change for the individual gravitational acceleration components in different directions (x,y,z). For example, T_{zz} gives the rate of change for g_z when moving a unit length in z-direction. g_z is the gravitational acceleration of mass A due to mass B in z-direction. Consider the case where the z-axis points radially outwards from point mass A to point mass B. Equation 2.2 shows that gravity varies with distance proportionally to $1/r^2$, or in this case, $1/z^2$. Equation 2.4 shows that T_{zz} is the partial derivative of g_z with respect to z. Therefore, for T_{zz} the distance varies proportional to $1/z^3$, as is shown in the equations below:

$$g_z = G\frac{m_B}{z^2} \tag{2.5}$$

$$T_{zz} = \frac{\partial g_z}{\partial z} = -2\frac{(Gm_B)^2}{z^3} \tag{2.6}$$

Simplifying the problem using $m_B = 1$ and $G = 1$ enables us to inspect how g_z and T_{zz} relate to distance, see Figure 2.1. T_{zz} is more sensitive to masses nearby, seeing a fast decay of the signal with increasing distance. T_{zz} has reduced to 10% at $z = 0.21m$ which is approximately 50% faster than g_z, which reaches 10% of its signal at $z = 0.32m$. Important to note that for this simplified example the numbers themselves carry no significant information, however, one can conclude that g_z is more useful for masses that are further away, and the T_{zz} has a higher sensitivity for masses nearby. Discussions on the other GGT components will be given later in Subsection 2.3.2, where practical examples can be used to aid the readers understanding.

2.1.2. Gravity Gradient Tensor Invariants (I_0, I_1, I_2)

The invariants of the gravity gradient tensor contain information about the dimensionality of the gravity anomalies. Invariants are used to model subsurface structures (Beiki and Pedersen, 2010; Yu and Zhao, 2010; Oruç, 2010). Contrary to the gravity anomalies and gravity gradients, the invariants are not direction-dependent (Pedersen and Rasmussen, 1990), which makes them potentially useful to

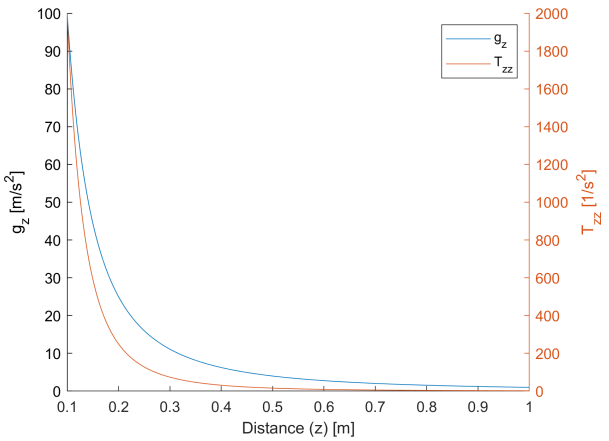

Figure 2.1: General relation for g_z and T_{zz} with distance

analyse features that have changing orientations, e.g. subduction zones. The second incentive for using invariants is that the errors in the orientation of measurement sensors and random noise in the measurement channels will not effect the tensor invariants (Mikhailov et al., 2007). On the downside, the dimensionality information of the gravity gradients is lost when computing the invariants.

Literature shows that invariants are only used for modelling of shallow subsurface features. Oruç (2010) used invariants (I_1, I_2) together with a high-resolution (~ 0.1 km) terrestrial gravity gradient dataset to find a subsurface feature at a depth of 5 km, in his case, a salt dome offshore Louisiana, USA. The depth estimation accuracy was in the order of 10 m. The Vredefort impact structure in South Africa was investigated Beiki and Pedersen (2010) using airborne data with a resolution of 0.25 m. This structure had a diameter of 250-300km, and the depths were only estimated down to 1500m. For subduction zone modelling one investigates features down to 670 km, with gravity dataset resolutions in the order of ~100 km. Thus far, invariants have primarily been used for shallow subsurface structures, and their application to deep structures like subduction zones has to be investigated, which will be done in this thesis (Beiki and Pedersen, 2010; Bouman et al., 2013; Klokočník et al., 2014).

Using an arbitrary reference system, the invariants are given below, where GGT denotes the 3x3 Marussi tensor given in Equation 2.4 (Pedersen and Rasmussen, 1990):

$$I_0 = \text{trace}(GGT) = T_{xx} + T_{yy} + T_{zz} \tag{2.7}$$

$$I_1 = T_{xx}T_{yy} + T_{xx}T_{zz} + T_{yy}T_{zz} - T_{xy}^2 - T_{xz}^2 - T_{yz}^2 \tag{2.8}$$

$$I_2 = \det(GGT) = T_{xx}T_{yy}T_{zz} + 2T_{xy}T_{yz}T_{xz} - T_{yz}^2T_{xx} - T_{xz}^2T_{yy} - T_{xy}^2T_{zz} \tag{2.9}$$

Note that I_0 should be zero, because the GGT is symmetric and therefore traceless according to Laplace's equation (Oruç, 2010). Moreover, assuming that the GGT is symmetric and has real eigenvalues, $I_1 \leq 0$ (Pedersen and Rasmussen, 1990). Invariant are mainly used for contouring of geological structure. However, their physical interpretation remains a topic for further research.

Literature on the usage of gravity, GGT, and invariants for subduction zones provides two main instructions (Braitenberg et al., 2011; Alvarez et al., 2012):

- Use gravity field for relatively smaller density contrasts at deeper depths
- Use GGT and invariants to map density contrasts in shallow parts of the subduction zone

2.2. Maximum resolution of model

Using the equations given in Barthelmes (2013), one can determine the maximum spatial resolution obtainable at the Earth surface for a given maximum model degree (l_{max}). The maximum number of zeros at the equator can be used to compute the maximum spatial resolution, or in other words, the shortest half-wavelength (Barthelmes, 2013, Eq. 112):

$$\psi_{min,general}\,(l_{max}) \approx \frac{\pi R}{l_{max}} \tag{2.10}$$

Maximum Degree	Number of Coefficients	Resolution ψ_{min}			
		General		Advanced	
ℓ_{max}	N	[degree]	[km]	[degree]	[km]
2	9	90.000	10000.000	77.885	8653.876
5	36	36.000	4000.000	38.376	4264.030
10	121	18.000	2000.000	20.864	2318.182
15	256	12.000	1333.333	14.333	1592.587
30	961	6.000	666.667	7.394	821.587
36	1369	5.000	555.556	6.195	688.321
40	1681	4.500	500.000	5.590	621.154
45	2116	4.000	444.444	4.983	553.626
50	2601	3.600	400.000	4.494	499.342
75	5776	2.400	266.667	3.016	335.073
180	32761	1.000	111.111	1.266	140.690
360	130321	0.500	55.556	0.635	70.540
500	251001	0.360	40.000	0.457	50.828
1000	1002001	0.180	20.000	0.229	25.439
2000	4004001	0.090	10.000	0.115	12.726
5000	25010001	0.036	4.000	0.046	5.092
10000	100020001	0.018	2.000	0.023	2.546

Table 2.1: Maximum spatial resolution: smallest feature that is distinguishable (ψ_{min}) within a model having a certain maximum degree (l_{max}), *adjusted from:* Barthelmes (2013, Tab. 1)

Where ψ_{min} is the resolution in km at the equator, and R the Earth's radius in km. A more accurate equation for the spatial resolution, based on a spherical harmonic representation of a equiareal pieces, is given below (Barthelmes, 2013, Eq. 114):

$$\psi_{min,\,advanced}\,(l_{max}) = 4\arcsin\left(\frac{1}{l_{max}+1}\right) \tag{2.11}$$

The spatial resolutions computed with the general and advanced equations are given in Table 2.1. From this table it is evident that advanced equation provides a more conservative spatial resolution than general equation, neglecting $l_{max} = 2$. Barthelmes (2013, Fig. 5) uses a synthetic signal to show that the advanced equation more accurately relates l_{max} to spatial resolution. Throughout this report, the general and advanced equations will dictate the upper and lower limits of obtainable spatial resolution for values of l_{max}.

2.3. Gravity observation models

XGM2016 is considered the most gravity suitable model for analysing the Sumatra subduction zone, Firstly because of the high spatial resolution of the incorporated datasets, and secondly, due to the combination of many independent datasets. Other models, e.g. EGM2008, GEBO, GOCO05s and others, were investigated, however, those were found inferior to XGM2016.

XGM2016 is a combined terrestrial-satellite-derived gravity model, incorporating 11 years of GRACE (2000-2013), 4 years of GOCE (2009-2013), new terrestrial and altimetry data (Pail et al., 2016). GOCO05s is a satellite-only gravity model mainly based on data from the ESA GOCE mission. GOCO05s will not be used as an independent model. It is only discussed because it is incorporated into XGM2016. The SHC datasets of both models were downloaded online from International Centre for Global Earth Models (ICGEM) portal (Barthelmes and Köhler, 2016).

2.3.1. GOCO05s

GOCO05s is resolved up to degree 720. The spatial resolution is at least 15'x15'. NIMA96 is used as fill-in gravity anomaly dataset in the Sumatra region, which has a lower spatial resolution of 30'x30' (Fecher et al., 2016). GOCO05s incorporates data from GRACE (SHC<120) and GOCE (SHC: 120-260) (Mayer-Gürr, 2015). The full-lifetime GOCE gravity anomaly data has an accuracy of ~1 mGal and 0.4 mE for vertical gravity gradients at resolutions of d/o 200 (Pail et al., 2011; Pail, 2012). GRACE

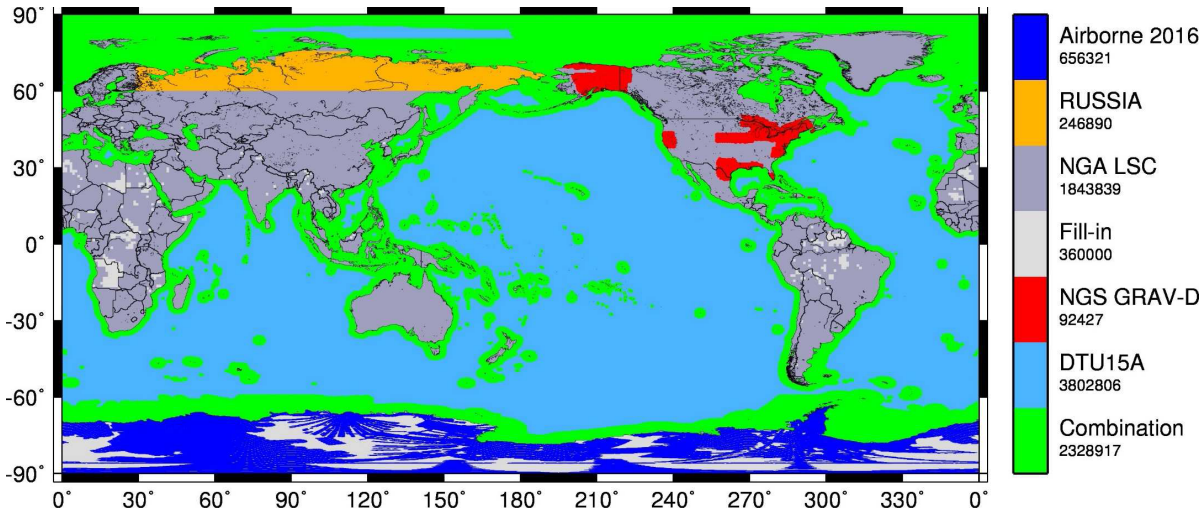

Figure 2.2: Global gravity anomaly datasets used for XGM2016, where numbers correspond to incorporated data-points (Pail et al., 2016)

gravity data has a similar gravity anomaly accuracy of ~1 mGal (Floberghagen et al., 2011). The model accuracy depends on the SHC truncation settings used, larger bandwidths will have larger gravity errors. The accumulative gravity error between d/o 0-150 is ~0.3 mGal. For higher d/o than 150 this errors increases rapidly, 300% between 150-200, and by 400% between 200-250 (Pail, 2012). While selecting a SHC truncation settings, one should keep in mind that the errors for GOCO05s, increase significantly for SHC above d/o 200.

2.3.2. XGM2016

The United States National Geospatial-Intelligence Agency (NGA) is working towards an updated version of EGM2008, which will be released in 2019 under the name EGM2020. XGM2016 is an intermediate update towards EGM2020 by the Technical University of Munich. It is modelled up unto the spherical harmonic degree of 719, combining GOCO05s with a 0.25°x0.25° gravity anomaly grid from the National Geospatial-Intelligence Agency's Least-Squares Collocation (NGA-LSC). XGM2016 is fully based on GOCO05s up unto SHC d/o 110, between d/o 110 and 200 the coefficients are computed using both satellite and terrestrial datasets, and for d/o higher than 200 the coefficients are fully based on terrestrial data. Therefore, if XGM2016 is only used for lower SHC d/o than 100, one is simply using GOCO05s, which explains why proper understanding of that model is also required. The accumulative gravity error for GOCO05s explained in Subsection 2.3.1 is mitigated in XGM2016, because terrestrial data is incorporated for SHC d/o above 150. XGM2016 was released exactly at the start of my thesis project.

The resolution computed using Equation 2.11 is merely an upper limit for the maximum obtainable spatial resolution. Terrestrial datasets have varying regional data coverage and accuracy. On the contrary, satellite datasets generally have homogeneous global coverage and accuracy. Therefore, combining regional terrestrial datasets with global satellite datasets induces resolution variations from one region to the other (ICGEM, 2017). Concluding, only if the resolution of all the incorporated datasets has a resolution of 0.3°, the regional resolution of XGM2016 will approach the upper limit of 0.3°. The different datasets used for XGM2016 are given in Figure 2.2. NGA LSC was used for Sumatra and the other Indonesian islands, for the coastal oceanic regions different datasets were combined, for the oceans DTU15A was used.

Results and validation of XGM2016 and forward modelling tool

The gravitational potential (U) is considered ineffective for subduction zone analysis, due to its very long wave-length signal. Literature does not show a consistent trend for the usage of the GGT for subduction zone research. Alvarez et al. (2015) and Rossi et al. (2017) use T_{zz} for gravity inversion for the Andean and Tonga subduction zone. Mansi et al. (2013, 2014) uses the diagonal entries of GGT (T_{xx}, T_{yy}, T_{zz}), and Švarc et al. (2016) uses all GGT components. For this study, the other GGT

components are not shown nor investigated, as the invariants combine all the information from the GGT.

The *synthesis* of XGM2016 was done for $l_{max} = 90$, 179 and 719, whereas results for $l_{max} = 90$ will be shown and discussed later in this report. The results for the radial gravity (g_R), radial-radial gravity gradient (T_{RR}) are shown in Figure 2.3. For both SH truncations there is a strong positive g_R anomaly (∼100-150 mGal) following the volcanic arc from Java unto the middle of Sumatra. A negative g_R anomaly (∼-100 mGal) is observed in front of the trench in the Java and Andaman Sea region. The same features are seen for T_{RR} truncated at d/o 179. For the truncation setting at 719, an additional negative anomaly is observed following the trench. For both truncations settings and both g_R and T_{RR}, the negative and positive anomalies are absent in the northern region of Sumatra, approximately at a latitude of 2 degrees. An explanation for this interesting phenomena will be presented later.

Chesner (1998, 2012) showed that there is a lot of tectonic activity below the Toba volcanic centre in northern Sumatra, located at red circle in Figure 2.3a. Negative P-wave seismic velocity anomalies are observed below the volcanic centre due to serpentinization of the subducting crust, and the subsequently ascensions of relatively low density fluids. This does not explain the positive anomalies of g_R and T_{RR}, so different explanations need to be investigated. The Toba volcanic centre has a maximum dimension of ∼100 km, which would only be distinguishable in gravity data for $l_{max} \approx 180$, see Table 2.1. For $l_{max} = 90$, the volcanic centre is indeed not visible in the gravity data.

The second and third invariants (I_1, I_2) are shown in Figure 2.4. The I_1 signal follows the shape of the subduction zone, whereas the I_2 signal only has shows a distinct signal for the full model ($l_{max} = 719$). Due to the lack of signal in I_2 for lower l_{max}, it is not used in further analyses.

To have the full confidence that the gravity forward modelling tool was working correctly (Root et al., 2016), it was deemed useful to validate its output with another algorithm. The output of the MATLAB® *synthesis* algorithm was validated with plots obtained from the ICGEM Calculation Service. The *synthesis* output is given in Figure 2.3a and 2.3c, whereas the ICGEM validation data for $l_{max} = 179$ is given in Figure 2.5. The *synthesis* plots closely match the validation plots. The *synthesis* results for g_R show a maximum residual in the order of 10% with the validation data. This residual is primarily caused by a constant positive difference of ∼15 mGal. This difference is observed when investigating the offset in the extreme values for *synthesis* and validation data: -113 and 187 mGal (*synthesis*) compared to -129 and 170 mGal (*validation*). The residuals for T_{RR} were in the order of 2%, corresponding to differences of less than ∼0.5 Eötvös. The extreme values for both were: -23.4 and 28.5 Eötvös (*synthesis*) compared to -23.7 and 28.8 Eötvös (*validation*). Moreover, the same signal patterns are visible, and no major differences were identified between the *synthesis* and validation results. Therefore, both the XGM2016 model as the forward modelling tool were validated to be loaded and working correctly.

Truncation settings for XGM2016

Several truncations were investigated and applied to the *synthesis* of XGM2016. Firstly, and most importantly, the $C_{2,0}$ term was neglected, removing most of the signal coming for the ellipsoidal Earth (J_2). Secondly, the long wavelength signal from non-subduction zone features (e.g. mantle) is removed by truncating the lower SHC limit. Mansi et al. (2014) used $l_{min} = 9$, whereas Švarc et al. (2016) used $l_{min} = 60$. The SHC lower limit is determined using a spectral analysis, which is done in Section 6.1. Thirdly, short wavelength signal from non-subduction zone features (e.g. topography, bathymetry, sediments, etc.) are removed by truncating the upper SHC limit or applying a topographic correction. Mansi et al. (2014) applied topographic correction using ETOPO1 at 7 km, whereas Gutknecht et al. (2012) applied a topographic gradient correction using GOCO03s (T_{rr}) at 8 km.

To gain understanding of what structures are visible in the GGT invariants, the invariants are computed for different SHC truncation settings. The conclusions are presented in this section. First, truncating the lower limit with $l_{min} = 2$ and 8 was investigated. For either truncation limit, the measured values for I_1 were almost identical, with minor differences ranging between 0.5% and 1.6% depending on locations in the subduction zone. Therefore, one can conclude that the SHC between d/o 2 and 8 do not contain a strong I_1 signal.

Figure 2.6 shows that there is very little signal for $2 \leq$ d/o ≤ 40 in the second tensor invariant (I_1). The second invariant increases approximately by a factor 30 comparing SHC=2-40 to SHC=40-90.

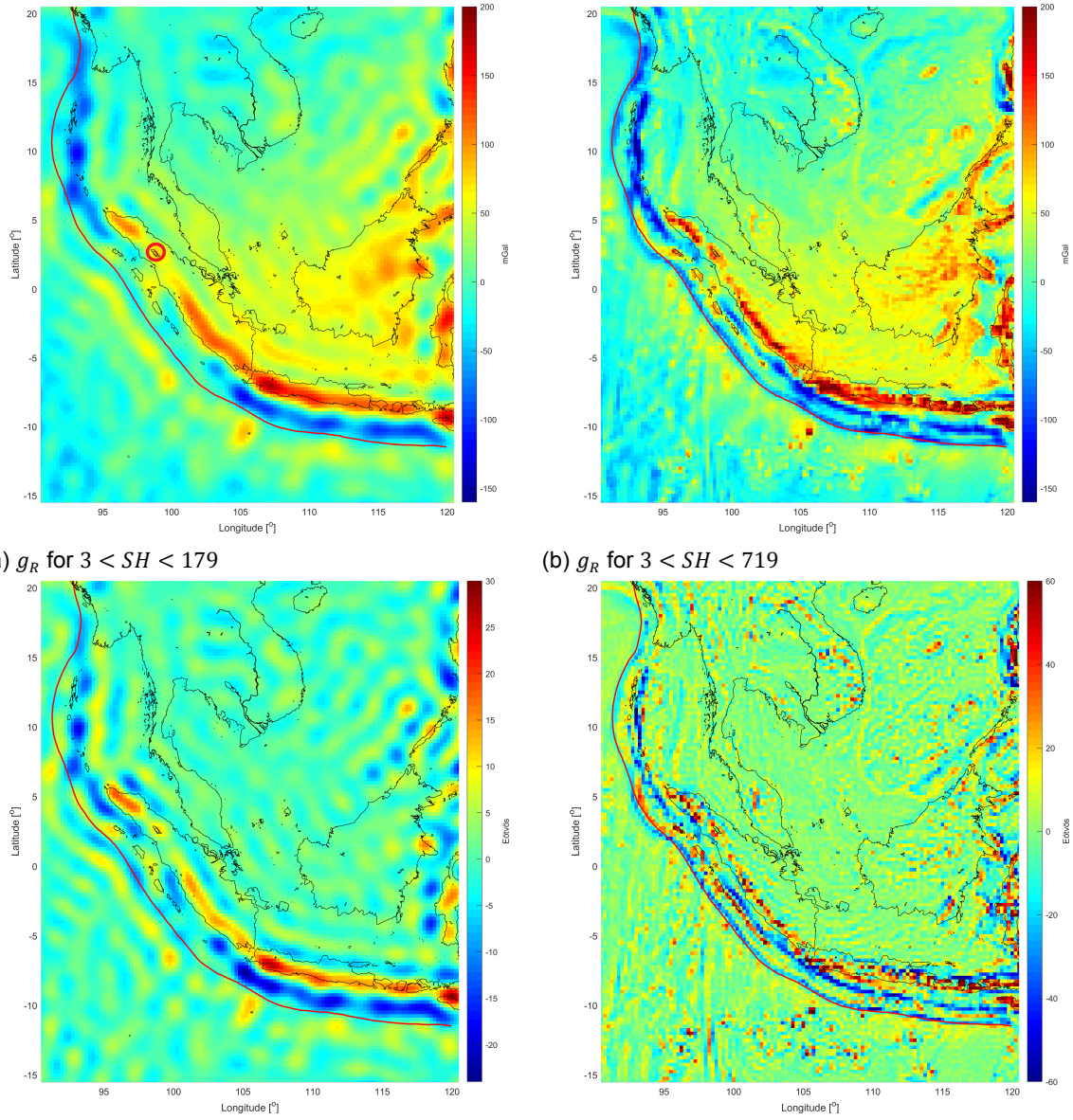

(a) g_R for $3 < SH < 179$

(b) g_R for $3 < SH < 719$

(c) T_{RR} for $3 < SH < 179$

(d) T_{RR} for $3 < SH < 719$

Figure 2.3: XGM2016 radial gravity (g_R) and radial-radial GGT component (T_{RR}) for different SHC settings

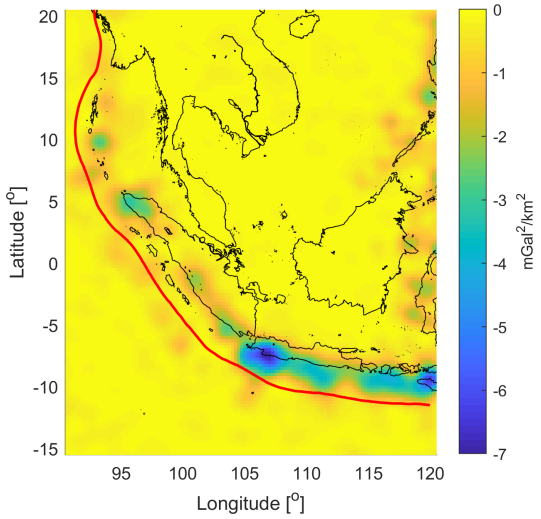

(a) I_1 for $3 < SH < 179$

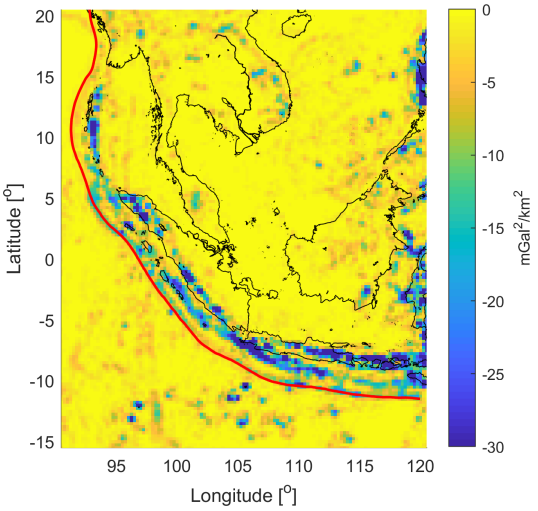

(b) I_1 for $3 < SH < 719$

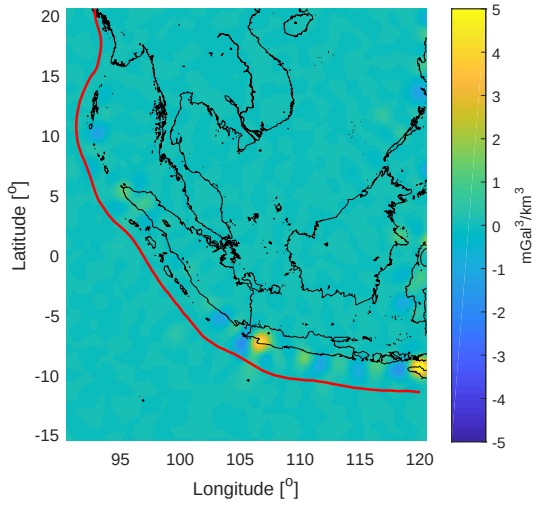

(c) I_2: for $3 < SH < 179$

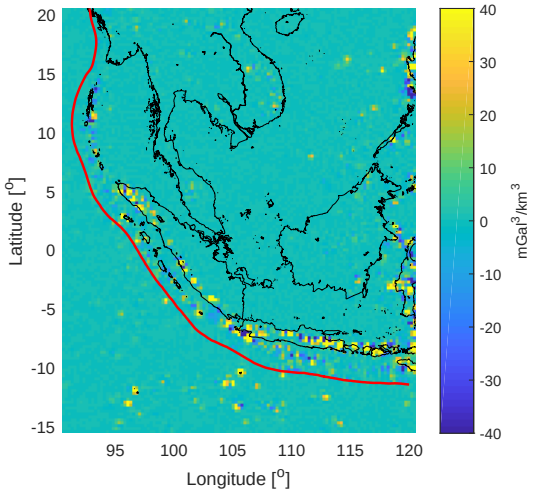

(d) I_2: for $3 < SH < 719$

Figure 2.4: XGM2016 second and third Invariants (I_1, I_2) for different SHC settings

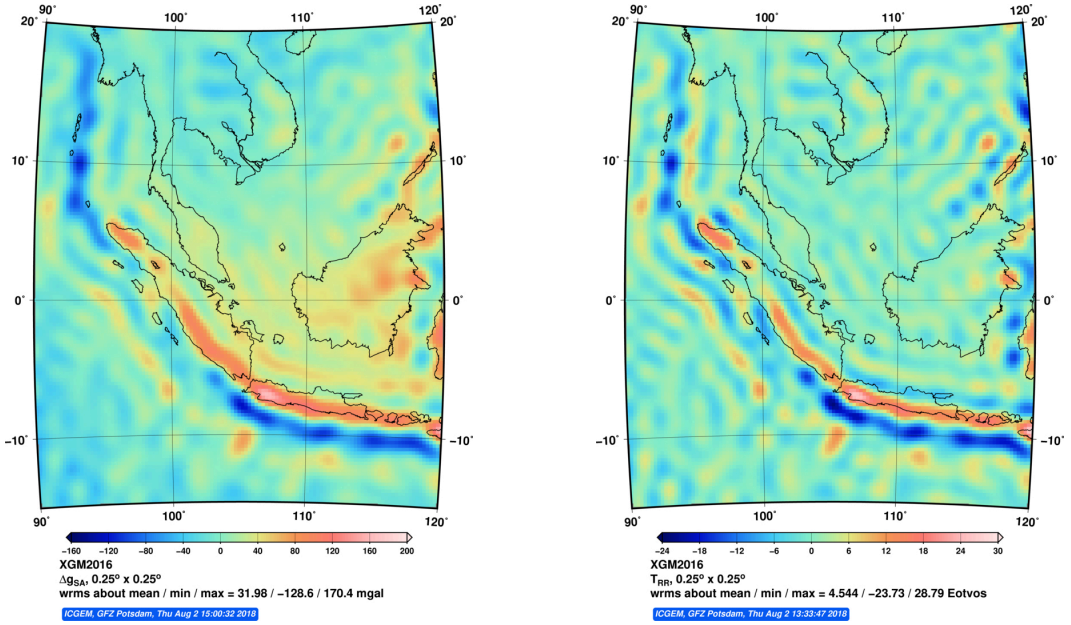

Figure 2.5: Results from ICGEM Calculation Service used for validation ($l_{max} = 179$)

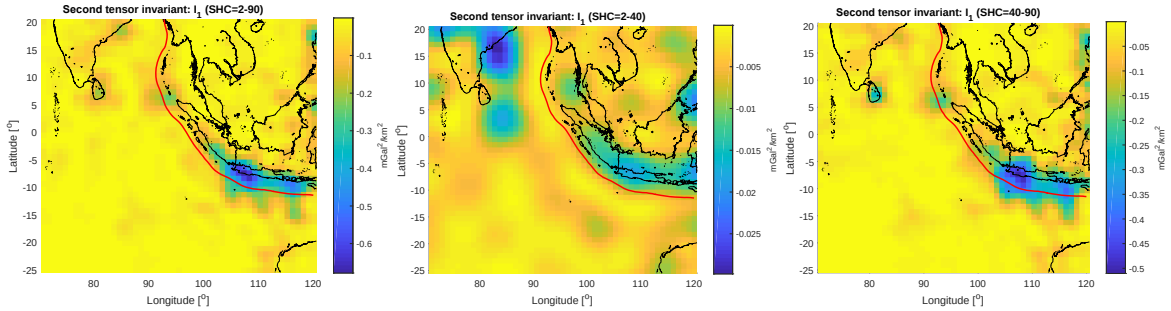

Figure 2.6: Resulting I_1 for different SHC truncation settings, with the lower SHC boundary truncated between d/o 2 and 40

Moreover, for SHC=2-40 there is a weak long wavelength signal that corresponds to the shape of the subduction zone. This long wavelength signal is overpowered by a localised signal coming from western Java, see the blue anomaly in SHC=2-90 and SHC=40-90. For all three truncation settings, it stands out that there is no trench-perpendicular anomaly around the Toba volcanic centre, for its location recall the red circle in Figure 2.3a. The results showed that the strong signal coming from the Java region weakens for increasing l_{min}, and disappears for $l_{min} = 80$.

One continued to incrementally increase l_{min} from d/o 50 to 80, which results are summarized in Figure 2.7, which has its negative y-axis pointing upwards. The values were measured at the strong anomaly in western Java, see Figure 2.6. The minor decrease in I_1 from l_{min} d/o 2 to 40 in Figure 2.7, is in agreement with the conclusion made earlier, that there is little signal in this bandwidth. The sharp decrease in I_1 for l_{min} d/o 40 to 80 shows that this bandwidth contains most of the second invariant signal. As stated in Figure 2.3.2, different truncation settings could be used to utilize both gravity and gravity gradients in their optimal wavelength. This recommendation should also be extended to the usage of the invariants.

While doing observation for different truncation settings, one noticed the direct correlation between the landmass of Sri Lanka and the relatively high negative values for I_1 and I_2, see Figure 2.8. The cause for this correlation should be further investigated, however, it is outside the scope of this thesis project. A possible hypothesis could be that a steep bathymetry profile in all directions around Sri Lanka causes large values for the GGT components, and subsequently for I_1 and I_2.

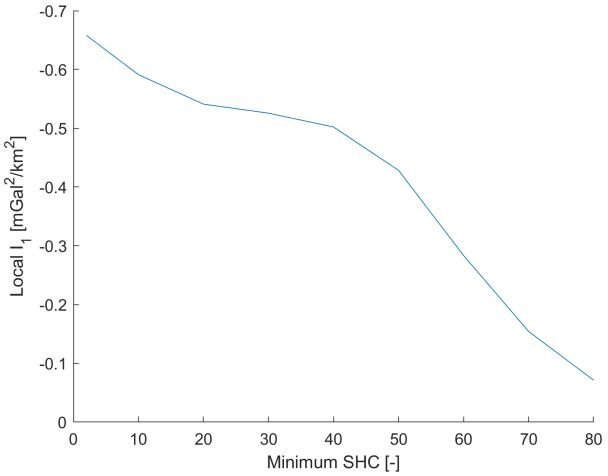

Figure 2.7: Results for *analysis* of XGM2016 for different minimum SHC, using $l_{max} = 90$

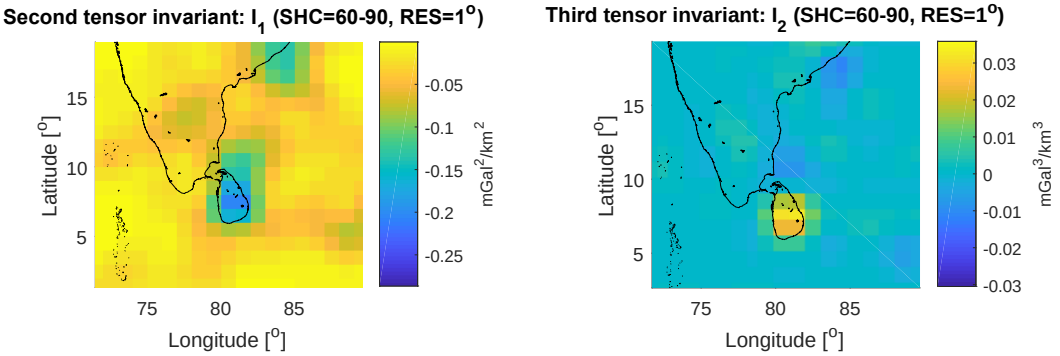

Figure 2.8: Observed correlation in XGM2016 for I_1, I_2 and the landmass of Sri Lanka

Comparison: XGM2016 and GOCO05s

A gravity anomaly residual analysis was done comparing XGM2016 with GOCO05s for different SHC truncation settings, with l_{max} varying from d/o 50 to 250. Recall that GOCO05s was used for the first d/o 100 SHC of XGM2016. It was shown that for low truncation of $l_{max} = 50$, the residual is in the order of 10^{-4} mGal, whereas it increased three orders of magnitude for $l_{max} = 120$. The residuals for $l_{max} = 90$ and $l_{max} = 100$, were in the order of 10^{-3} and 10^{-2} mGal, respectively. For higher d/o the residual kept increasing, because one is comparing GOCO05s with other terrestrial datasets which are incorporated in XGM2016 for SHC above d/o 100. For $l_{max} = 180$ and 250, the residual between XGM2016 and GOCO05s was in order of 1 and 10 mGal. Therefore, for the first 180 SHC d/o significant amount of satellite derived gravity data was used in XGM2016.

2.4. Spectral gravity forward modelling algorithm

The used spectral gravity forward modelling algorithm was developed by Root et al. (2016) as part of his PhD project. Here, only the algorithm's characteristics relevant to this thesis project will be discussed. One does not intend to explain the whole algorithm, as it was mainly used as a black-box.

2.4.1. Analysis and synthesis

The algorithm carries out two main steps: 1) the SHC for a global density structure are computed, which is called *analysis*, 2) the gravitational potential (U), three components of the gravitational acceleration vector (g), and six components of the gravity gradient tensor (GGT) are computed using the SHC from step 1, which is called *synthesis*. Italics is used to increase clarity. The main inputs to the algorithm are global depth fields and corresponding density fields for each modelled layer. For the *analysis* the maximum SHC d/o l_{max} needs to be specified, together with parameters related to the planetary body, e.g. radius (R), standard gravitational parameter (μ), and geoid. Moreover, global longitude-latitude grids of depth and density are required for each desired layer. For the *synthesis* the SHC truncation settings are required as input, together with the height for which the synthesis is performed. Moreover, the region and resolution for the *synthesis* can be specified.

The *analysis* is done using the Fast Spectral Method (FSM), which is based on the binomial series expansion method used to solve the spherical harmonic-based volume integral (Pavlis and Rapp, 1990). This is done faster compared to other methods, from which FSM derives its name. The MATLAB® software for FSM has a maximum truncation limit of $\alpha_{bin,max} = 8$ for the binomial series. Root et al. (2016) verified that a truncation limit of $\alpha_{bin} = 2$ provides accurate results ($\sim$ 1 mGal) for topographic masses modelled up to SHC d/o 180, corresponding to a spatial resolution of 1 degree (Balmino et al., 1973; Rummel et al., 1988; Martinec et al., 1989).

This forward modelling algorithm uses a spherical harmonic representation of the global gravitational potential fields. Benchmarking against a tesseroid geometry approximation of Kaban et al. (2010) showed that, as long as the convergence criterion (explained below) is met, the accuracy of FSM stays within the uncertainties of global forward modelled gravity fields.

2.4.2. Convergence of forward modelling algorithm

FSM has convergence problems for higher d/o SHC and large layer depths. In other words, large errors will occur for the higher d/o SHC when deep layers are forward modelled. Adhering to the limit (*criterion < 0.5*) given in Figure 2.9 will allow for correct gravity modelling. This figure gives a relation between the maximum layer depth and the required SHC truncation for which an acceptable error level is obtained for the binomial series truncation ($\alpha_{bin} = 3$). For example, if a density distribution has a maximum depth of 100, 200, and 400 km from a given reference sphere, large errors will be present in SHC d/o higher than 80, 50, and 25, respectively. Important to note that this maximum depth is defined with respect to the upper boundary of a certain layer (Root et al., 2016), so extra caution is required when forward modelling thick layers, where the base will be significantly further away from the reference sphere than the top.

Fortunately, the forward modelling algorithm automatically adjust the reference sphere to the upper boundary of the input density model when no material is present above that layer. This reduces the upper boundary to an artificial depth of 0 km. Input models that exceed the maximum depth of the

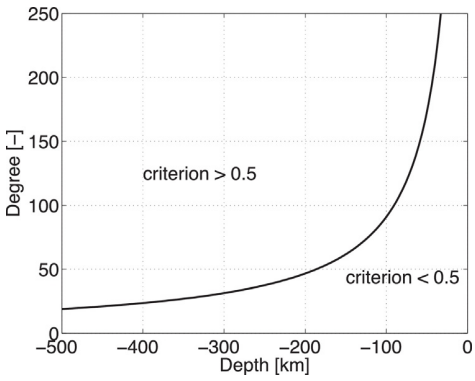

Figure 2.9: Maximum modelling depth for different SHC upper limits ($\alpha_{bin} = 3$) (Root et al., 2016)

convergence criterion are vertically segmented into virtual layers, after which the FSM is applied. The vertical segmentation settings used throughout this thesis were 50 and 100 km, corresponding to SHC truncation settings of 180 and 90. Synthesis is applied using the summation of SHC for all virtual layers, which results in the gravity signal for the full input model.

Dividing the input boundary models into virtual layers, and performing the analysis on every layer individually is very computationally expensive. Forward modelling for higher SHC degrees would not only mean a more computationally expensive FSM, but also performing this for more virtual layers to adhere to the convergence criterion, by applying a denser vertical segmentation. Therefore, it is important to find the optimal truncation settings which minimize computation time, while adhering the convergence criterion in Figure 2.9.

Concluding, there are two methods that can be used to obtain correct forward gravity results, despite the truncation error of the binomial series: 1) allow for additional terms, e.g. increase α_{bin}, in the binomial series, 2) divide the input density model into virtual vertical segments. Both methods would proportionately increase the computational effort. The convergence criterion is only computed for $\alpha_{bin} = 3$ in Root et al. (2016), therefore, a default truncation of $\alpha_{bin} = 3$ was used to allow for quick determination of the relation between SHC truncation settings and maximum layer depth, based on Figure 2.9. Other studies also only used the first three terms of the binomial series (Rummel et al., 1988; Vaníček et al., 1995).

3

Models for lithosphere

The oceanic lithosphere is the layer that is subducting at a convergence plate boundary, also called subduction zone (Vermeersen, 2015). The oceanic lithosphere subducts under the continental lithosphere because it is heavier. To understand the properties of the subducting oceanic lithosphere, from now onwards called slab, it is important to study the general properties of the oceanic lithosphere, and to find ways to use those properties for slab modelling.

The first part of this chapter will discuss the derivation of the lithospheric age distribution at the trench, and secondly, an innovative approach used to convert that distribution to a first-order age approximation for the entire slab.

The second part of this chapter will explain how the thickness distribution of the slab is computed using lithospheric age. Lastly, different density values will be reviewed that have been used in literature for the lithosphere, slab and mantle.

3.1. Age of oceanic lithosphere

The global oceanic lithospheric age model by Müller et al. (2008) is used for computing the lithospheric age, and subsequently, the lithospheric thickness. The model is grid-line registered and has a resolution of 6 arc-minutes, which corresponds to 0.1°. This model used interpolation in spreading direction of seafloor isochrons to compute the lithospheric age and spreading rate. The isochrons are based on ship-tracked magnetic anomaly data (Müller et al., 2008). An age contour plot for the extended Sumatra region is given in Figure 3.1. As can be seen from this figure, age data is only available for regions with oceanic lithosphere. No data is available for the subduction zone, which spans between the red-blue-black line until the dotted green line. To deal with this problem, one decided to constrain the slab with respect to its conditions at the trench, which allows for imposing additional degrees of freedom on the slab itself, e.g. different thickness distribution. Therefore, no age data within the subduction itself is required. This new way of slab modelling will be elaborated upon in Subsection 4.4.2.

3.2. Lithospheric age along-trench

To obtain the oceanic lithospheric age at the trench, four operations were performed. All the references are made with respect to Figure 3.1. The first problem was that the trench did no overlap with the oceanic lithospheric age data between the latitudes of -7° and 25°. Therefore, the trench for those longitudes was shifted westward by 0.3° to ensure consistent overlap with the age model (see blue line). Important to note that this shifted part of the trench was only used to retrieve the corresponding trench age from the age model. This retrieved age data would then be applied back to the corresponding original trench. The second operation was to extract the age data on the trench using linear interpolation (over black and dotted blue lines), as the grid of the trench and age coordinates were not the same. For the third operation the along-trench distance starting at the most northern trench point was computed, which was used to plot the along-trench age data. For the most northern part of the trench no age data was available, and shifting the trench would not solve this problem. The final operation was to

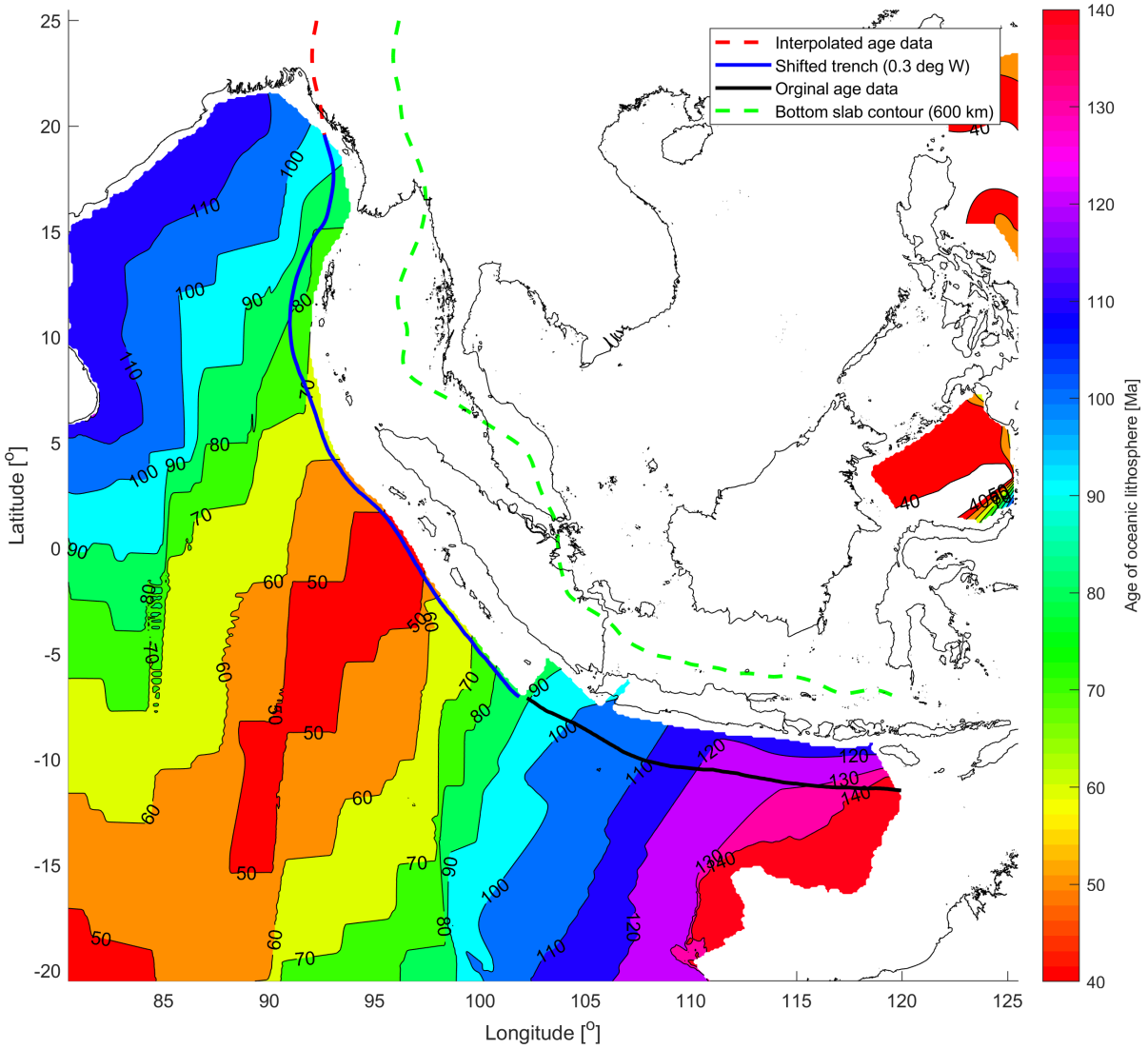

Figure 3.1: Contour plot for the *Age of Oceanic Lithosphere* (Müller et al., 2008), all the additional plotted lines (red, blue, black, green) are based on the combined top-slab model (Figure 4.2)

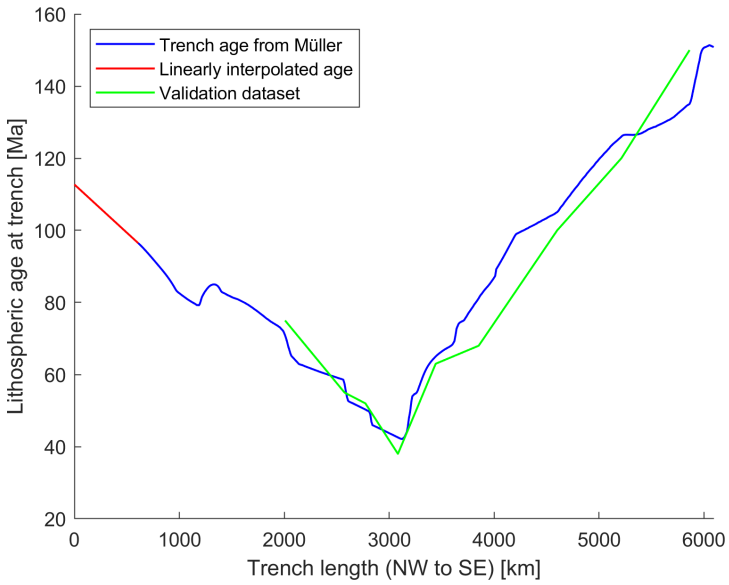

Figure 3.2: Lithospheric age from Müller et al. (2008) along the trench, validation dataset (green) from Jacob et al. (2014)

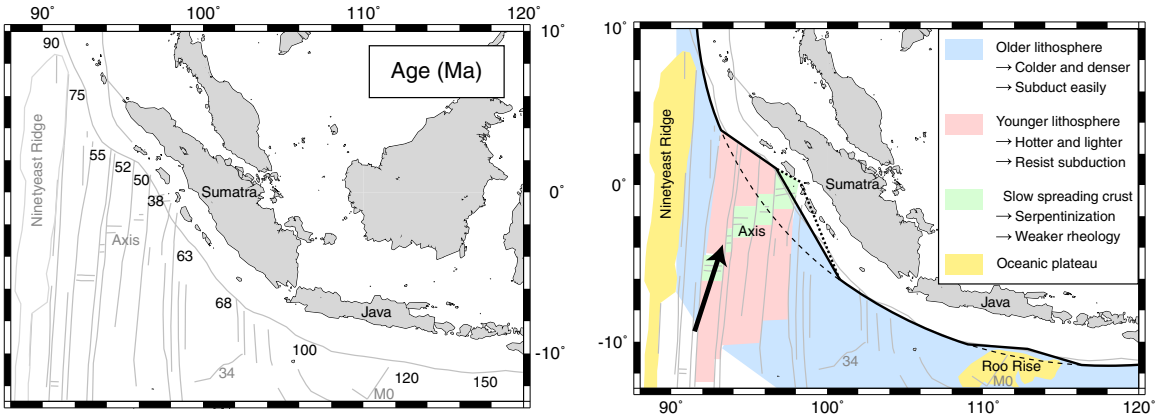

(a) Lithospheric age at trench

(b) Schematic of lithospheric characteristics

Figure 3.3: Lateral age values and schematic for the Sumatra subduction zone (Jacob et al., 2014, Fig. 10, Fig. 11)

interpolate the along-trench age data for the blue line to that part of the trench, shown in dotted red in Figure 3.1.

Figure 3.2 gives the final along-trench oceanic lithospheric age distribution, where the red line corresponds to the interpolated part along the dotted red line in Figure 3.1. The trench age increases from 40 Ma for northern Sumatra region unto 150 Ma for the region south-west of Java. In northward direction from the minimum age at northern Sumatra, the trench age also increases, to a maximum value of approximately 90 Ma in the Andaman Sea. The previously mentioned ages are in correspondence with literature. Figure 3.3a shows similar trench ages of 38-50 Ma at northern Sumatra, 100-150 Ma south of Java, and 75-90 Ma for the Andaman Sea (Jacob et al., 2014). The reference values (green) in Figure 3.1 show good correlation with the computed trench age, which validates both method for computing the trench age as the age model by Müller et al. (2008).

Figure 3.3b shows that younger lithosphere is subducting under northern Sumatra. Younger lithosphere is said to resist subduction, as it is lighter than older lithosphere, which is related to the indentation of the trench at this location (Jacob et al., 2014). This feature is also observed in Figure 3.1, where the region with the youngest lithosphere (dark red contour) is located at the indentation of the trench at northern Sumatra.

3.3. Thickness of oceanic lithosphere

Now that the along-trench oceanic lithospheric age has been determined, the trench thickness can be computed. The thickness of the oceanic lithosphere can be estimated using either thermal or seismic modelling. Thermal modelling, and more specifically, plate cooling models, directly relate lithospheric age to lithospheric thickness using empirical relations.

Three cooling models will be discussed and used: the Half-Space Cooling model (HS) by Turcotte and Schubert (1982), and the plate models, Parsons, Sclater and McKenzie model (PSM) (Parsons and Sclater, 1977) and Global Depth and Heat model (GDH1) (Stein and Stein, 1992). Those three models were selected because they are the most widely used relations for lithospheric thickness computations due to their simplicity and accuracy (Kirby et al., 1996; Fowler, 2005; Lowrie, 2007). The models are similar in a sense that they relate age, heat flow, mantle temperature, lithosphere temperature to lithospheric thermal thickness or ocean depth. However, the models differ in their definition at which temperature the boundary between lithosphere and asthenosphere occurs.

For Half-Space Cooling models (HS) the lithosphere is defined by an isotherm, therefore the plate thickness is able to grow indefinitely. On the other hand, plate models assume a constant thickness (L) for the lithosphere, which is the asymptotic thermal thickness of old oceanic lithosphere (Scheidegger, 1982; Lowrie, 2007). Plate models are fitted to ocean depth and heat flow measurements, and therefore tend to be accurate representations. Those models work better away from the mid-ocean ridges, or in other words, for older lithosphere.

The plate model by Parsons and Sclater (1977) uses a plate thickness (L) of 125 km and a base temperature of 1350°, whereas the GHD1 model by Stein and Stein (1992) uses 95 km and 1450°, respectively. GDH1 only uses empirical data from North Pacific and Northwest Atlantic (Stein and Stein, 2013). The differences in used boundary conditions for the different models are given in Table 3.1, where the plate thickness (L) for HS is by definition undefined.

Literature has two different views on how to compute the oceanic lithospheric thickness. In essence, one school assumes that the original HS cooling model is accurate unto ~120-150 Ma (Sandwell, 2001; Steinberger and Becker, 2016), whereas the other school only credits validity up unto 70 Ma based on the assumption that older lithosphere is in thermal equilibrium with the asthenosphere (Fowler, 2005; Jacob et al., 2014). One school uses HS, whereas the other school uses plate models (e.g. GDH1, PSM).

For this research both methods were combined into a method called the weighted HS model, see Equation 3.3. The original HS model by Turcotte and Schubert (1982) is given in Equation 3.1. The ratio of 2.32 is taken from Jacob et al. (2014) and based on an approximate lithosphere-asthenosphere temperature difference of 10%, where the error function (**erf**) is given in Fowler (2005, Tab. A5.1). The weighted HS is computed using the original HS together with a weighting factor (Λ), see Equation 3.2. The weighting factor is computed using the PSM and GDH1 depth parameters are given in Equation 3.4, 3.5 and 3.6. The PSM-GDH1 weighting factor accounts for the fact that PSM gives good approximations for younger lithosphere, and GDH1 has a better empirical fit for older lithosphere (Stein and Stein, 1992). The weighted HS model maintains the simplicity of the HS mathematical description while ensuring that the lithospheric thickness convergences towards an asymptote. The weighted HS model has previously been used for the Sumatra subduction zone by Jacob et al. (2014).

Comparing original HS results with lithospheric thicknesses derived from tomographic models lead to two observations. Firstly, for ages between 10 and 120 Ma there is a good fit with minor deviations of ~5 km. Secondly, the HS cooling model under-estimates the heat flow for ages above 120 Ma, which leads to an over-estimation of ~20 km for the lithospheric thickness compared to tomographic models (Steinberger and Becker, 2016, Fig. 3). This inaccuracy in the heat flow estimation in HS is well-known and linked to incorrect estimates of the thermal diffusivity (κ) and the inability for HS to approach an asymptotic thickness (Sandwell, 2001; Lowrie, 2007). Using the weighted HS meant that the accurate part of the HS was used, whereas the inaccurate range (>120 Ma) were adjusted for by weighting.

Table 3.1: Constants used for thermal modelling of the oceanic lithosphere for: Global Depth and Heat model (GDH1), Parsons, Sclater and McKenzie model (PSM), and Half-Space Cooling model (HS) (Fowler, 2005, Tab. 7.4)

Symbol	Parameters	**GDH1**	**PSM**	**HS**
L	Plate thickness $[km]$	95 ± 10	125 ± 10	-
T_a	Temperature at base of plate $[°C]$	1450 ± 100	1350 ± 275	1365 ± 10
α	Coefficient of thermal expansion $[°C^{-1}]$	3.1×10^{-5}	3.28×10^{-5}	3.1×10^{-5}
k	Thermal conductivity $[W/m]$	3.138	3.138	3.138
c_p	Specific heat $[kJ/kg]$	1.171	1.171	1.171
κ	Thermal diffusivity $[m^2/s]$	0.804×10^{-6}	0.804×10^{-6}	0.804×10^{-6}
ρ_m	Mantle density $[kg/m^3]$	3330	3330	3330
ρ_m	Water density $[kg/m^3]$	1000	1000	1000
d_r	Ridge depth $[km]$	2.6	2.5	2.6

The original HS (Equation 3.1), and weighted HS (Equation 3.3), together with the weighting factor are given below:

$$\frac{T_l}{T_a} = \mathbf{erf}\left(\frac{L}{2\sqrt{\kappa t}}\right) \rightarrow L(t) = 2.32\sqrt{\kappa t} \tag{3.1}$$

$$\Lambda = \frac{d_{GDH1}(t) - d_0}{d_{PSM}(t) - d_0} \tag{3.2}$$

$$L_{weighted} = \Lambda \cdot 2.32\sqrt{\kappa t} \tag{3.3}$$

Where a thermal diffusivity (κ) of 1E-6 m^2/s was used, the lithospheric age (t) is in seconds, and the lithospheric thickness by the weighted HS model ($L_{weighted}$) in meters. The thermal diffusivity (κ) is the fraction $k/\rho c_p$, where k is thermal conductivity, ρ density, and c_p specific heat. The most commonly used values for thermal diffusivity (κ) are 8×10^{-7} and 1×10^{-6} m^2/s.

For $0 < t < 70$ Ma, the PSM model for oceanic depth is given as (Parsons and Sclater, 1977, Eq. 21):

$$d_{PSM}(t) = 2500 + 350\sqrt{t} \tag{3.4}$$

For $t \geq 20$ Ma, the GDH1 model for oceanic depth is given as (Stein and Stein, 1992):

$$d_{GDH1}(t) = 5651 - 2473\exp(-0.0278t) \tag{3.5}$$

$$d_0 = d_{GDH1}(t = 0) = 5651 - 2473 = 3178m \tag{3.6}$$

Where the age (t) is in Ma, and the depths (d) are given in meters. The age-to-thickness conversion was checked with values from Jacob et al. (2014), and one concluded that the used model approaches an asymptotic value of 108 km, whereas the reference data shows a different pattern. This is because Jacob et al. (2014) did not use the standard PSM and GDH1 expressions, and unfortunately did not document the used custom parameters.

Table 3.2 gives the computed thickness values for different lithospheric ages, with and without weighting. Furthermore, reference values from Jacob et al. (2014) are included to validate the results. A comparison between the original (Equation 3.1) and weighted HS model (Equation 3.3) is given in Figure 3.4 for two values of thermal diffusivity (κ). The weighted HS model is only accurate for lithosphere older than 10 Ma. This limitation is no problem, as the age range for which computations are required is between 40-150 Ma, see Figure 3.2. Moreover, a reference HS is plotted for $\kappa = 1\times10^{-6}$ m^2/s, $T_l = 1100°$, $T_a = 1300°$, resulting in a lithosphere-asthenosphere temperature difference of $\sim 18\%$ (Fowler, 2005). In Figure 3.4 shows that an increase in thermal diffusivity (κ) leads to an increase in oceanic lithospheric thickness (L), both for the original and weighted HS. The original HS overestimates the thickness with respect to the reference HS because a lower lithosphere-asthenosphere temperature difference of 10% is used for the original HS. Figure 3.4 also shows the unboundedness of the original HS, and that applying a weighting factor (Equation 3.2) results in a bounded and realistic age-thickness distribution.

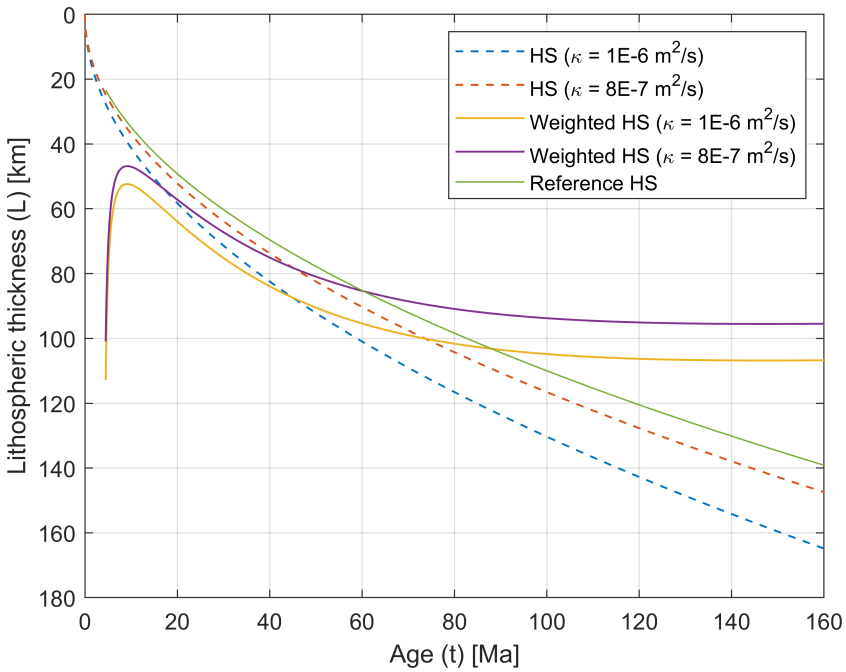

Figure 3.4: Original and weighted Half-Space Cooling model for two thermal diffusivity (κ) values

Table 3.2: Results for age-based thickness computations using the original and weighted HS, reference values from Jacob et al. (2014)

Lithospheric age (input)	**38**	**55**	**63**	**75**	**120**	**150**
Thickness without weighting [km]	80.3	96.6	103.4	112.8	142.7	159.6
Thickness with weighting [km]	87.6	97.6	100.6	103.8	107.9	107.7
PSM-GDH1 weighting-factor [-]	1.090	1.010	0.973	0.920	0.756	0.675
Reference thickness [km]	85	97	103	105	113	115
Reference density [kg/m^3]	3264	3268	3270	3271	3273	3273

Surface wave dispersion studies of the oceanic lithosphere resulted in two conclusions. Firstly, flattening of the lithospheric thickness after 70 Ma, which is also advocated by Stein and Stein (2013). Secondly, the lithospheric thickness at 100 Ma is approximately 100 km (Fowler, 2005, Sec. 9.2.2). Both conclusions are best resembled by '*Weighted HS (κ = 1E-6 m^2/s)*' in Figure 3.4, therefore, the weighted HS together with a thermal diffusivity of 1×10^{-6} m^2/s is deemed the most accurate representation for the lithospheric thickness.

Having the oceanic lithospheric trench age as input, see Figure 3.2, the oceanic lithospheric thickness was computed using both the original and weighted HS for two values of κ. This resulted in the lithospheric thickness distributions along the trench given in Figure 3.5. Where the yellow line (*Weighted HS (κ = 1E-6 m^2/s)* was selected as the most accurate representation, having an oceanic lithospheric thickness that ranges between 85 and 108 km. Again, the unboundedness of the original HS is displayed, which results in unrealistically values for lithospheric thickness (140-160 km).

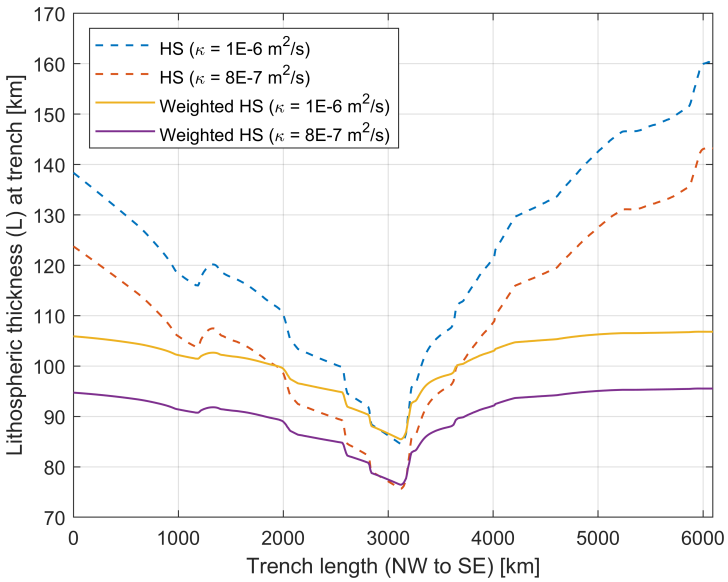

Figure 3.5: Lithospheric trench thickness derived from trench age (see Figure 3.2) using HS, PSM, and GDH1 (Turcotte and Schubert, 1982; Parsons and Sclater, 1977; Stein and Stein, 1992)

3.4. Density of lithosphere, slab and mantle

The bulk density of the lithosphere is defined to be around 3300 kg/m^3 (Capitanio et al., 2015; Gutknecht et al., 2014; Jacob et al., 2014). However, for gravity modelling one is more interested in the density contrast between layers. According to Cloos (1993), the lithosphere-asthenosphere contrast is ~30 kg/m^2 for young plates, and ~100 kg/m^2 for older plates. Based on this information, one generally uses a 40-80 kg/m^2 slab-mantle contrast. More specifically, the lithosphere-asthenosphere contrast for a 80 Ma old oceanic lithosphere with a 7 km basaltic crust is ~40 kg/m^2. For a subducting slab, this density contrast can increase to 80 kg/m^2 due to material transitions, e.g. transition from basalt or gabbro to more dense materials like eclogite and amphibolite. A continental lithosphere of 100 km has a negative density contrast of ~90 kg/m^2, assuming a granitic crust of 30 km (Cloos, 1993).

Capitanio et al. (2015) used a oceanic lithosphere-mantle contrast of 75 kg/m^2, where one assumed that continental lithosphere contrasts range between -100 kg/m^2 to 45 kg/m^2. The mantle density is usually taken as 3200 kg/m^2, with a slab density contrast of 60 kg/m^2 (Zhang et al., 2017). Moreover, the bulk density of the lithosphere is also dependent on its thickness (Jacob et al., 2014). The estimated density corresponding to different sets lithospheric age and thickness is given in Table 3.2, see the reference density row. The density changes from 3264 kg/m^3 for 38 Ma, to 3273 kg/m^3 for 150 Ma, which is a minor density increase of 9 kg/m^3. Therefore, this increase in lithospheric density with age will be neglected in this study.

The Andean subduction zone has plenty of specific density cross-sections (Köther et al., 2012; Hosse et al., 2014). The Sumatra subduction zone has little literature on its detailed density structure. Concluding, different lithosphere-asthenosphere contrasts are being used in literature, ranging from 30 to 100 kg/m^3. In this study a standard density contrast of 50 kg/m^3 will be used between the lithosphere and the asthenosphere, which is in line with other studies in this region (Cloos, 1993; Zhang et al., 2017).

4

Models for slab

The local top-surface slab model based on Slab1.0 (Hayes et al., 2012b) and a version by Broerse et al. (2014) which combines SLab1.0, UU-P07 and RUM, form the starting points for this research project. Model analysis of data quality and sampling in the Sumatra region was carried out, to enhance the understanding on their possibilities and limitations. By the end of this chapter, all the main ingredients for a simple slab model have been discussed and selected.

4.1. Slab1.0

Slab1.0 provides three-dimensional models for different subduction zones. Usage is made of active and passive seismic data, to map the entire slab from the fore arc to beyond the transition zone. Slab1.0 is unique in a sense that it combines a large number of different and independent datasets. Three different earthquake catalogues were incorporated into Slab1.0, gCMT, NEIC PDE, and EHB (Engdahl et al., 2007). The trench break locations on the seafloor are obtained from Tarr et al. (2010), whereas for the sediment thickness map of Divins (2003) is used. Plenty of passive seismic datasets were available in the Sumatra region, of which the following were incorporated: Kopp et al. (2001), (Kopp, 2002), (Simoes et al., 2004), Grevemeyer and Tiwari (2006), (Franke et al., 2008), (Shulgin et al., 2009), and (Lüschen et al., 2011). The Slab1.0 top-slab model extends down to a depth of 600 km.

Slab1.0 interpolates 2D cross-sections along-strike into 3D slab surface geometries. Those 2D along-strike cross-section are generated every 10 km along the trench, and are fitted to EHB and other earthquake catalogues data points, which are filtered for low vertical location uncertainty. For the Sumatra subduction zone 480 2D cross-sections were used. Important to note that, the intermediate depths (80-400 km) earthquake locations are horizontally shifted by 10 km in down-dip direction. This is done to account for the fact that earthquakes at intermediate depths tend to occur in the slab, thus below the interface (Hayes and Wald, 2009). However, for shallow subduction zones (0-80 km) the depth of earthquakes corresponds well with the subducting slab interface, with an approximate error margin of ~5 km (Zhao et al., 1997).

Comparing the top-slab surface of Slab1.0 with averaged earthquake depths provided two conclusions: 1) The region around Java is poorly constrained having depth errors between -80 and 60 km, 2) The top-slab surface around Sumatra is well-fitted due to the availability of more seismic data in the region, the depth errors range from -40 to 10 km (Hayes et al., 2012a).

4.2. Combined top-slab model: Slab1.0, UU-P07, and RUM

This section will deal with the top-slab surface model from Broerse et al. (2014), which combines Slab1.0 (Hayes et al., 2012b), with seismic model RUM (Gudmundsson and Sambridge, 1998), and tomographic model UU-P07 (Amaru, 2007). This top-slab model is one of the most important inputs for this thesis, and is from now on referenced as combined top-slab model. Slab1.0 is fully incorporated into the combined top-slab model, see blue lines in Figure 4.1. For regions where there was no Slab1.0 data was available, RUM was used at depths of 0, 50 and 100 km (blue lines), and for

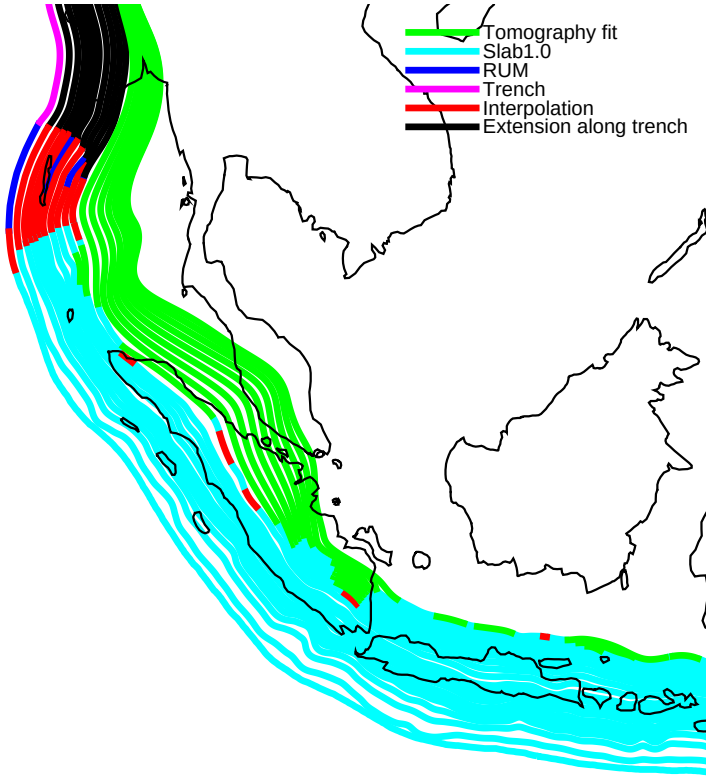

Figure 4.1: Data sources for the combined top-slab model (Broerse et al., 2014) using Slab1.0 (Hayes et al., 2012b), seismic model RUM (Gudmundsson and Sambridge, 1998), and tomographic model UU-P07 (Amaru, 2007)

deeper depths UU-P07 was used (green lines). The slab model between latitudes 15 and 25° is obtained through extrapolation along the trench, therefore, the results for this region should be treated with caution (Broerse et al., 2014). The combined model data is not represented by a uniform grid, but is given using a contour line representation, see Figure 4.2. This means that every line corresponds to a specific depth, and on those lines the strike-angle and dip-angle are given.

To perform the required gravity analysis and synthesis, the input data needs to be in cell-registered grid form. Therefore, the contour lines were interpolated generating a meshed surface with grid-points corresponding to the other models (topography, bathymetry, sediments). This was done using the built-in MATLAB® function *scatteredInterpolant*, which fits a surface $v = F(x,y)$ to the given scattered input data using Delaunay triangulation (Amidror, 2002).

Three different methods were tested for accuracy and smoothness: *linear*, *natural*, and *nearest neighbour*. The Slab1.0 region was used for benchmarking, because in this region the contour lines of the combined model were constructed solely based on Slab1.0. Moreover, the externally obtained Slab1.0 grid could be used as a validation dataset (Hayes et al., 2012a). The *nearest neighbour* interpolation was unable to generate accurate results. The residuals oscillate between large positive values (25 km) and negative values (-30 km), especially for the deeper regions of the combined top-slab model, see Figure 4.3f. The *nearest neighbour* interpolated results in Figure 4.3e show that there is no smooth top-slab distribution, but a step-wise decrease in depth. Instead of fitting a surface through all contour points and minimizing the total residual as is done for *natural* and *linear*, the *nearest neighbour* is limited to the depth resolution provided by the combined model, which ranges between step-sizes of 10 km and 50 km. For example, if a grid point is between the depth contour lines of 400 and 450 km, but closer to the 400 km contour line, it takes on the value of 400km, whereas the neighbouring grid point might be closer to the 450 km contour line, therefore it takes on the 450 km value. Therefore, the interpolated top-slab surface could jump by a maximum of 50 km from one grid point to the next grid point. This is an unacceptable and unnecessary error for subduction zone modelling, therefore *nearest neighbour* method is not considered any further.

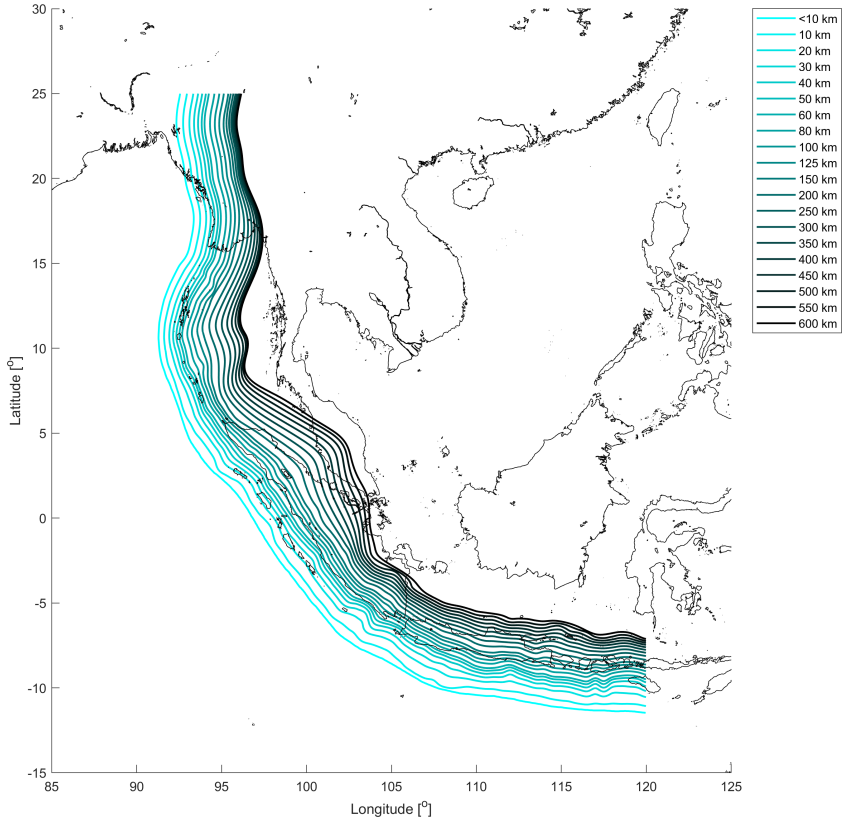

Figure 4.2: Contour lines for the combined top-slab model (Broerse et al., 2014)

Interpolation using *natural* and *linear* resulted in residuals ranging between -6 km and 6 km, where *natural* interpolation resulted in ~50 m lower residuals compared to *linear*, see Figure 4.3b and 4.3d. The better performance of *natural* was deemed insignificant compared to the absolute values of the residuals (~6 km). Therefore, *linear* interpolation was selected due to its superior computational efficiency. An error of 6 km was acceptable, knowing that the uncertainty in the input model, e.g. Slab1.0, was in de order of 10-80 km, see the discussions in Section 4.1.

The strike and dip-angles of the top-slab were also interpolated, see Figure 4.4. The strike-angle reflects on the smoothness of the top-slab surface, rapid changes in strike-angles indicate a rugged surface, whereas regions with relatively constant strike-angles are likely to be smooth. Dip-angle also reflects on the smoothness of the surface, and moreover, on the steepness with which the slab subducts. Large dip-angles are observed for the deep slab segments in the northern and southern regions of the Sumatra subduction zone. For the central part the dip-angle changes more slowly, and therefore, the slab will increase in depth more gradually.

Comparing Figure 4.10 with Figure 4.4 in the northern Sumatra region, it is interesting to see that the shallow dip-angles show correlation to the region with young lithospheric slab material. Moreover, this same region also has a relative constant strike angle. Younger lithosphere is warmer and therefore has a relatively lower density compared to older lithosphere (Jacob et al., 2014). Due to being lighter, young lithosphere subducts less easy than old lithosphere, which might be the cause for the shallow dip-angles correlating to the relatively younger slab in the northern Sumatra region.

4.3. Top-slab-perpendicular thickness

One observed that defining the slab thickness vertically would lead to inaccurate slab models. Therefore, the slab thickness was defined to be perpendicular to the top slab surface, in other words, the dip-angles (δ_D) and strike-angles (θ_S) were taken into account. Be reminded that the input model for the top-slab exists of contour lines, see Figure 4.2. This slab modelling assumes that the slab thickness varies in trench-perpendicular direction. The following steps were executed:

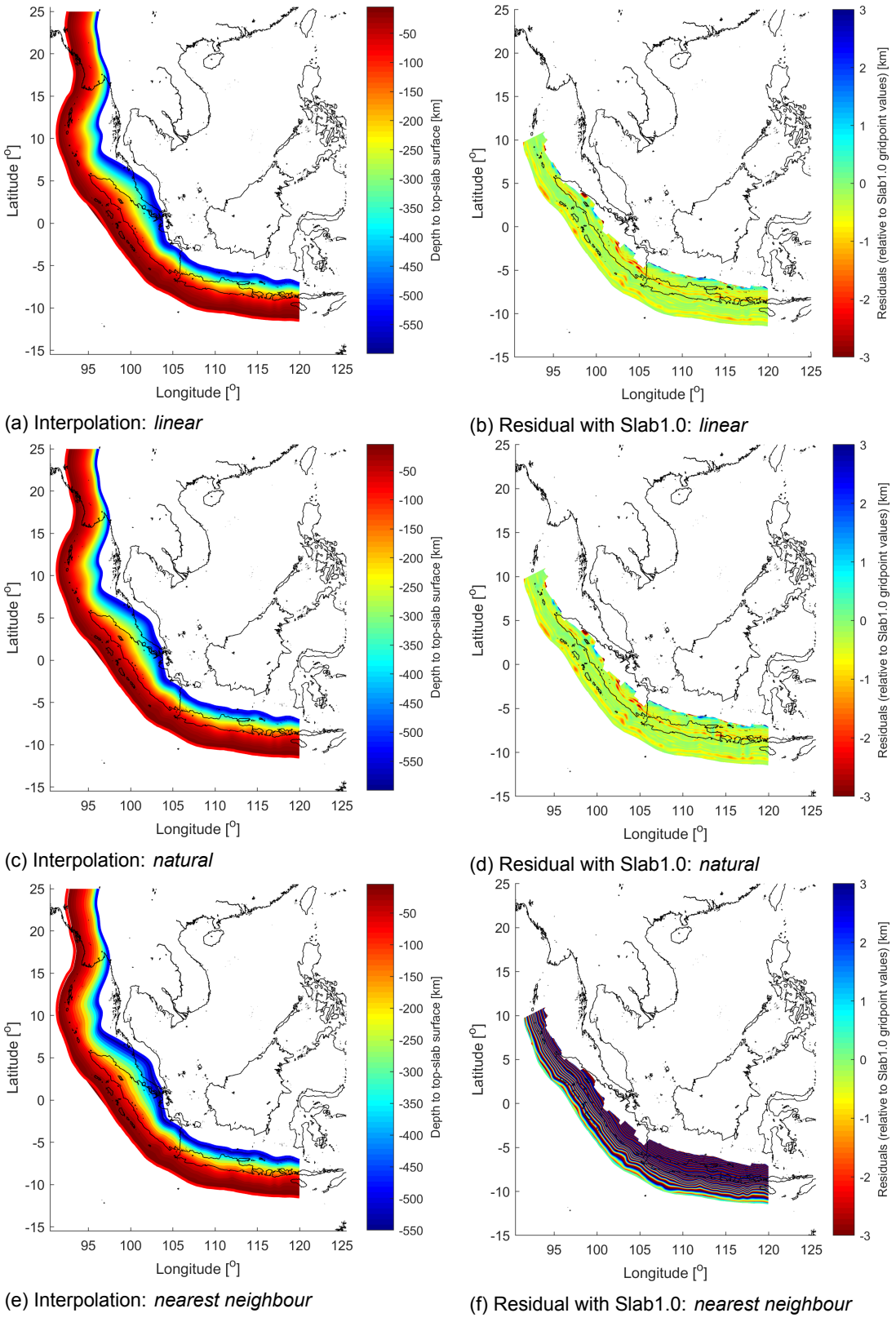

(a) Interpolation: *linear*

(b) Residual with Slab1.0: *linear*

(c) Interpolation: *natural*

(d) Residual with Slab1.0: *natural*

(e) Interpolation: *nearest neighbour*

(f) Residual with Slab1.0: *nearest neighbour*

Figure 4.3: Results for *scatteredInterpolant* in MATLAB® of combined top-slab model using different methods

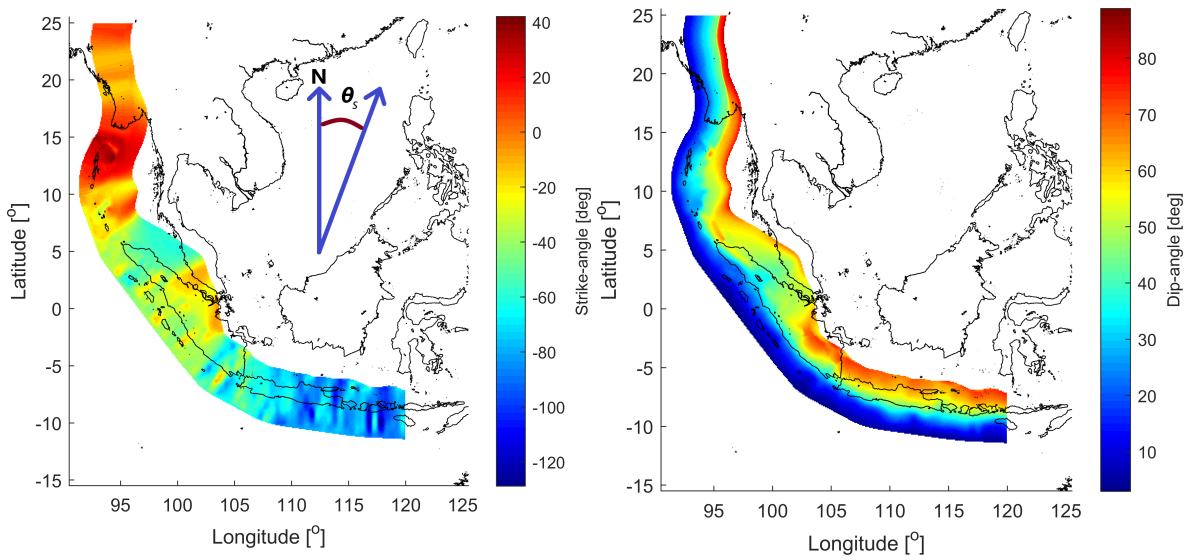

(a) Strike-angle (θ_s)

(b) Dip-angle (δ_D)

Figure 4.4: Interpolated strike and dip-angles (Broerse et al., 2014)

1. Depending on the methodology, either a thickness distribution for the whole subduction is provided, or a thickness distribution for each contour line. The dip-angles (δ_D) and strike-angles (θ_S) are used from the combined top-slab model, see Section 4.2.

2. For every point on the top-slab surface the longitude (ϕ_b), latitude (λ_b) and depth (c) to the corresponding bottom-slab point is computed using a given thickness (t_{slab}). The identifier i corresponds to an arbitrary point on the top-slab surface. See Figure 4.5 for the graphical representation of the different variables used in the equations below:

$$a_i = t_{i,slab} \cdot \cos(\delta_{D,i}) \qquad b_i = t_{i,slab} \cdot \sin(\delta_{D,i}) \tag{4.1}$$

$$c_i = a_i + d_i \tag{4.2}$$

$$\Delta\phi_i = b_i \cdot \sin(\theta_{S,i}) \qquad \Delta\lambda_i = b_i \cdot \cos(\theta_{S,i}) \tag{4.3}$$

$$\phi_{i,b} = \lambda_i + \Delta\phi_i \qquad \lambda_{i,b} = \lambda_i + \Delta\lambda_i \tag{4.4}$$

   Where d is the depth to a point on the top-slab, a and b are the vertical and horizontal shift between top and bottom slab points, respectively.

3. To ensure that the bottom-slab and the lithosphere connect at beginning of the subduction zone, a vertical slab thickness was applied at the location of the trench. Moreover, the 600 km depth contour line was added to the bottom-slab contour lines to create a boundary closing the gab between the top and bottom of the slab.

4. Linear interpolation (*scatteredInterpolant* in MATLAB®) was used to fit a 3D surface through the bottom-slab contour points ($\phi_{i,b}$, $\lambda_{i,b}$, c_i) resulting in a bottom-slab surface.

Incorrect results were obtained for the bottom-slab surface for the initial runs of the algorithm explained above. After inspection of the different inputs, large outliers were identified in the strike and dip-angle data which caused inconsistent locations and depths bottom-slab (ϕ_b, λ_b, c). For instance, the strike-angle data for 100 km depth clearly shows the presence of outliers, see Figure 4.6. Here, one minor and three major outliers were identified using visual inspection. A new dataset for strike and dip-angle was created by removing all the outlier entries. The algorithm was able to construct correct bottom-slab surfaces using this new dataset.

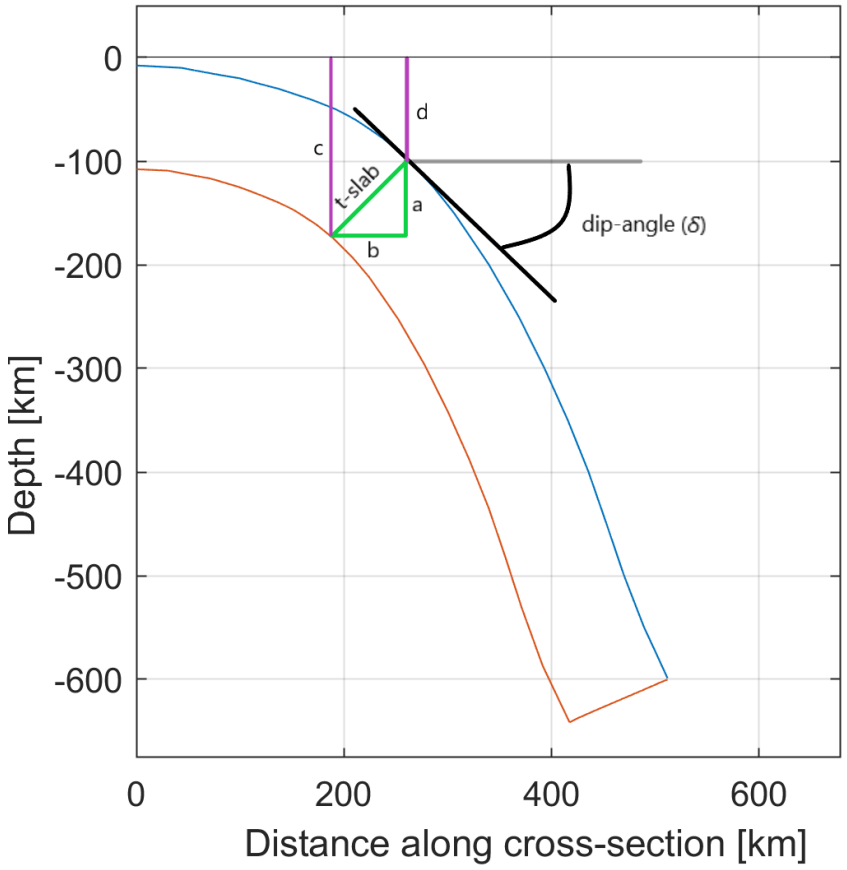

Figure 4.5: Parameters used to model the bottom-slab using a top-slab perpendicular slab thickness

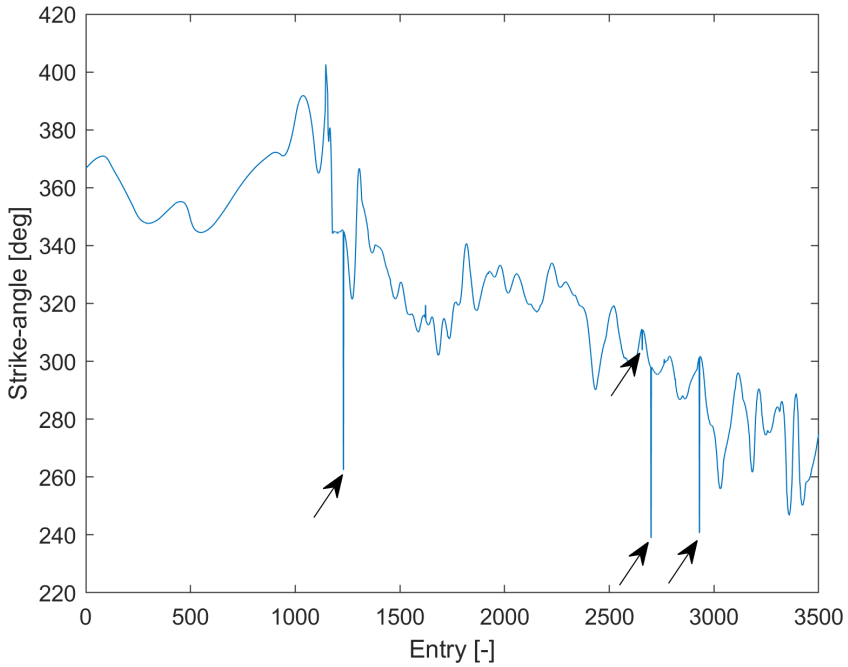

Figure 4.6: Outliers in strike-angle data for 100 km depth (Broerse et al., 2014)

4.4. Slab thickness distribution

The assumption that the slab has the same thickness distribution across the whole subduction zone is an oversimplification. A tomographic cross-section through Java shows that the slab has a significantly varying thickness, see Figure 4.7. Two methodologies to apply varying slab thickness were constructed and tested: a thickness gradient applied in dip-direction, and a thickness distribution based on subduction rate and direction.

4.4.1. Thickness gradient applied in dip-direction

By subtracting a lithospheric thickness distribution from the top-slab surface contour lines, one could approximate the bottom-slab surface contour lines. Allowing for degrees of freedom in the lithospheric thickness distribution, by applying scaling factors on the thickness distribution contour lines, resulted in a contour-dependent variable thickness distribution. The bottom contour lines were calculated with the methodology explained in Section 4.3. The following inputs were required:

- Top-slab contour lines (Figure 4.2) from the combined top-slab model explained in Section 4.2
- Trench thickness profile (yellow line in Figure 3.4) explained in Section 3.3
- Thickness scaling factors for the different contour lines

From literature, one knows that the slab does not have a constant thickness. A constant thickness distribution is shown in Figure 4.8c, where the trench thickness profile extended over the subduction zone in dip-direction. This distribution is obtained by setting all the scaling factors to 1, see Figure 4.8a.

Amongst others, Richards et al. (2007) showed that there might be thinner slab around 400 km depth under Java, see Figure 4.7. Similar results are visible in Pesicek et al. (2010), where P-wave anomalies also show a thinning synthetic slab at 440 km depth under northern Sumatra. Both studies used *ak135* by (Kennett et al., 1995). These slab geometries can also be modelled with the contour-dependent variable thickness distribution, where a show-case is given in Figure 4.8d using the scaling factors given in Figure 4.8b. Here, the slab has half the trench thickness between 400 and 450 km depth, and linearly increasing thickness towards a factor 1.2 for deeper contour lines, which corresponds to the slab given in Figure 4.7. After inspecting Figure 4.8d, it was concluded that this methodology able to create a simple thickness distribution in dip-direction, however, inclusion of information concerning subduction direction or subduction velocity are not possible. As subduction direction and velocity are expected to be more comprehensive and accurate constraints for slab thickness modelling, one choose to neglect the contour-dependent thickness distribution and investigated another methodology, explained in the next section.

4.4.2. Age distribution based on subduction rate and direction

Conventionally the lithospheric age is determined using seafloor magnetic anomalies, like Müller et al. (2008). No magnetic anomalies are available for the subducting slab at Sumatra, therefore no scientific data on the slab age is available, see Figure 3.1. The subduction direction and rate for the Sumatra subduction zone are not constant, but change along trench, having a subduction rate of 64 km/Ma in the south which decreases to 39 km/Ma in the north (Sieh and Natawidjaja, 2000; McNeill and Henstock, 2014). The co-latitude of subduction direction (ϕ_{sub}) changes between approximately 20-30 degrees, when accounting for the North-East fore-arc motion (McCaffrey, 2009).

In this section an innovative way is presented to obtain a first-order estimation of the slab age based on two assumptions that will simplify the approximation. Firstly, the entire slab subducts in the same direction. Secondly, the slab subducts at the same rate as it did at the trench, irrespective of its depth. A constant subduction rate of 55 km/Ma will be used, which is derived from measurements at the central Sumatran trench (McNeill and Henstock, 2014). An algorithm was designed to relate all depth contour points from Broerse et al. (2014) to a trench location and its corresponding age using a co-latitude as constraint. In Figure 4.9 different algorithm outputs are given, where only 1% of the points and connecting lines are displayed to increase visibility. The co-latitude (ϕ) is defined in Figure 4.9a.

For every contour point, the algorithm finds a trench point which best satisfies the co-latitude constraint (ϕ_{sub}). The trench coordinates and age data were discretized using a sample size N_{discr} to fill gabs in

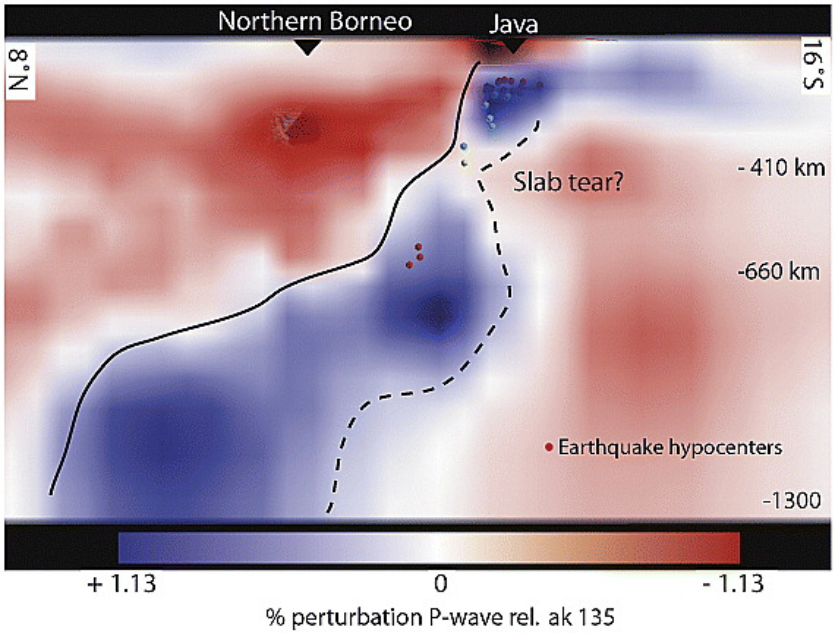

Figure 4.7: Tomographic cross-section (Java-Northern Borneo) for *ak135* (Kennett et al., 1995) showing a varying thickness of fast P-wave velocity anomalies (Richards et al., 2007)

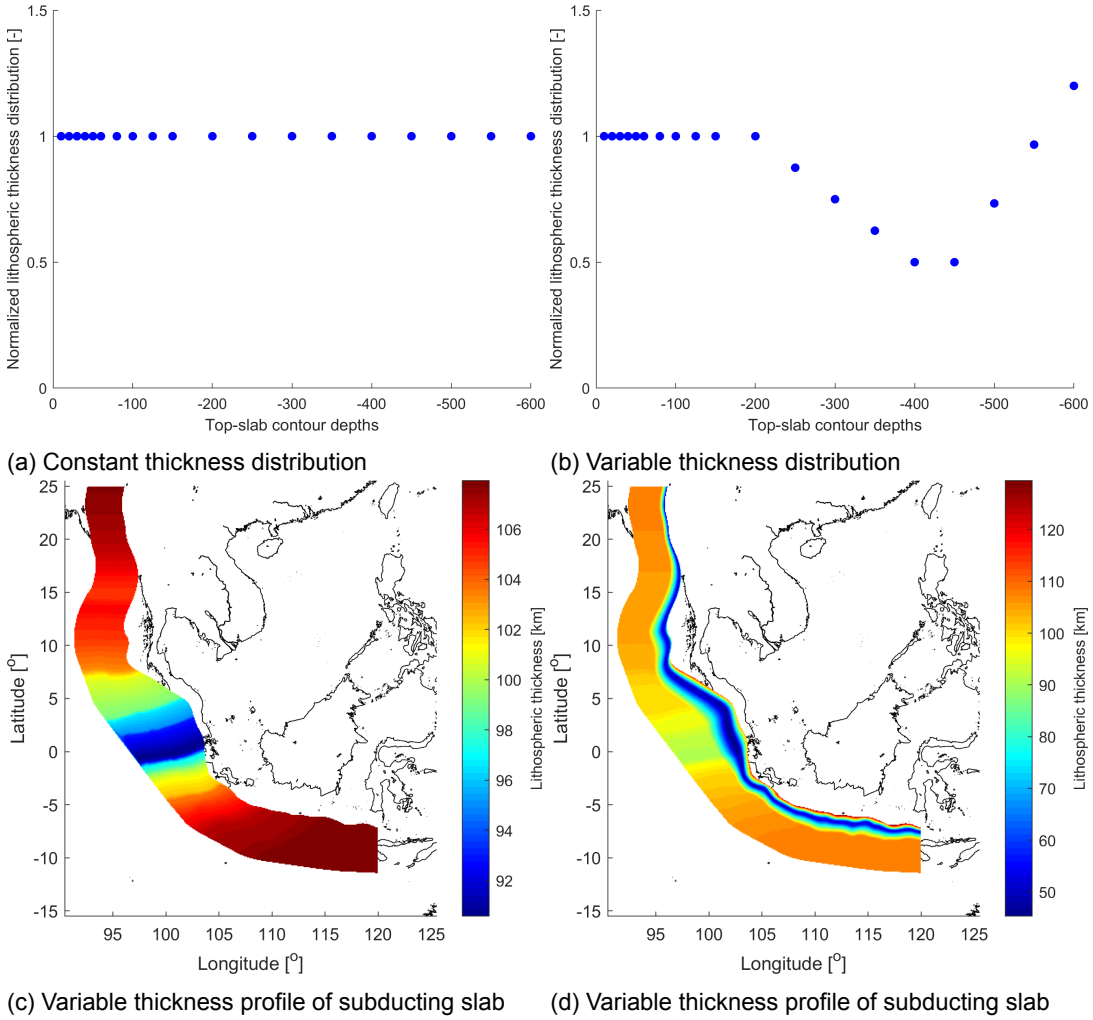

Figure 4.8: Thickness distribution and profiles for slab based on combined top-slab model (see Section 4.2)

the original trench data. The discretization was done using the *griddedInterpolant* MATLAB® function with a *pchip* interpolator. For a contour point there could be multiple trench points that satisfy the co-latitude constraint, see the red and green arrow in Figure 4.9a. To account for this non-uniqueness, the algorithm selects the trench point with the smallest distance measured from a specific contour point, within a subset of trench points that satisfy the co-latitude constraint. The subset is created using the *mink* MATLAB® function, given a maximum number of subset entries (N_{subset}). Figure 4.9b gives the output for $N_{subset} = 20$ using the same discretization. Different combinations for N_{discr} and N_{subset} were analysed. For $N_{discr} = 1E5$ and $N_{subset} = 100$, every single contour point was correctly matched with a trench point, see Figure 4.9c. In the same figure, one sees that between the trench points **b'** and **c'** there is a significant distance which corresponds to difference in trench lithospheric age, which again will result in an age jump on the contour line from point **b** to **c**, instead of having a more realistic distribution, e.g. for the trench in Figure 3.2. Therefore, a minimum ϕ_{sub} of 30° was derived for which all contour lines showed consistent age distributions without jumps. The final algorithm settings are shown in Figure 4.9d, which verifies that realistic output from the algorithm is obtained.

Knowing the distance from trench to contour point, the increment in age with respect to the trench (Δt_{point}) can be computed using a given subduction rate. Adding this increment to the trench age (t_{trench}) results in an age approximation (t_{point}) for that contour point:

$$t_{point} = t_{trench} + \Delta t_{point} = \mathrm{t}_{trench} + \frac{\Delta distance}{rate_{subduction}} \tag{4.5}$$

Realistically, the distance should be measured along the top-slab surface instead of in the horizontal plane. As a first-order approximation, this arc distance is computed as the diagonal between a trench point and the corresponding top-slab contour point at a given depth. This is an accurate approximation for regions where the dip-angle is fairly constant. However, for regions with increasing dip-angle, it will lead to an underestimation of the distance, and therefore result in a conservative estimate of the slab age. In Figure 4.10, the age distribution for a slab subducting with a constant rate of 55 km/Ma in a constant direction of $\phi_{sub} = 30°$ is given, together with a constant age distribution in the same subduction direction of $\phi_{sub} = 30°$. In both figures it is clear that the slab under northern Sumatra is relatively young (~40-60 Ma), whereas the age increases both in southward and northward direction. Old slab is present eastward of Java (>120Ma), which is confirmed by Jacob et al. (2014). For Figure 4.10b, the age gradients in the southern region are more horizontal compared to Figure 4.10a, which is in agreement with the subduction directions corrected for fore-arc motion, derived by McNeill and Henstock (2014, Fig. 1). Those corrected directions basically dictate trench-perpendicular convergence in the Andaman Sea and southward of Java, whereas an oblique convergence is measured at Sumatra, which corresponds with the direction of age change in Figure 4.10b. For the same figure, the maximum age difference between trench and the 600 km depth contour line is in the order of ~12-18 Ma.

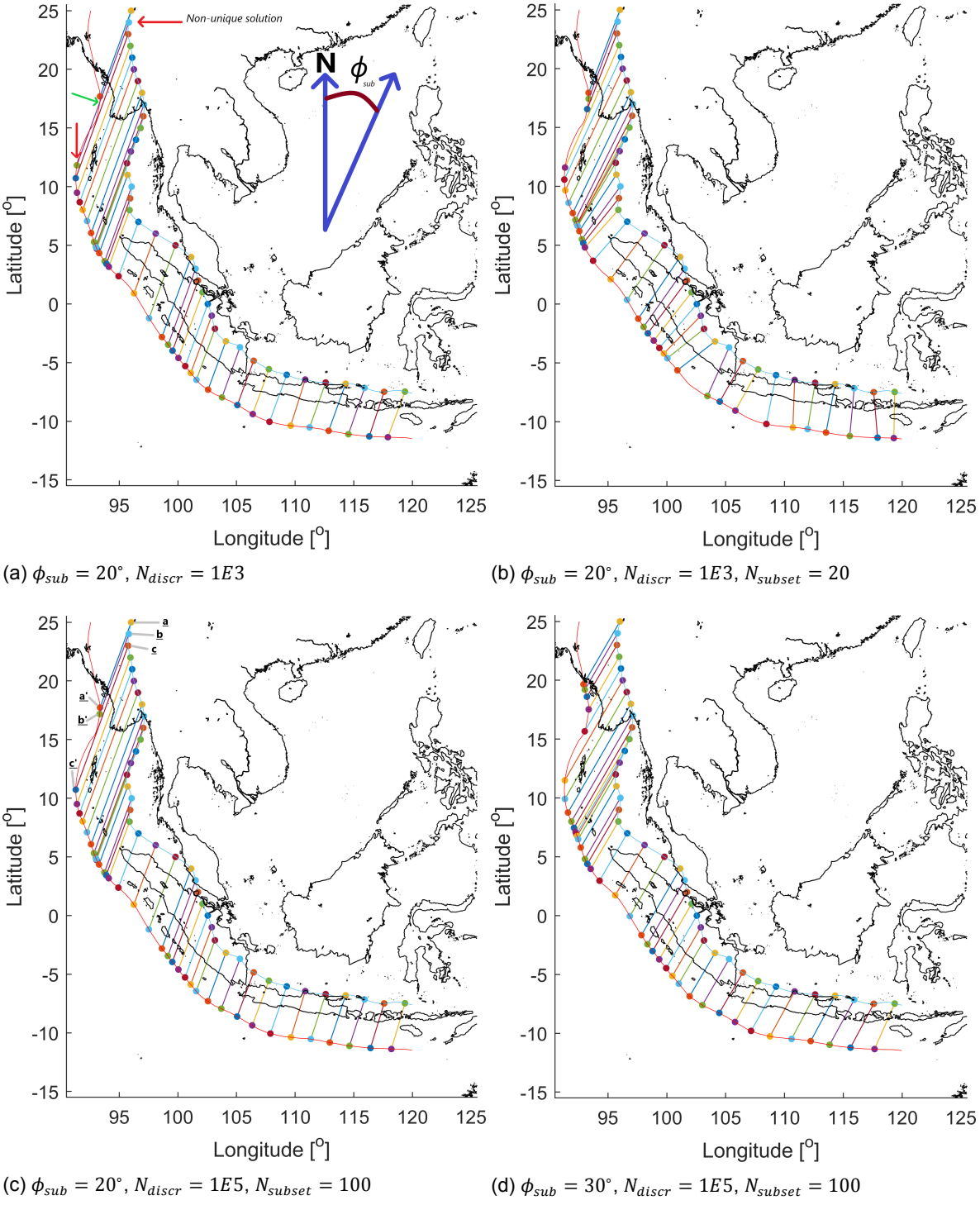

(a) $\phi_{sub} = 20°$, $N_{discr} = 1E3$

(b) $\phi_{sub} = 20°$, $N_{discr} = 1E3$, $N_{subset} = 20$

(c) $\phi_{sub} = 20°$, $N_{discr} = 1E5$, $N_{subset} = 100$

(d) $\phi_{sub} = 30°$, $N_{discr} = 1E5$, $N_{subset} = 100$

Figure 4.9: Slab age propagation algorithm using subduction direction (ϕ_{sub}), only displaying 1% of the output for the 400 km depth contour line

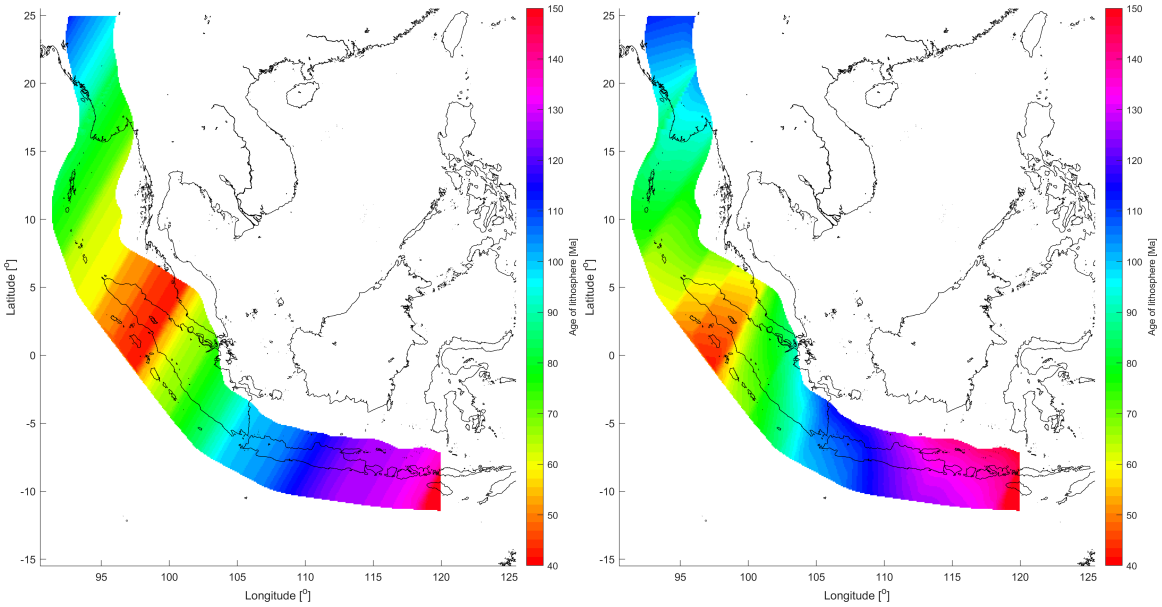

(a) Constant age in subduction direction ($\phi_{sub} = 30°$)

(b) Age based on subduction direction ($\phi_{sub} = 30°$) and subduction rate (50 km/Ma)

Figure 4.10: First-order age approximations for the slab

5

Background model

In this section the different Earth models will be discussed, and incorporated into a full background model. The gravity results of the full background model will shed light on different characteristics of the Sumatra subduction zone, and whether a slab is present in observations model. Four external models will be introduced.

5.1. Input Earth models

The characteristics and accuracy of the four input models are discussed in this section. Moreover, data visualisation are given. All models were freely available online.

5.1.1. Topography and bathymetry model

ETOPO1 is a global land topography and ocean bathymetry model, sampled at a resolution of 1 arc-minute (Amante and Eakins, 2009). 13 different data sources are incorporated. For the Sumatra subduction zone, SRTM30 Topography and GEBCO sea-floor bathymetry are used. The ETOPO1 model for the Sumatra region is shown in Figure 5.2.

5.1.2. Sediment model

The model that is online available and currently has the highest resolution is the *Total Sediment Thickness of the World's Oceans and Marginal Seas* by Whittaker et al. (2013, Version 2). The values for sediment thickness are averaged over 5-minute grid cells, and located in the centre of the cells. Horizontal resolution is between ~1-10 km (0.01-0.09 degree), vertical resolution is in the order of ~1-10 m. Because it is also used in Slab1.0, one expects to increase the robustness of the analysis by using the same model.

As the model only contains thickness data at sea, this means that the data is unevenly sampled over latitude and longitude. The arcGIS file was loaded and plotted for this region, see Figure 5.1.

5.1.3. Crust model

Within the ESA 3D-Earth project, a Moho depth and V_p model was available (Szwillus, 2018). The Moho is the base of the crust. The advantage of this model was that the uncertainties for the Moho depth and V_p were quantified, which is not the case for the alternative CRUST1.0.

The P-wave velocities were converted to densities using the Nafa-Drake relation. This relation is usable for all rocks except mafic crustal and calcium-rich rocks (Ludwig et al., 1970; Brocher, 2005):

$$\rho = 1.6612V_p - 0.4721{V_p}^2 + 0.0671{V_p}^3 - 0.0043{V_p}^4 + 0.000106{V_p}^5 \tag{5.1}$$

This equation relates P-wave velocity (V_p, km/s) to density (ρ, g/cm^3), and is valid for 1.5 km/s $< V_p <$ 8.5 km/s. For the empirical values of the Nafa-Drake relation, please read (Brocher, 2005, Tab. 1). The resulting densities and Moho depths are given in Figure 5.3. The errors in the Moho depth are in the range of 2-5 km in oceanic regions, and 10 km in continental regions. The crustal densities are

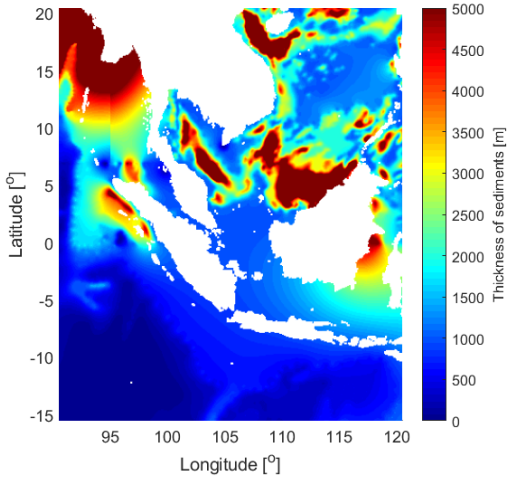

Figure 5.1: Total Sediment Thickness of the World's Oceans and Marginal Seas, Version 2 (Whittaker et al., 2013) for Sumatra

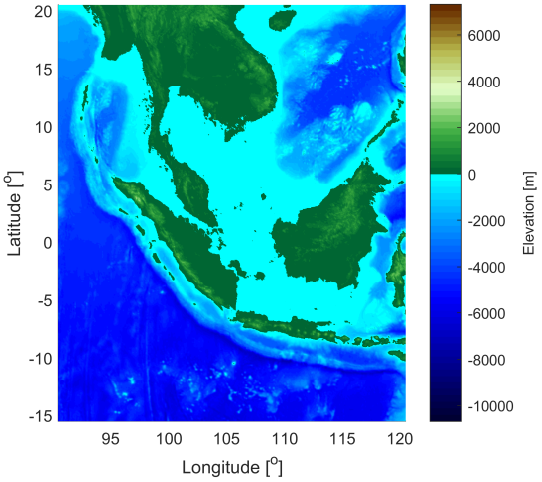

Figure 5.2: ETOPO1 for Sumatra (Amante and Eakins, 2009)

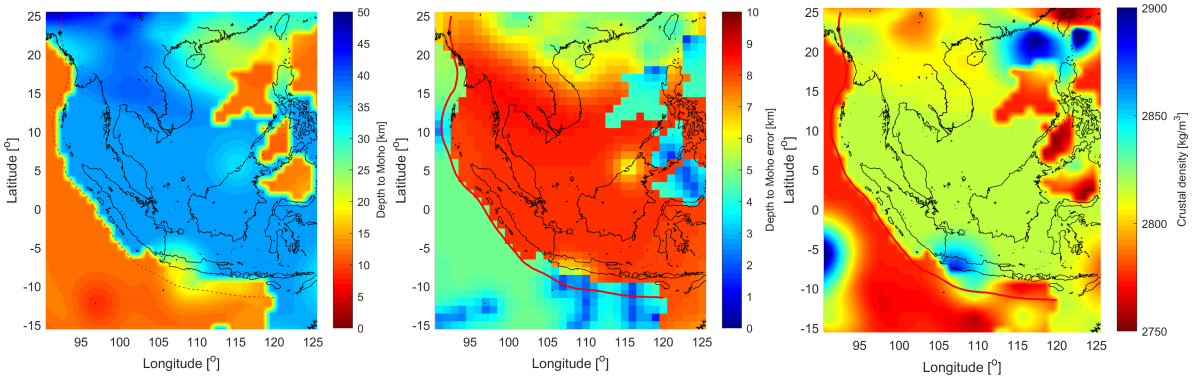

(a) Moho depth (b) Moho depth error (c) Crust density, derived from V_p

Figure 5.3: Moho and V_p-density model (Szwillus, 2018)

approximately constant (2815 kg/m^3) in the subduction zone. There is a high density (2875 kg/m^3) region in west Java. This coincides with the location where the Moho depth also has relative large values of 18-25 km, and a Moho error of ~5-8 km. Therefore, this positive mass anomaly is expected to also cause a strong positive gravity anomaly. For oceanic crust, both the thickness and densities are much lower than for continental crust.

5.1.4. Lithosphere model

The model by Hamza and Vieira (2012) is used for the Lithosphere-Asthenosphere Boundary (LAB). Heat flow and crust models were used to construct this LAB model. A new method, replacing the HS model, is used to compute the lower boundary of the lithosphere in oceanic regions. The LAB depth is given in Figure 5.4. This model has a low resolution of 2°, which is much lower than the resolution of the other models. In the subduction zone the LAB depth ranges between 120 and 160 km. In the northern part of the subduction zone, depths of more than 200 km are measured.

5.2. Integrating bathymetry and sediments

The topography and bathymetry model ETOPO1 was integrated with the oceanic sediment thickness model by Whittaker et al. (2013). The following steps were taken:

1. The ETOPO1 grid, with an original resolution of 1-arc-minute, was under-sampled to a resolution of 5-arc-minutes. The ETOPO1 grid used cell-registration. Cell-registered grids are commonly

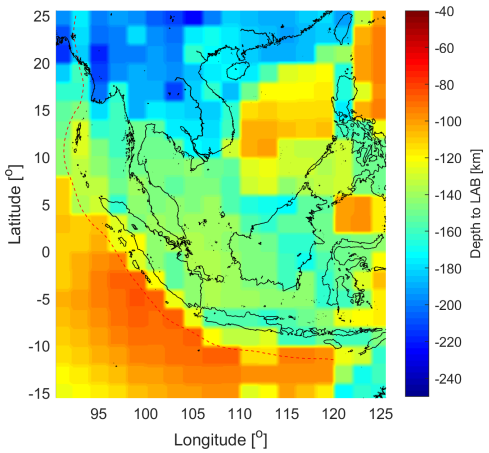

Figure 5.4: Depth to LAB (Hamza and Vieira, 2012)

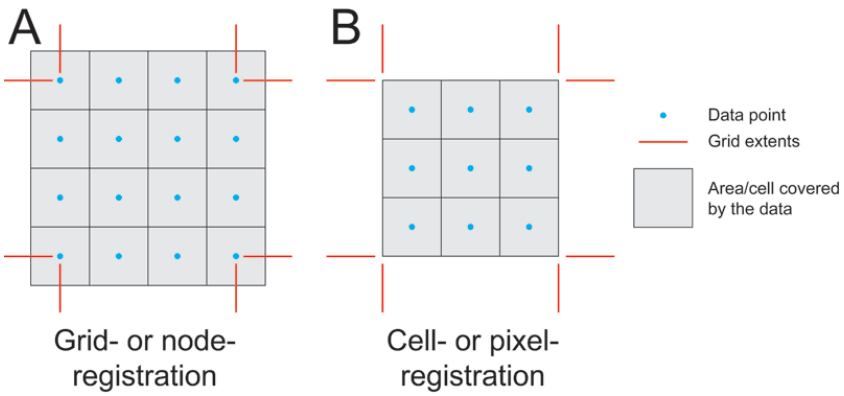

Figure 5.5: Definition of grid-registration and cell-registration for structured grids (Amante and Eakins, 2009, Fig. 14)

used to visualize data, see the definition in Figure 5.5 (Amante and Eakins, 2009).

2. The oceanic sediment model was interpolated using linear interpolation (*griddedInterplolant*) in MATLAB® to the same grid as ETOPO1. Different interpolation methods were tested in MATLAB® (*linear, nearest, next, previous, pchip, cubic, spline, makima*). The method *linear* was able to reconstruct the original dataset with the lowest misfit, especially because it outperformed other interpolation methods around NaNs cells, where other interpolation methods replaced existing cells with NaNs. Continental cells in the sediment model were assigned with NaNs.

3. The ETOPO1 data was split into a topography dataset ($Z > 0$) and a bathymetry dataset ($Z < 0$). Then the sediment thicknesses were subtracted from the bathymetry dataset, giving the base of the sedimentary layer, basically subtracting Figure 5.1 from Figure 5.2.

4. Important assumption: there are no sediments at the location of landmasses, only at sea, as can be seen in Figure 5.1, where topography is marked with NaNs (in white).

It is crucial for all the models to be referenced to the same cell-registered grid. Therefore, the interpolation explained in step 2. (above) is carried for every single external model that is loaded into MATLAB®.

5.3. Full background model

All the presented models were integrated into one background model. Because all the models are independent, inconsistencies or overlap between models might occur in certain regions. Several checks were used to give precedence to a certain model with higher certainty. If the slab model or Moho model are above the sediments model, the sediment model gets priority. The base of the lithosphere

Table 5.1: Densities used for different Earth layers

Layer	Density [kg/m^3]
Topography	2670
Bathymetry	920
Sediments	200
Crust	Variable
Lithosphere	3300
Slab	3300
Mantle	3250

follows the bottom of the slab. Cross-sections of the full background model are given in Figure 5.6. Both a constant lithosphere and the LAB model are shown. The crust model correctly changes from thin oceanic crust to thicker continental crust at the trench. Moreover, the top-slab connects well with the basement, which is the base of the sediment layer. In Figure 5.6a, the volcanic arc is seen in the topography between $\lambda = 98° - 99°$ and the back arc between $\lambda = 100° - 101°$.

When applying the densities given in Table 5.1, the gravity signal can be computed. The results are given in Figure 5.7, where gravity signal for the full model with and without slab is shown, both with LAB model. One thing that immediately stands out is the difference in range, the full model has an approximate range between -300 and 300 mGal, compared to -60 to 100 mGal for XGM2016. This large signal is because the model is not in isostatic equilibrium yet. Isostatic compensation will be investigated in Subsection 6.3.1.

There are two distinct anomalies within the subduction zone. Firstly, a large positive g_R anomaly is present at west Java, which is also seen in XGM2016, comparing Figure 5.7a with 5.8a. Moreover, a negative g_R anomaly is present in the Andaman Sea for the full model, which can be explained by the deep oceanic bathymetry at that location, see Figure 5.2. XGM2016 also has a negative anomaly in the Andaman Sea, but closer to the trench, which could also be related to the bathymetry. The full model with slab shows a large positive g_R anomaly extending from Java to Sumatra and Malaysia, which is caused by the slab, see Figure 5.7b. This anomaly does correspond with the positive g_R anomaly for XGM2016, which confirm that this anomaly is related to the subducting slab. For I_1 not much information is obtained from the results. However, there is also a I_1 anomaly present in west Java for the full model with and without slab, and also for XGM2016, see Figure 5.7c, 5.7d, and 5.8b.

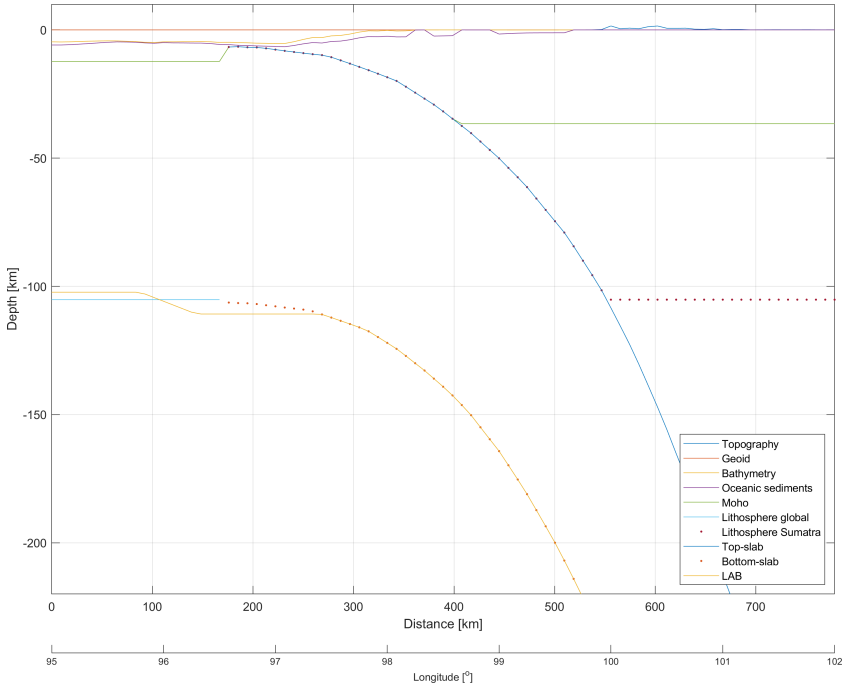

(a) Cross-section at $\phi = 0°$

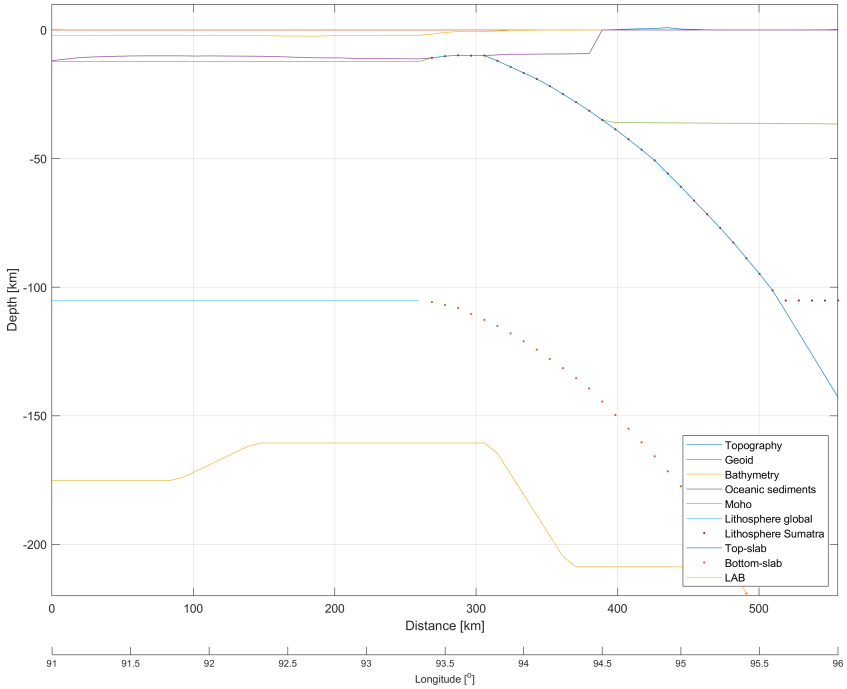

(b) Cross-section at $\phi = 18°$

Figure 5.6: W-E cross-sections of full model boundaries

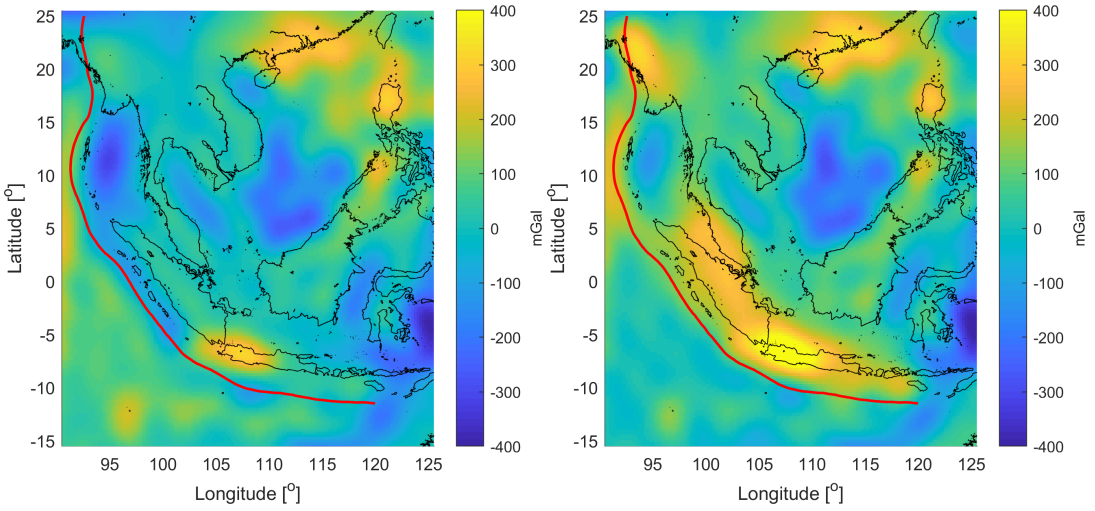

(a) Full model: g_R (b) Full model with slab: g_R

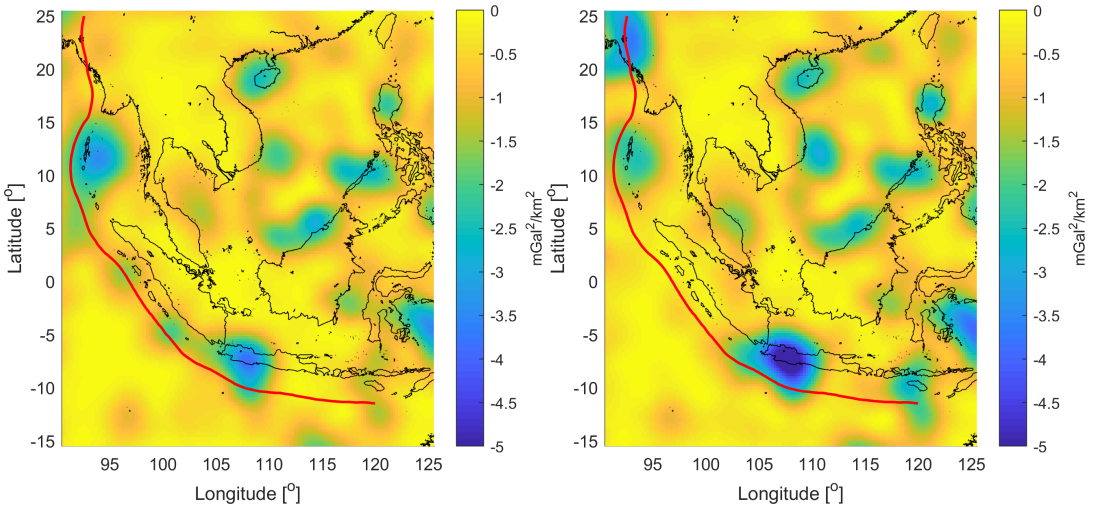

(c) Full model: I_1 (d) Full model with slab: I_1

Figure 5.7: Gravity results for full model (topography, bathymetry, sediments, crust) and slab, SHC=3-90

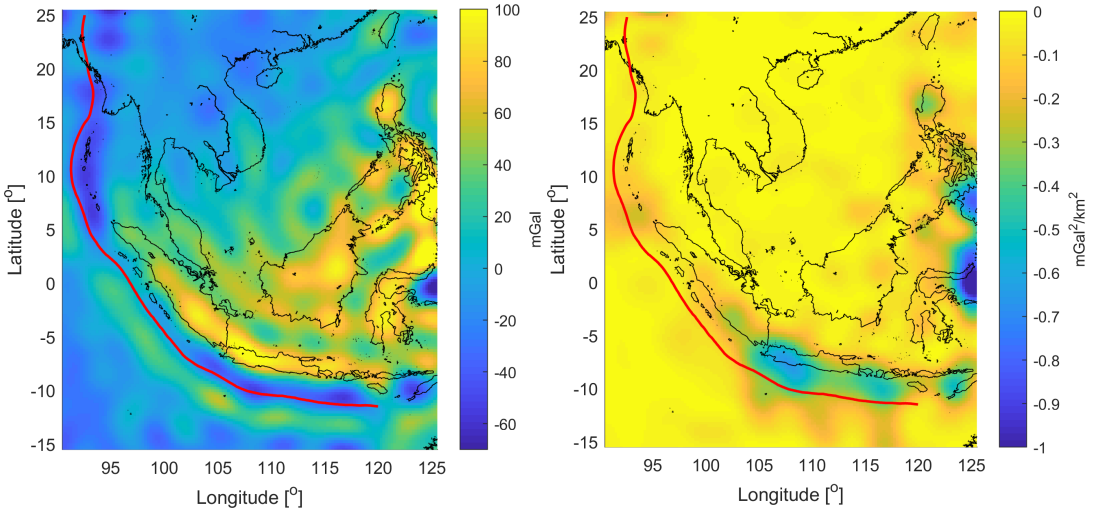

(a) XGM2016: g_R (b) XGM2016: I_1

Figure 5.8: XGM2016, SHC=3-90

6

Gravity Sensitivity Tests (GST)

In this chapter the computational results and corresponding discussions for different Gravity Sensitivity Tests (GST) applied to a simple slab are presented. This simple slab is a first-order approximation of the slab present in the Sumatra subduction zone. In short, different slab parameters are varied to see how this influences the forward modelled gravity signal. Moreover, also slab features are investigated for their gravity sensitivity. Only the radial gravity component (g_R) and the second gravity gradient tensor invariant (I_1) are discussed.

6.1. Comparison settings and metrics

Several uniform benchmark criteria are established to enable comparison between the different tests. All the presented cross-sections of the subduction zone are taken perpendicular to the trench, see Figure 6.1. The seven different cross-sections are 7.5° (~830 km) apart, and have an individual length of 12.5° (~1400 km). Depending on the region of interest, all or a selection of the cross-sections will be used to visualize results of the different tests.

Up until this point in the report, a model SHC d/o of 179 is used. However, all the input boundary models (e.g. topography, sediments, slab, LAB, etc.) for the analysis (forward modelling) are sampled at a 5-arc-second resolution, which corresponds to a d/o 2159 resolution. Therefore, one could potentially increase the SHC resolution in the analysis.

The nominal synthetic slab model is based on the top-slab geometry explained in Section 4.2 with a constant top-slab perpendicular thickness of 100 km, where the slab extends down to 600 km, the lithosphere and slab have the same density of 3300 kg/m^3, and the mantle density is 3250 kg/m^3, resulting in a slab-mantle density contrast of 50 kg/m^3. Different constant values for the slab-mantle density contrast will be tested in GST3.

6.1.1. Spectral analysis for slab based on Slab1.0

The purpose of a spectral analysis is to find the optimal SHC bandwidth capturing the signal solely related an input model. The slab model based on Slab1.0, presented in Section 4.1, was used to perform a spectral analysis. A constant thickness of 70 km was used together with a large density contrast of -400 kg/m^3.

The spectral analysis was done with respect to the radial gravity component (g_R). The assumption that the full slab signal is captured by a SHC bandwidth of d/o 0 to 179 was used. The signal for this bandwidth was used as observation data ($g_{R_{obs}}$). Quantifying the remaining signal for different SHC truncation settings was done by computing the residual with the $g_{R_{obs}}$ grid, and comparing it to the average signal of the observations ($\overline{g_{R_{obs}}}$). This was done for every grid point individually, after which a summation was applied, using the following equations:

$$\overline{g_{R_{obs}}} = \frac{1}{N} \sum_{\lambda_{min}}^{\lambda_{max}} \sum_{\phi_{min}}^{\phi_{max}} g_{R_{obs}}(\lambda, \phi) \tag{6.1}$$

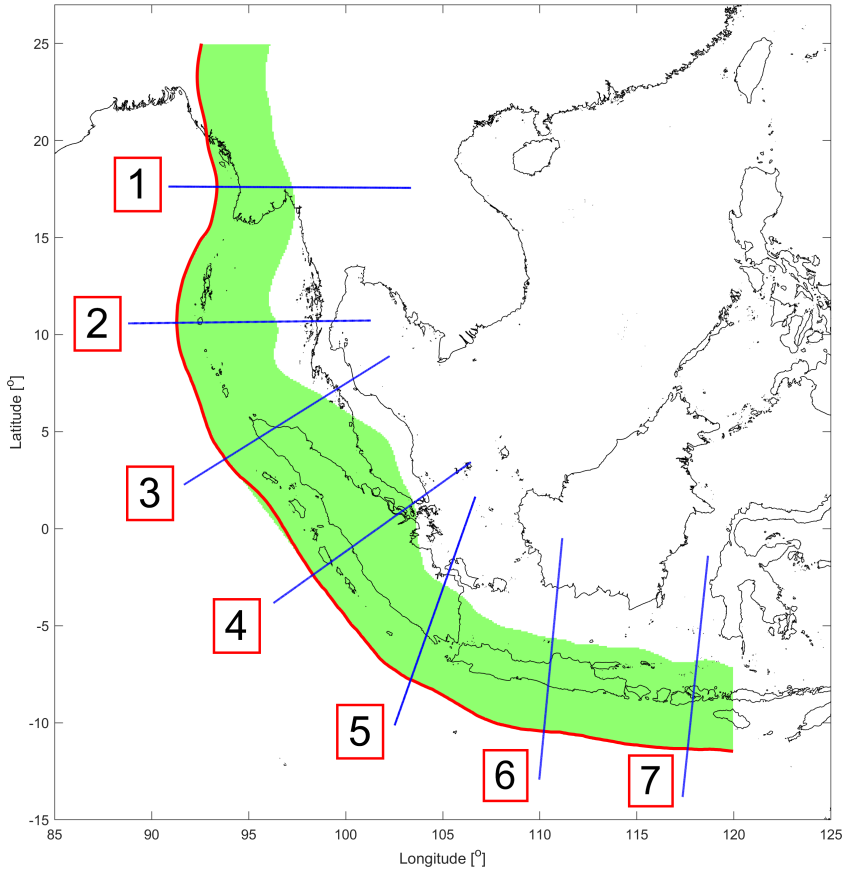

Figure 6.1: Trench-perpendicular cross-sections of the Sumatra subduction zone (green, trench given in red): equal separation along trench by 7.5° (~830 km), cross-section length of 12.5° (~1400 km)

$$\delta g_R(\lambda,\phi) = |g_R(\lambda,\phi) - g_{R_{obs}}(\lambda,\phi)| \tag{6.2}$$

$$g_{R,total} = \frac{1}{N}\sum_{\lambda_{min}}^{\lambda_{max}}\sum_{\phi_{min}}^{\phi_{max}} \delta g_R(\lambda,\phi) \tag{6.3}$$

$$\Delta g_R = 100\% - \frac{g_{R,total}}{|\overline{g_{R_{obs}}}|} * 100\% \tag{6.4}$$

Where, λ and ϕ are the longitudes and latitudes of points within the subduction zone, N is the total number of sample points, $\overline{g_{R_{obs}}}$ is the average observation signal, and Δg_R is the percentage representing the remaining signal for a certain SHC truncation setting.

Varying the SHC lower and upper limits between 0 and 175 resulted in the spectral analysis plot given in Figure 6.2. The g_R slab signal is confined between lower SHC limits of d/o 1 and 20 and upper SHC limits of d/o 40 and 175. For SH=5-60 the remaining signal is 79%, increasing the lower SHC limit by d/o 20 to SH=25-60 results in only 36% being left of the original signal. Decreasing the upper SHC limit by d/o 20 to SH=5-40, still results in 68% of the signal to be present. Therefore, increasing the lower SHC limit has a larger impact on the remaining g_R slab signal than decreasing the upper SHC limit. From the top row in Figure 6.2 for SH=0-175 99% of the signal is present, for SH=20-175 only 56% of the signal is left. Therefore, it is concluded that approximately 45% of the signal is represented by SHC between d/o 0 and 20. A higher resolution spectral analysis is given in Figure 6.3, where the dark red marks truncation settings for which 80% of the signal is present. When striving for 80% of the signal to be present, truncations settings of 0-44, 2-48, 4-56, and 6-84 are required. Those truncation settings show that to compensate for the loss of signal due to lower SHC truncation, significantly more higher order SHC are required to obtain the same amount of signal.

To find the optimal (narrowest) bandwidth comes down to a trade-off between isolating the signal using a narrow bandwidth or maximizing the amount signal captured using a large bandwidth. Having a narrow bandwidth has the advantage of omitting signal not related to the subducting slab.

6.1.2. Spectral analysis for slab based on Slab1.0, UU-P07, and RUM

A spectral analysis was carried out for the combined top-slab model based on Slab1.0, UU-P07 and RUM, which is explained in Section 4.2. A constant thickness of 100 km was used together with a slab density contrast of 50 kg/m^3. Instead of using the spectral analysis algorithm from the previous section, a more computationally efficient spectral analysis was constructed utilizing the conclusions from Subsection 6.1.1. It was shown that truncating the lower SHC limit is not favourable because of two reasons: 1) Most of the slab signal (~45%) is present between SHC d/o 0 and 20, 2) Significant additional higher order SHC are required to compensate for the loss of signal from the lower order SHC. Forward modelling using higher order SHC is much more computationally expensive than using lower order SHC. Therefore, the lower SHC limit (l_{min}) was fixed to d/o 3. In the spectral analysis, the upper limit (l_{max}) was varied between d/o 3 and 359.

For l_{max} = 359, one used virtual layers of 25 km thick, for all the other computations using different l_{max} virtual thicknesses of were used. This decision was made because larger virtual thicknesses increase the computational efficiency. For the explanation of why virtual layers are required to obtain convergence of the forward modelling tool, see Subsection 2.4.2. The visual results are given in Figure 6.5 and Figure 6.6, where one deliberately fixed the colour-scale axis. The numerical results are presented in Figure 6.4.

Assuming that the extreme values for g_R and I_1 are good indicators of the available signal, accurate truncation settings based on Figure 6.4 were selected. For g_R 90% of the slab signal is present for SHC between d/o 3 and 50, and the slab is fully captured (99%) for SHC above d/o 90. As expected, I_1 is more sensitive for truncations, 80% of the signal is captured for SHC up to d/o 90, extending SHC up to d/o 180 will lead to 99% coverage.

The observations above are confirmed by visual inspection of the gravity results. Figure 6.5 shows that the g_R signal of SHC=1-60 is similar in amplitude and distribution as the signal for SHC=3-359.

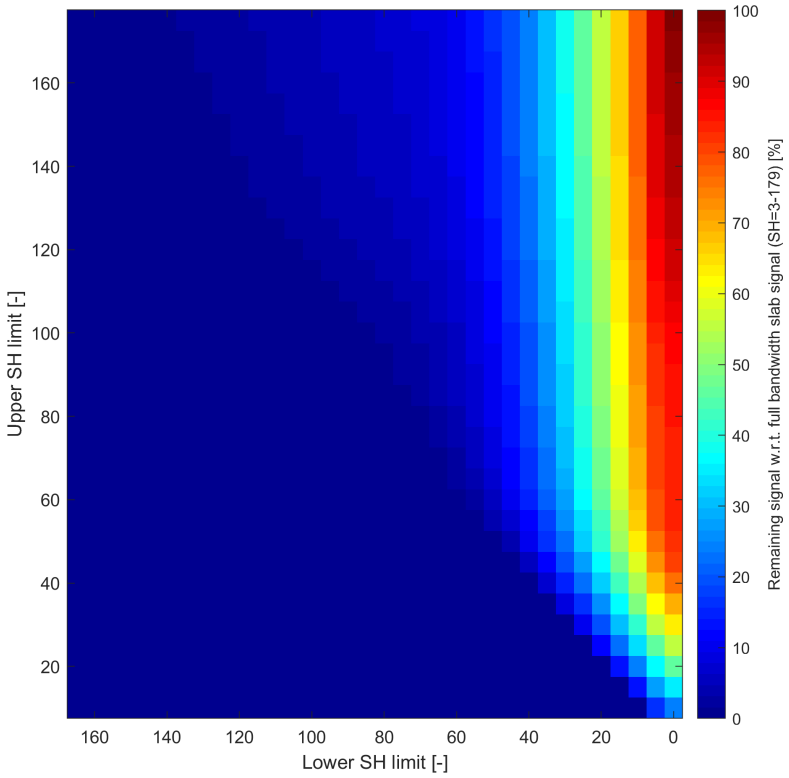

Figure 6.2: Spectral analysis for $l_{min} = 0 \rightarrow 165$ and $l_{max} = 10 \rightarrow 175$ (step-size = 5)

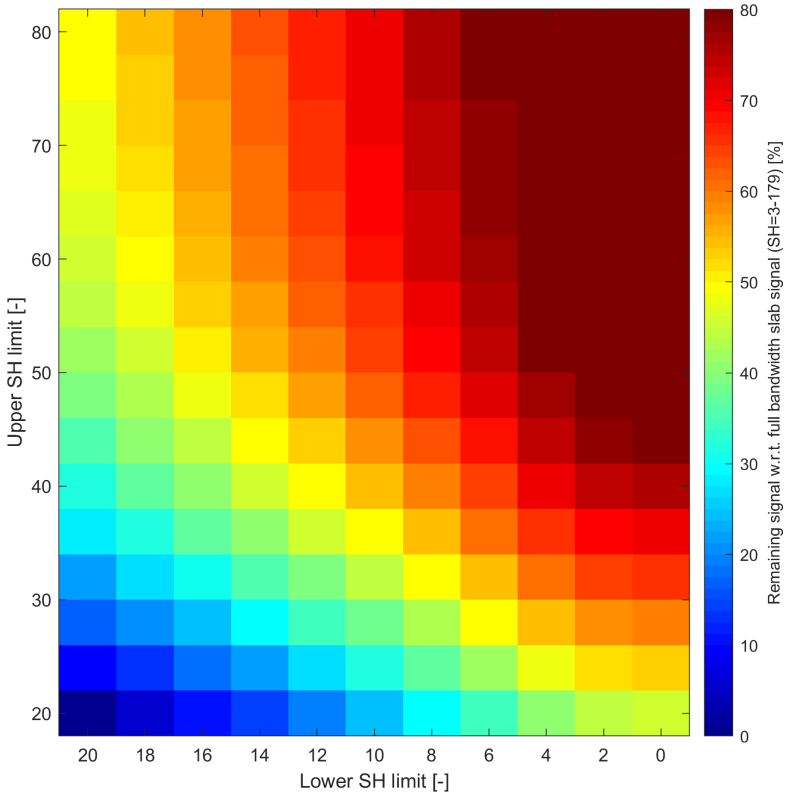

Figure 6.3: Spectral analysis for $l_{min} = 0 \rightarrow 20$ and $l_{max} = 20 \rightarrow 80$ (step-size = 2)

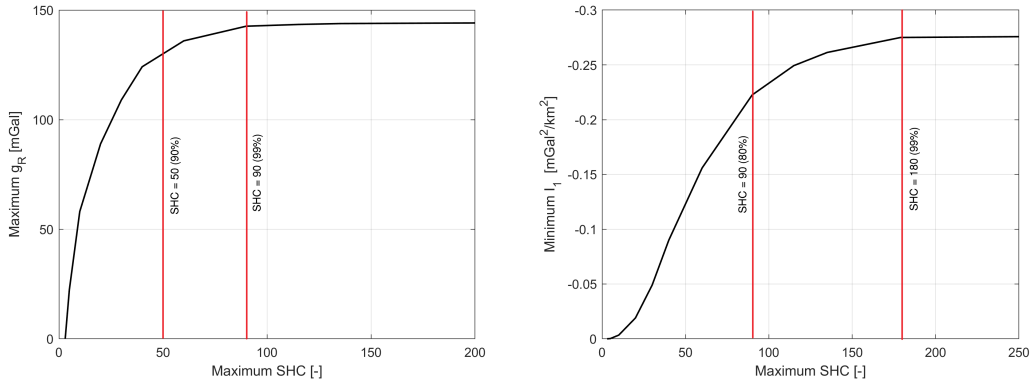

(a) SHC truncation effect on maximum g_R

(b) SHC truncation effect on minimum I_1

Figure 6.4: Results for model analysis (forward modelling) using different maximum SHC

However, SHC=3-30 shows significant change with respect to SHC=3-60. This is in accordance to the steep decline of the signal after SHC=40, seen in Figure 6.4a. Figure 6.6 shows that the I_1 signals for SHC=3-135 and SHC=3-359 show close resemblance. For SHC=3-60 and SHC=3-90 the signal diminishes in amplitude as the short-wavelength signal is being truncated. Between SHC=3-135 and SHC=3-90 the I_1 signal decreases slightly by 20%, but the steep decrease is indeed seen for lower SHC than d/o 90, in accordance with Figure 6.4b. Therefore, the regional maximum g_R or minimum I_1 are accurate benchmarks for spectral analysis.

A truncation of $l_{max} = 90$ will be used, allowing for a theoretical maximum resolution of 2°, which corresponds to 220 km at the equator. This truncation setting was selected after a trade off between computational efficiency and forward modelling accuracy. Having 99% and 80% of the total signal for g_R and I_1, respectively, was deemed sufficient for the Gravity Sensitivity Tests (GST).

6.2. GST related to slab parameters

The following six gravity sensitivity tests (GST) will investigate the effects of different slab parameters on the gravity signal. When adjusting slab parameters to fit existing gravity observations, knowledge on the sensitivities will allow for more informed adjustments of the slab parameter. Firstly, the gravity signal of slab segments at different depths is analysed in GST0. Thereafter, the gravity sensitivity to slab maximum depth, slab thickness, and slab uniform density are investigated in GST1 to GST3. Different radial density distributions for the slab will be researched in GST4. For a schematic summary of the slab parameters being investigated in GST0 to GST4, see Figure 6.7. For GST5 and GST6 non-constant slab thickness distributions spanning the Sumatra subduction zone are investigated. If not stated otherwise, the nominal slab setting given in Section 6.1 are used, where the slab has a thickness of 100 km and extends down to 600 km, with a slab-mantle contrast of 50 kg/m^3, and no slab-lithosphere contrast. For all the different GST a virtual thickness of 50 km is used. Important to note that this virtual thickness is does not have physical implications on the results, but is an important programming parameter to obtain correct forward modelled gravity results, see Subsection 2.4.2.

GST0: Slab segments of 100 km at different depths

GST1: Variable maximum depth of slab

GST2: Variable constant thickness of entire slab

GST3: Variable constant density of entire slab

GST4: Variable density with depth within slab

GST5: Age-based along-trench thickness distribution for entire slab

GST6: Age-based thickness distribution varying in dip-direction based on subduction rate/direction

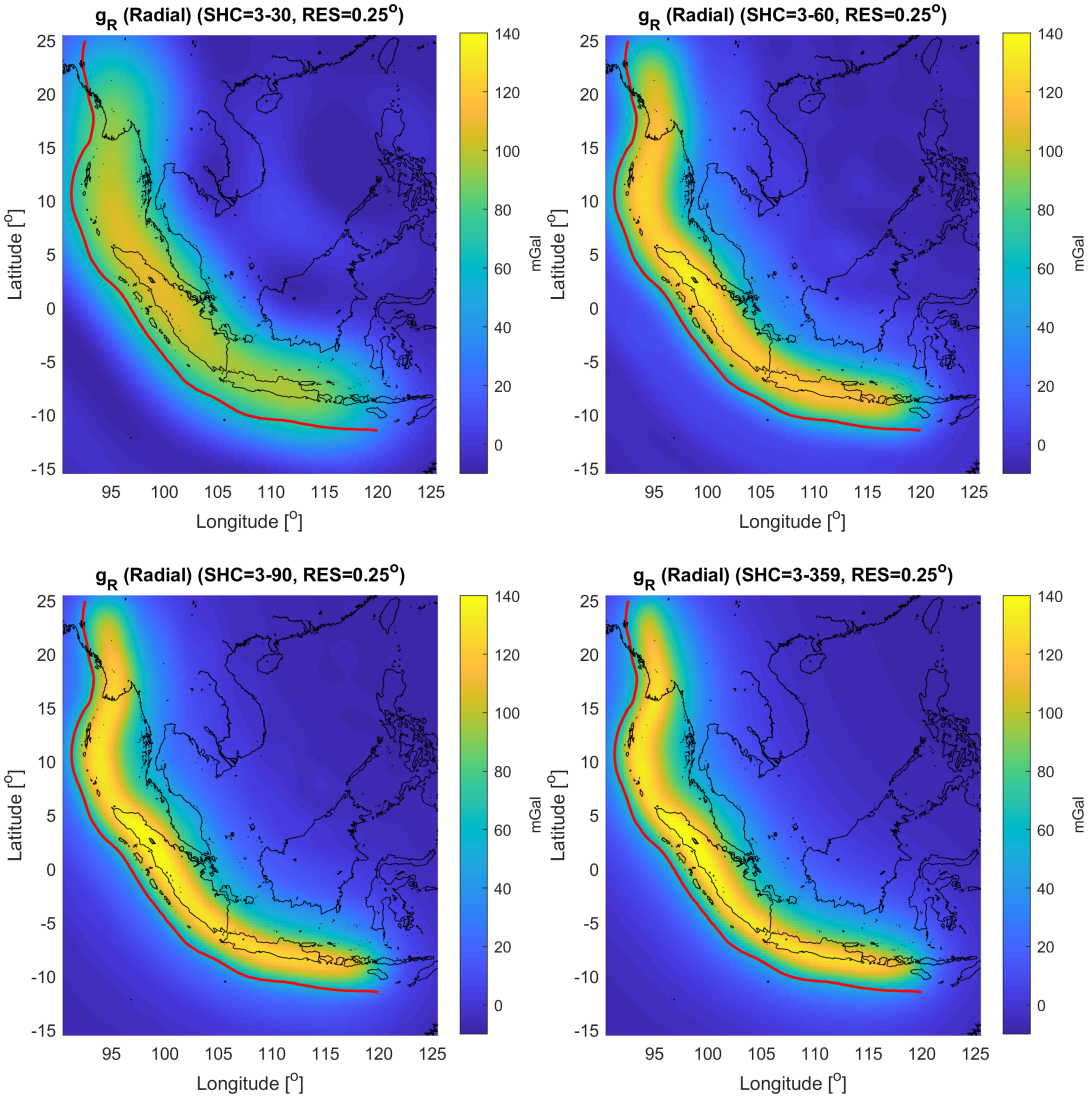

Figure 6.5: Plots for model g_R analysis (forward modelling) using different maximum SHC [nominal model]

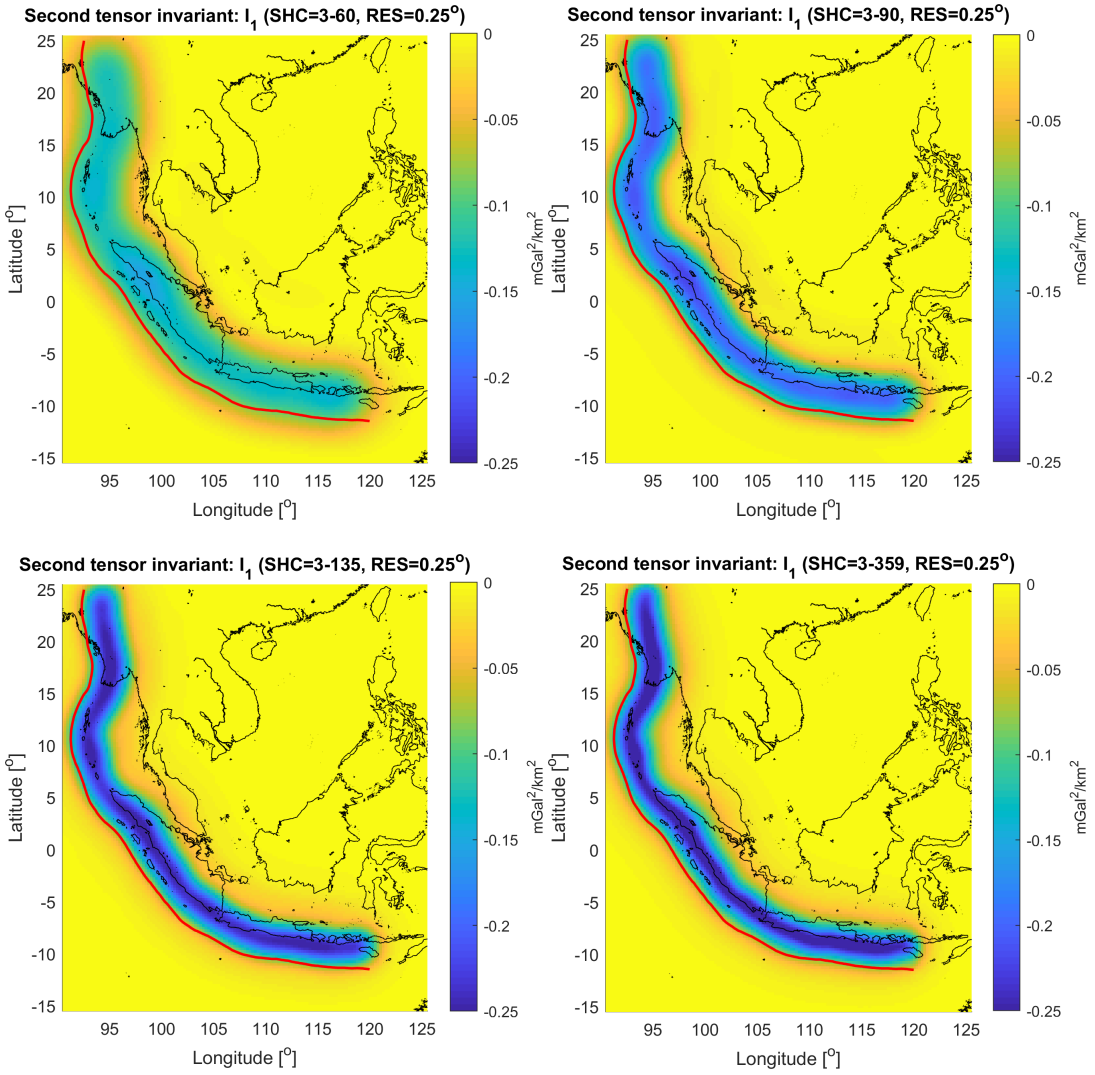

Figure 6.6: Plots for model I_1 analysis (forward modelling) using different maximum SHC [nominal model]

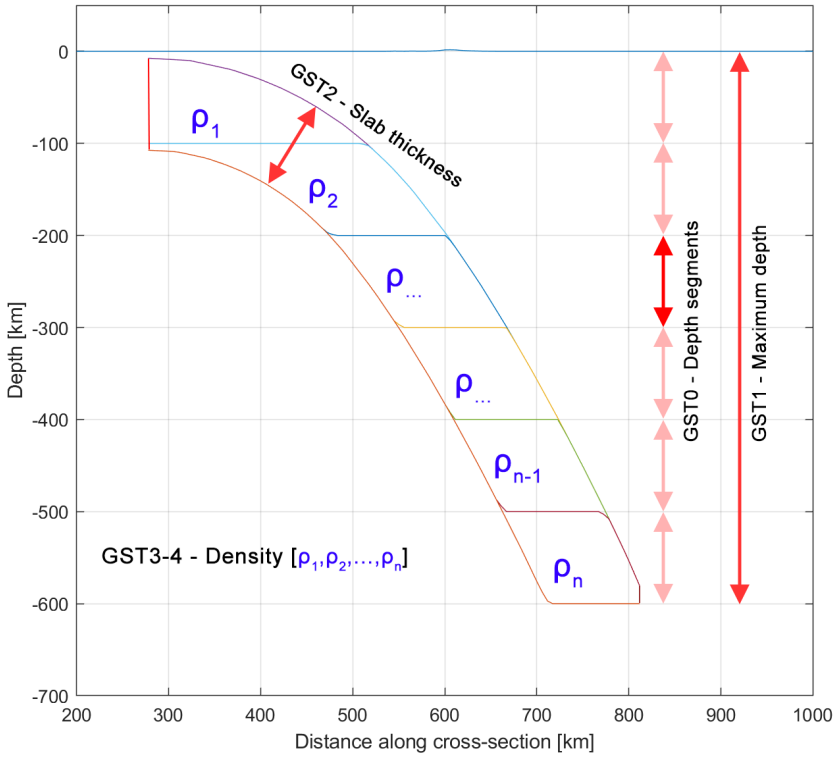

Figure 6.7: Schematic of slab parameters being investigated in GST0 to GST4: maximum slab depth, slab thickness, and slab density distribution (ρ_1,ρ_2,...,ρ_n)

6.2.1. GST0: Slab segments of 100 km at different depths

To better understand the gravity signal coming from different vertical segments of the slab the following sensitivity test is constructed. This test will determine to what depth an accurate slab model is necessary for gravity modelling. Those conclusions will be linked to the noise level of the observations, see Subsection 2.3.2.

The slab was segmented using a constant vertical thickness of 100 km. A slab-mantle density contrast of 50 kg/m^3 was used. Four cross-sections of the input model are given in Figure 6.8. The gravity forward modelling was done at sea-level (h=10 m), and forward modelled results at GOCE altitude are also presented.

Figure 6.9 supports three main conclusions. Firstly, for both g_R and I_1 the signal gets smeared for deeper segments. Shallow segments are more pronounced in the short-wavelengths, whereas for deeper segments the long-wavelengths become more dominant. This can be seen in Figure 6.9. Secondly, for increasing segment depths the signal moves away from the trench. This is due to the addition of mass at the bottom of the slab, which is also located furthest from the trench. Thirdly, the maximum amplitude of I_1 is positioned around northern Sumatra, where the slab dips less steep and therefore the slab segments are wider, increasing the mass relative to the other segments north and south from this section.

Using the extreme values for g_R and I_1 within the subduction zone as benchmark, the sensitivity with respect to segment depth was captured in Figure 6.10. For both g_R and I_1 the extreme values decrease with increasing segment depth. With every 100 km increase in depth, the segment's maximum g_R amplitude gets reduced by 25-50%. Moreover, every 100 km increase in depth leads to a 60-90% reduction in the segment's minimum I_1 amplitude. Therefore, masses below 300-400 km depth do not significantly influence I_1, whereas g_R does show sensitivity for deeper masses down to at least 600 km depth. Those observations link back to Subsection 2.1.1, where it was shows that the GGT components have higher sensitivity to masses close to the reference point than the gravity components, and lose sensitivity quickly with increasing distance. I_1 being a product of the GGT components will have similar sensitivity characteristics, which is proven by the previous results. Table 6.1 shows that

Table 6.1: Extreme values for different segment depths (GST0)

Model	Max. g_R [mGal]	Percentage (%)	Min. I_1 [mE]	Percentage (%)
0-100 km	119.66	42.82	-509.71	79.50
100-200 km	69.52	24.88	-103.72	16.18
200-300 km	36.79	13.17	-19.75	3.08
300-400 km	25.36	9.08	-5.71	0.89
400-500 km	18.81	6.73	-2.06	0.32
500-600 km	9.30	3.33	-0.20	0.03
800-900 km	8.91	x	-0.16	x
1000-1100 km	6.90	x	-0.07	x

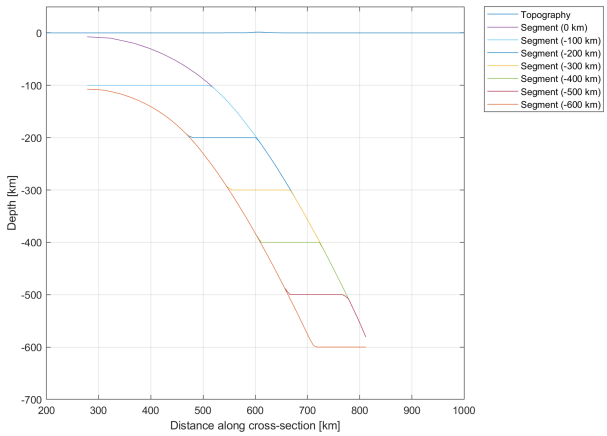

Figure 6.8: Trench-perpendicular cross-section N=6 (see Figure 6.1) for segmented slab with constant 100 km vertical thickness

the slab between 0 and 300 km contains 80% of the g_R signal, and 98% of the I_1 signal.

The behaviour of the extreme values of g_R and I_1 continued for lower depths than 600 km. Because the used slab geometry only extends down to 600 km, one replicated the slab segment between 500-600 km, and moved it to lower depths (800-900 km, 1000-1100 km). For those two test-cases, the values did not follow on the expected trend-line. For both g_R and I_1 the extreme values do not decrease in the same trend below 600 km. From Table 6.1, the g_R maximum value for 500 km is 18.1 mGal, for 600 and 800 it is 9.3 and 8.9 mGal. Thus, g_R does not significantly decrease for lower depths of 600 km. The same observation is true for I_1. The lower signal for deeper segments in not only a result of the increase distance to the computation point, but also due to the different segment geometries, and therefore, different segment masses. Seeing little change when moving a constant segment from 600 km, down to 800 and 1000 km, leads to the conclusion that the slab geometry itself also significantly influences the gravity signal for different depths.

In Figure 6.11, gravity results (d/o 200) for different density contrasts and corresponding depths are presented. This figure shows that for density contrasts lower than 3 kg/m^2 segments deeper than 200 km will fall in the noise level of GOCE measurements, and can therefore be neglected. Furthermore, one sees that the signal for segments deeper than 200 km is small compared to the upper segments, a 50-75% reduction compared to the first segment is measured.

Furthermore, the segments are forward modelled at the nominal GOCE altitude of 225 km. The results are presented in Figure 6.12. Those figures, which use constant colour-scales, show again that the signal quickly diminishes with increasing depth. Comparing g_R in Figure 6.9a with Figure 6.12a, one sees that the GOCE signal is less concentrated on the trench, in other words, more smeared out. Comparing I_1 in Figure 6.9b with Figure 6.12b, one observed that regional extreme values, e.g. west of Palau Sumba (red circle in Figure 6.9b), disappear at GOCE altitude. Concluding, the g_R and I_1 signal lacks short-wavelength information of the slab at the nominal GOCE altitude comparing to the signal at sea-level.

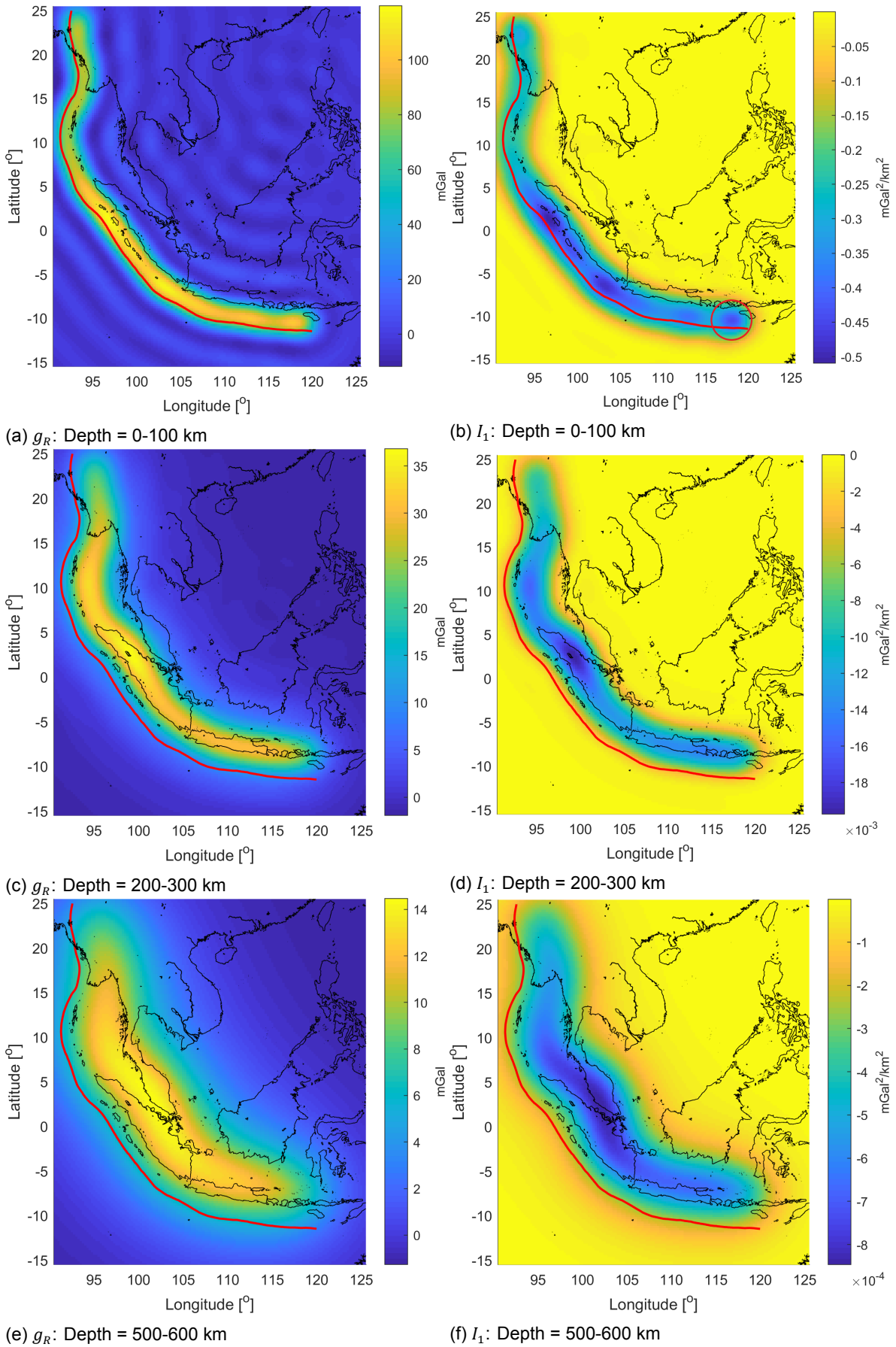

(a) g_R: Depth = 0-100 km

(b) I_1: Depth = 0-100 km

(c) g_R: Depth = 200-300 km

(d) I_1: Depth = 200-300 km

(e) g_R: Depth = 500-600 km

(f) I_1: Depth = 500-600 km

Figure 6.9: g_R and I_1 for segments at different depths for SHC = 3-90 using different colour-scales (GST0)

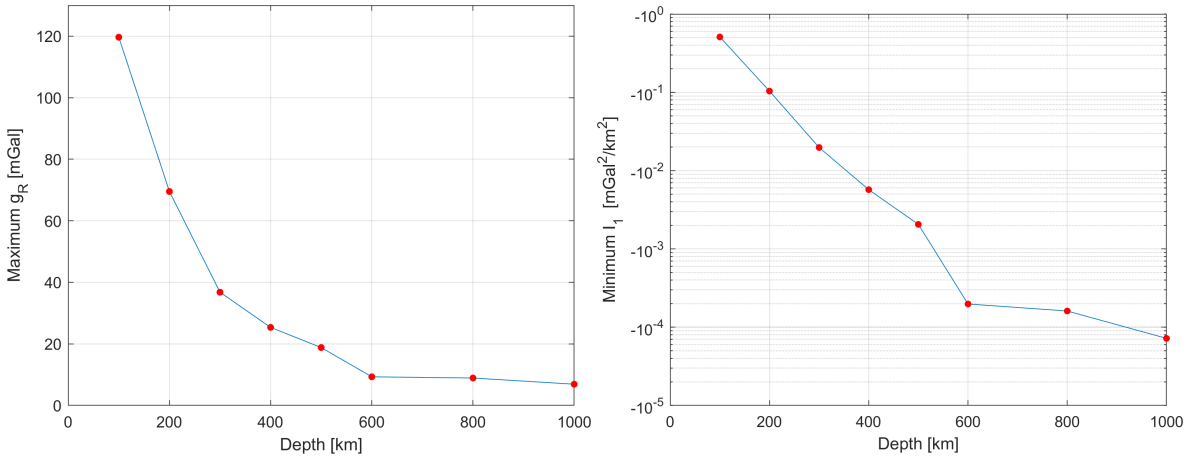

(a) Extreme values g_R (b) Extreme values I_1 (log-scale)

Figure 6.10: Extreme values for different segment depths (GST0)

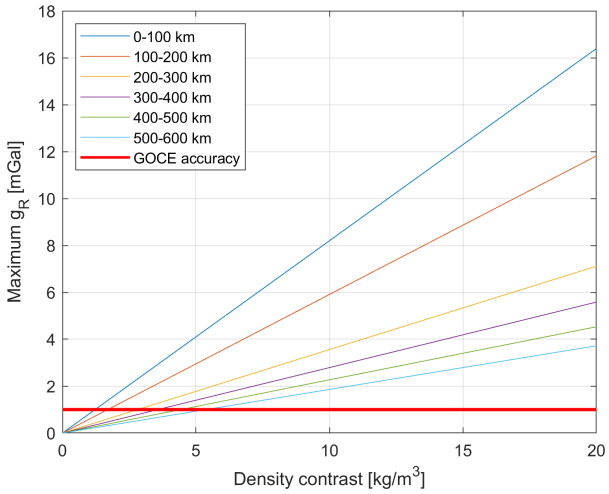

Figure 6.11: Maximum gravity signal at GOCE altitude for varying density contrasts for different slab segments (SHC=3-200)

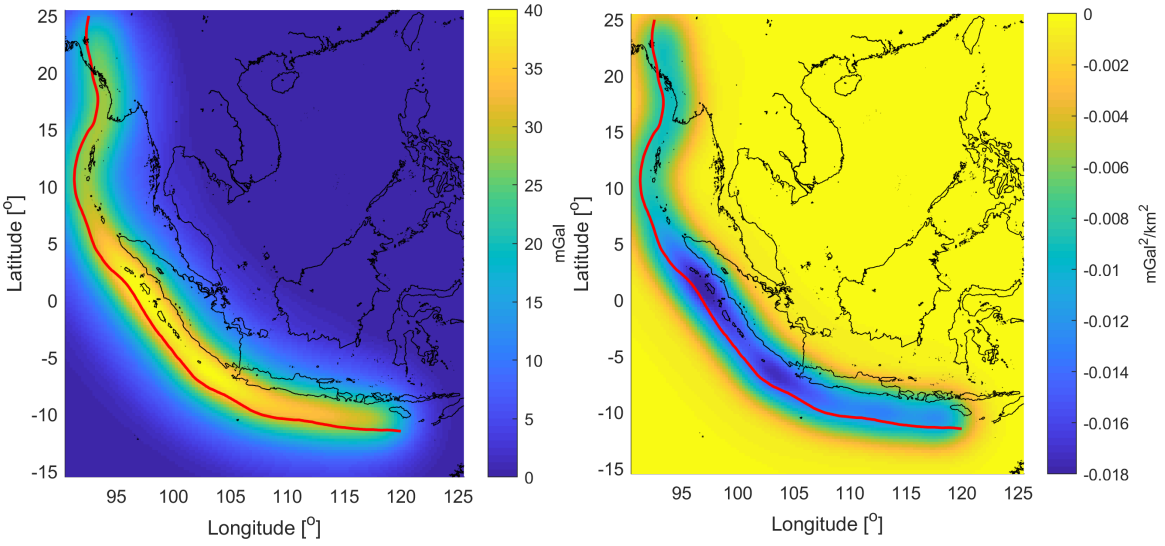

(a) Depth = 0-100 km

(b) Depth = 0-100 km

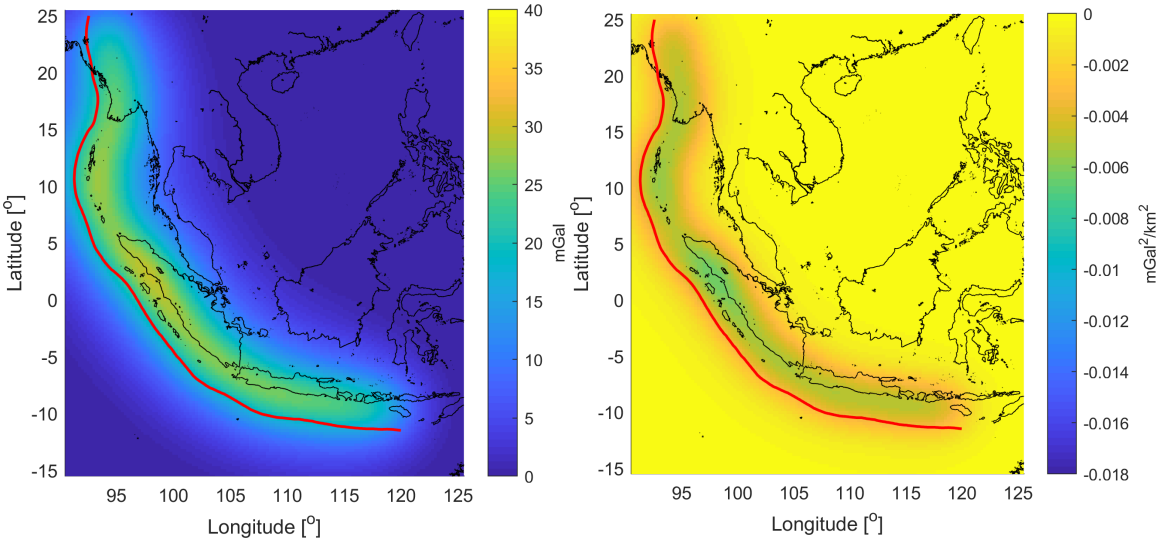

(c) Depth = 100-200 km

(d) Depth = 100-200 km

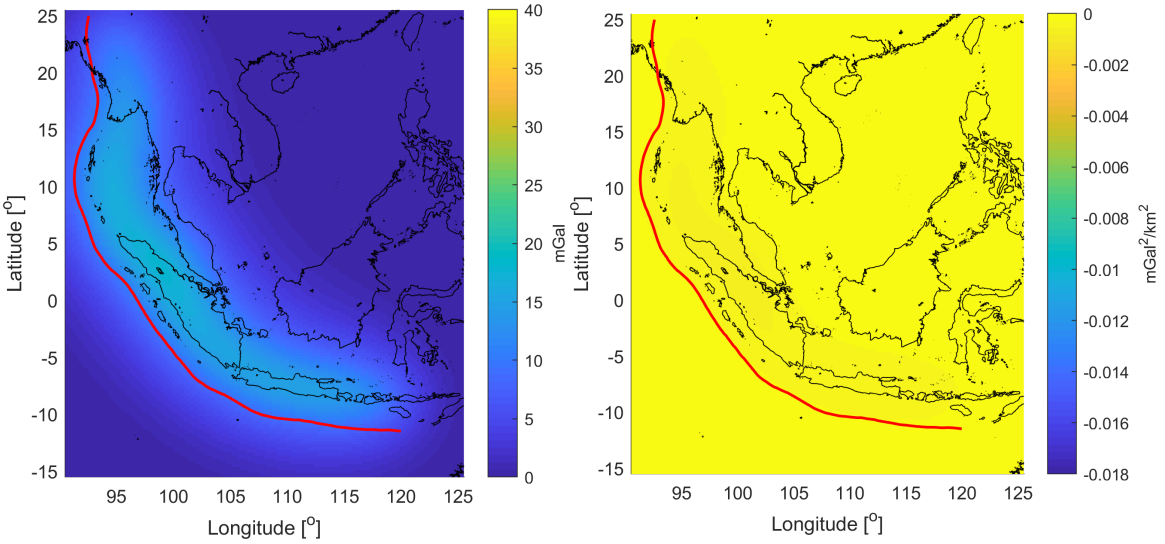

(e) Depth = 200-300 km

(f) Depth = 300-400 km

Figure 6.12: g_R and I_1 for segments at different depths for SHC = 3-90 at GOCE altitude (GST0)

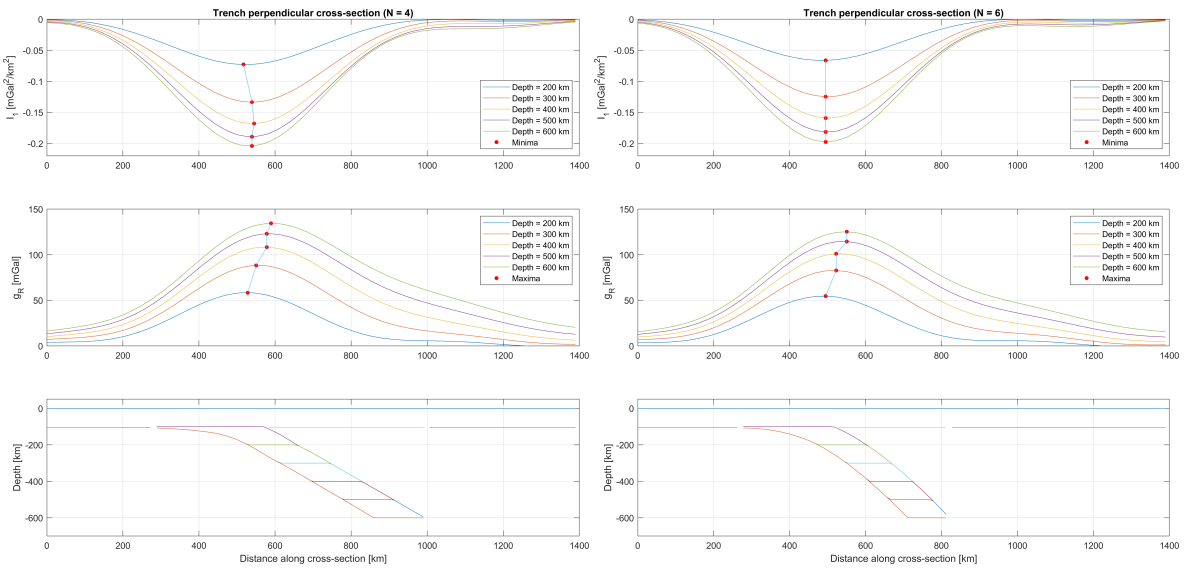

Figure 6.13: Gravity (g_R, I_1) cross-sectional results (GST1)

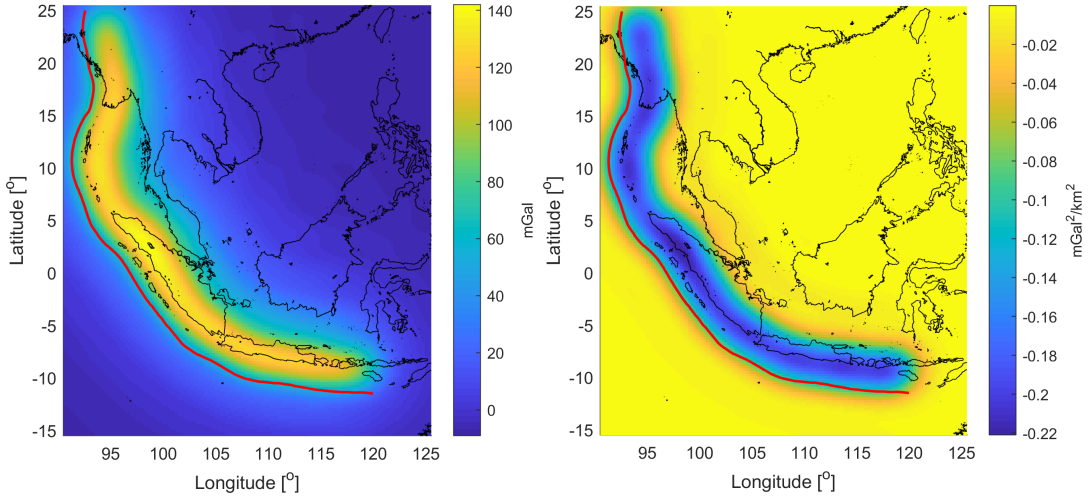

(a) Radial gravity g_R (b) Second invariant I_1

Figure 6.14: Gravity results for slab max. depth = 600 km (GST1) at sea-level, SHC=3-90 [nominal model]

6.2.2. GST1: Variable maximum depth of top-slab

This test investigates the change in gravity by varying the maximum depth of the slab, from 200 km to 600 km with a step-size of 100 km, see Figure 6.7. This test will add to the conclusions obtained from GST0, as it considers the slab as a whole, instead of only its individual segments, and therefore gives the total gravity signal. A constant slab thickness of 100 km was used. The lithosphere was modelled to be perfectly connected to the bottom-slab surface at the trench. The same density of 3300 kg/m^3 was applied for the lithosphere and the slab, resulting in no density contrast for the first 100 km depth, which is seen in the slab cross-section in Figure 6.13. A density contrast of 50 kg/m^3 between the slab and mantle was applied, giving the mantle a density of 3250 kg/m^3.

Three conclusion can be made upon inspection of Figure 6.13. Cross-sections N=4 and N=6 were chosen because of their good representation for the upper and lower bounds of the signal for the seven cross-sections. Firstly, comparing 'Depth = 200 km' to 'Depth = 300 km' and 'Depth = 400 km', the g_R anomaly is moving away from the trench as the subducting slab is allowed to extend deeper, which means mass is added at the bottom of the slab. This shift for N=4 is approximately 25 km and 30 km, respectively. For the models deeper than 500 km, no significant shift of the g_R peak is observed. A much smaller shift is observed for I_1, where the shift between 'Depth = 200 km' to 'Depth = 600 km'

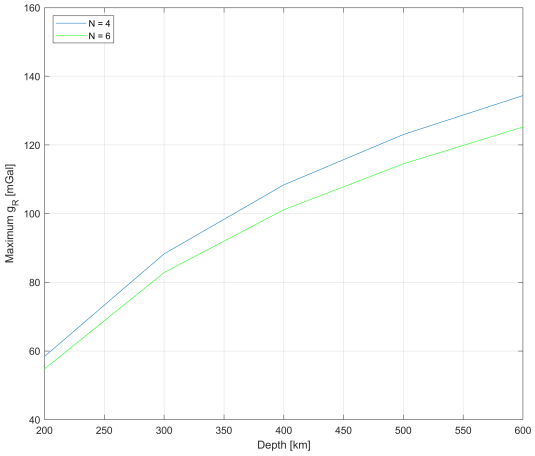

(a) Extreme values g_R (GST1)

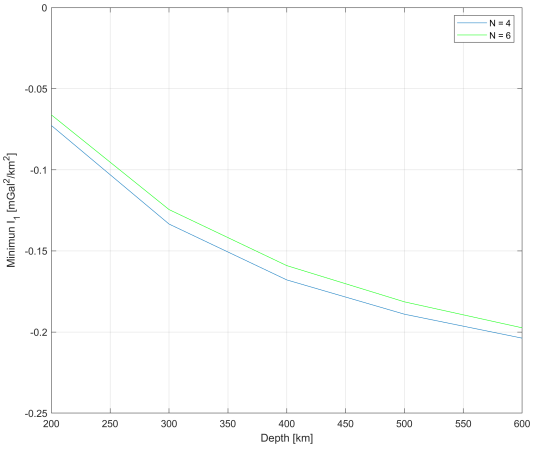

(b) Extreme values I_1 (GST1)

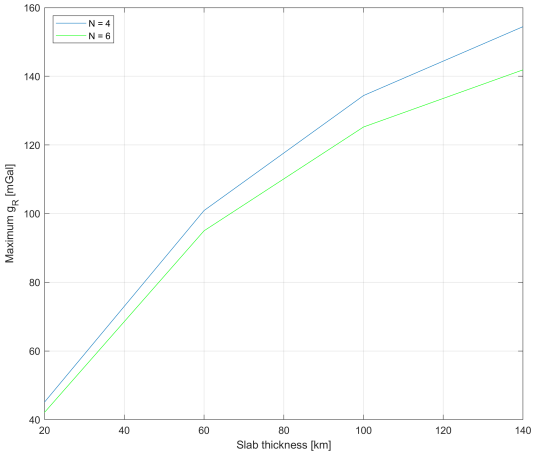

(c) Extreme values g_R (GST2)

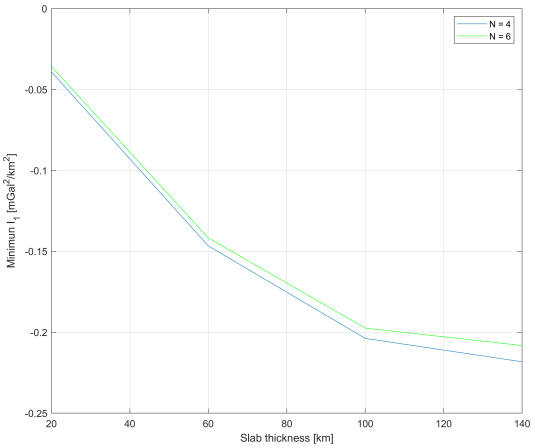

(d) Extreme values I_1 (GST2)

Figure 6.15: Extreme values for cross-sections N=4 and N=6 (GST1, GST2)

for N=4 is less than 20 km, and for N=6 no shift occurs at all. A shift towards the trench is observed in N=4, between 'Depth = 400 km' and 'Depth = 500 km'. Thus, for this slab geometry, I_1 does not necessarily move towards the location where mass it added, whereas g_R does. Secondly, for both g_R and I_1 the signal's amplitude increases for increasing slab depths. However, this increment added to the signal diminishes with depth, see Figure 6.15a and Figure 6.15b, where the gradient declines with depth. Except for increasing amplitude, no significant changes of the signal characteristics are observed. Lastly, the g_R and I_1 anomaly is positioned approximately in the middle of the subduction zone model and spans the entire zone, with slightly higher values in northern Sumatra, see Figure 6.14, where the slab dips less steep.

Having an observation error of ~1 mGal requires the slab depth modelling accuracy to be between 3.5 and 9 km, for a respective depth of 200 to 600 km. Those values are computed using the N=4 gradient in Figure 6.15a. This N=4 cross-section represent the upper boundary for required accuracy assuming a slab-mantle density contrast of 50 kg/m^3.

6.2.3. GST2: Variable constant thickness of entire slab

The constant slab-perpendicular thickness was varied from 20 km to 140 km in order to estimate the required accuracy for the slab thickness for accurate gravity modelling, see GST2 in Figure 6.7. The maximum slab depth was kept to 600 km. The global lithosphere adjusts automatically to the slab thickness at the trench, thus if the slab thickness is 60 km, the lithosphere will also be 60 km thick. This is done to keep the slab directly connected to the oceanic lithosphere (Fowler, 2005; Lowrie, 2007).

For increasing thickness, Figure 6.16 shows that, the g_R and I_1 signal both move away from the trench.

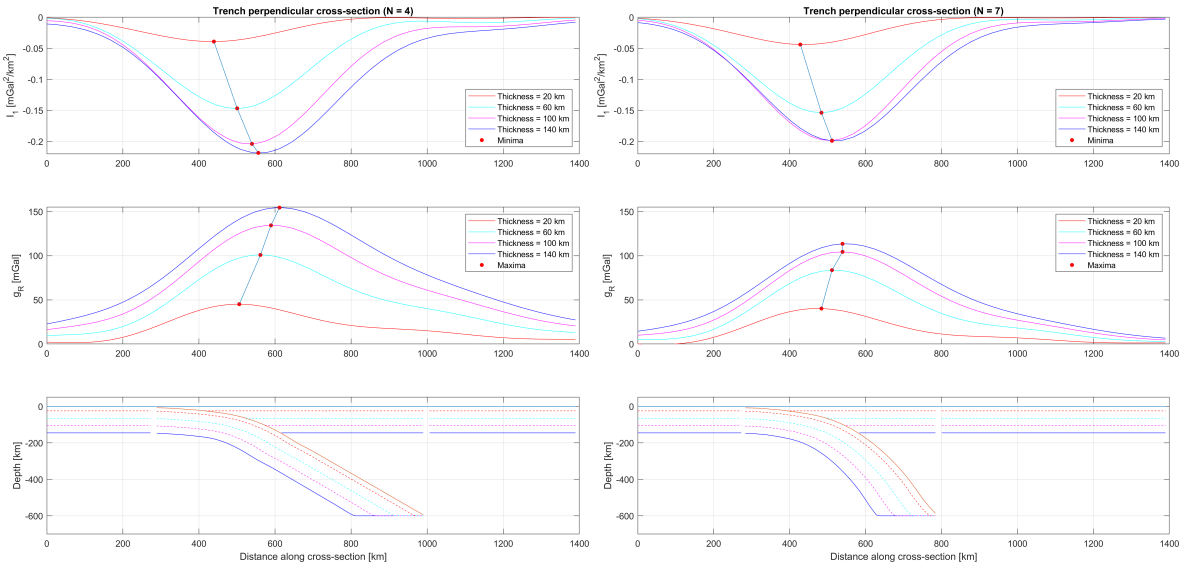

Figure 6.16: Gravity (g_R, I_1) cross-sectional results (GST2), the line colours in the model (bottom plot) correspond to the g_R and I_1 results

Thickness has a more significant contribution to the position of the signal than the maximum slab depth (GST1). From 'Max. thickness = 20 km' to 'Max. thickness = 60 km' in N=4, the signal moves approximately 60 km away from the trench. Secondly, both the g_R and I_1 signal become wider for increasing thickness. At N=7, the amplitude of I_1 does not increase beyond a slab thickness of 100 km.

Comparing the extreme values of GST1 and GST2 led to three observations, see Figure 6.15. Pay attention to the different x-axis, for GST1 it is maximum slab depth and for GST2 it is slab thickness. Firstly, the same values are obtained for 600 km depth in GST1 as for 100 km slab thickness in GST2, because those parameters represent the nominal model. Secondly, considering the slab thickness range 20-120 km and the slab depth range of 200-600 km, changing the slab thickness leads to a more significant change in gravity signal, which can be seen in the steeper gradients in Figure 6.15c and Figure 6.15d. Considering the whole range, the gradient of the depth-gravity relation is 0.19 mGal/km and 3.3×10^{-4} mGal^2/km^3 (GST1), whereas the gradient of the thickness-gravity relation is 0.91 mGal/km and 14.9 $\times10^{-4}$ mGal^2/km^3 (GST2). This is because changing the slab thickness (GST2) will add more mass closer to the surface, which larger influence on the gravity signal than adding mass at large depths, as is done when increasing the slab maximum depth (GST1). As explained before, masses close to the surface have a much larger effect on g_R and I_1. Thirdly, the signal seen in Figure 6.16 for GST2 shows more offset for different cross-section locations, in this case N=4 and N=6, than GST1.

The input slab model has varying parameters along the subduction zone, most notably, its strike and dip angles in shallow regions. Increasing the slab thickness leads to an increase in the signal from the shallow regions, and therefore increases the differences between locations with different strike and dip angles. From residuals plots for g_R and I_1 in Figure 6.17, changing the slab thickness mainly influences the signal in the Andaman Sea and northern Sumatra region. This region is more sensitive to changing slab thickness than the Burma or Java region, again related to the relatively less steep dip angle present there. Moreover, a weak I_1 anomaly following the trench is observed in Figure 6.17b, which is not seen for g_R. The nominal model has lithosphere and slab thickness of 100 km, whereas the given GST2 model has a lithosphere and slab thickness of 140 km. This difference in thicknesses results in a difference in the GGT components at the trench, which might explain this weak I_1 anomaly following the trench.

Assuming an observation error of ~1 mGal and an approximate slab thickness of 20, 60, and 100 km, the required accuracy for g_R would be 0.7, 1.2, and 2 km. Those numbers are computed using the gradient in Figure 6.15c for N=4.

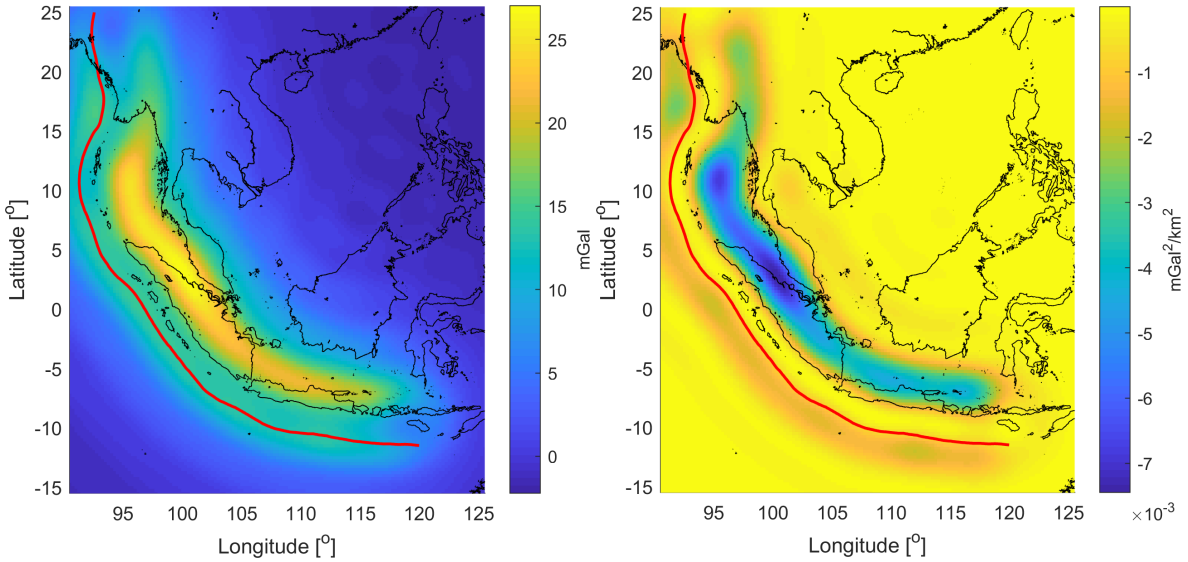

(a) g_R results (b) I_1 results

Figure 6.17: Residual plots (g_R, I_1) comparing the nominal (100 km) vs. the 140 km thickness model from GST2

6.2.4. GST3: Variable constant density of entire slab

In this sensitivity test the density of the slab was varied from 3000 to 3600 kg/m^3 in steps of 100 kg/m^3, assigning a constant density to all segments (ρ_1,...,ρ_n = const.), see Figure 6.7. A nominal mantle density of 3250 kg/m^3 was used, and the lithospheric density was set equal to the slab density.

Figure 6.18 shows that the density has no influence on the location of the peak for either g_R or I_1. Moreover, the g_R signal is symmetrical around zero, see for example the dotted lines for 'Density = 3000 kg/m^3' and 'Density = 3500 kg/m^3'. Those densities provide a slab-mantle contrast of -250 kg/m^3 and 250 kg/m^3, respectively. The positive and corresponding negative density contrast create overlapping lines for I_1 because I_1 can only be negative, therefore only four lines are visible.

For cross-section N=1 in Figure 6.18, the peaks for g_R and I_1 are located around the same point (~5 km). This is not the case for the other cross-sections (N=4,5,7). For N=4, the offset is 50 km, for N=5 and N=7 it is 60 km and 30 km, respectively. Except for N=1, the peak of g_R is positioned close to the intersection of the top-slab with the lithosphere. This characteristic could be used to locate the mantle wedge or estimate the thickness of the continental lithosphere. For all cross-sections, the I_1 peak is located where the bottom-slab surface is at 200 km depth.

The peaks for I_1 are closer to the trench than the peaks for g_R because shallow masses have a more significant influence on I_1 than on g_R (Yu and Zhao, 2010). As the shallower masses are positioned closer to the trench, likewise I_1 has its signal positioned closer to the trench. The dip angle determines the severity of the longitudinal difference between peaks of g_r and I_1. For steep dip angles the deeper masses are located closer to the trench and therefore g_R and I_1 will have their peaks closer than for shallow dip angles (e.g. N=1), where the slab mass is more spread out away from the trench (e.g. N=4).

6.2.5. GST4: Variable density with depth within slab

This test will quantify the effect of different density distributions on the position and magnitude of the gravity signal. The slab is segmented with depth in order to apply a density distribution. A user-defined segmentation is used which corresponds to the contour-lines from Figure 4.2. Thinner segments (10-25 km) between 0 and 150 km are modelled, as more segments will allow for a more smooth and realistic density distribution throughout the slab. Having a smooth distribution is necessary, because of the large sensitivity to density contrasts between 0 and 200 km, which was concluded from GST3. The interpolation resolution of the top and bottom slab model deteriorates with depth due to the large dip angles below 200 km. Therefore, thicker segments (50 km) for deeper layers ensure that the segments are well-connected to the top and bottom slab without showing interpolation artefacts.

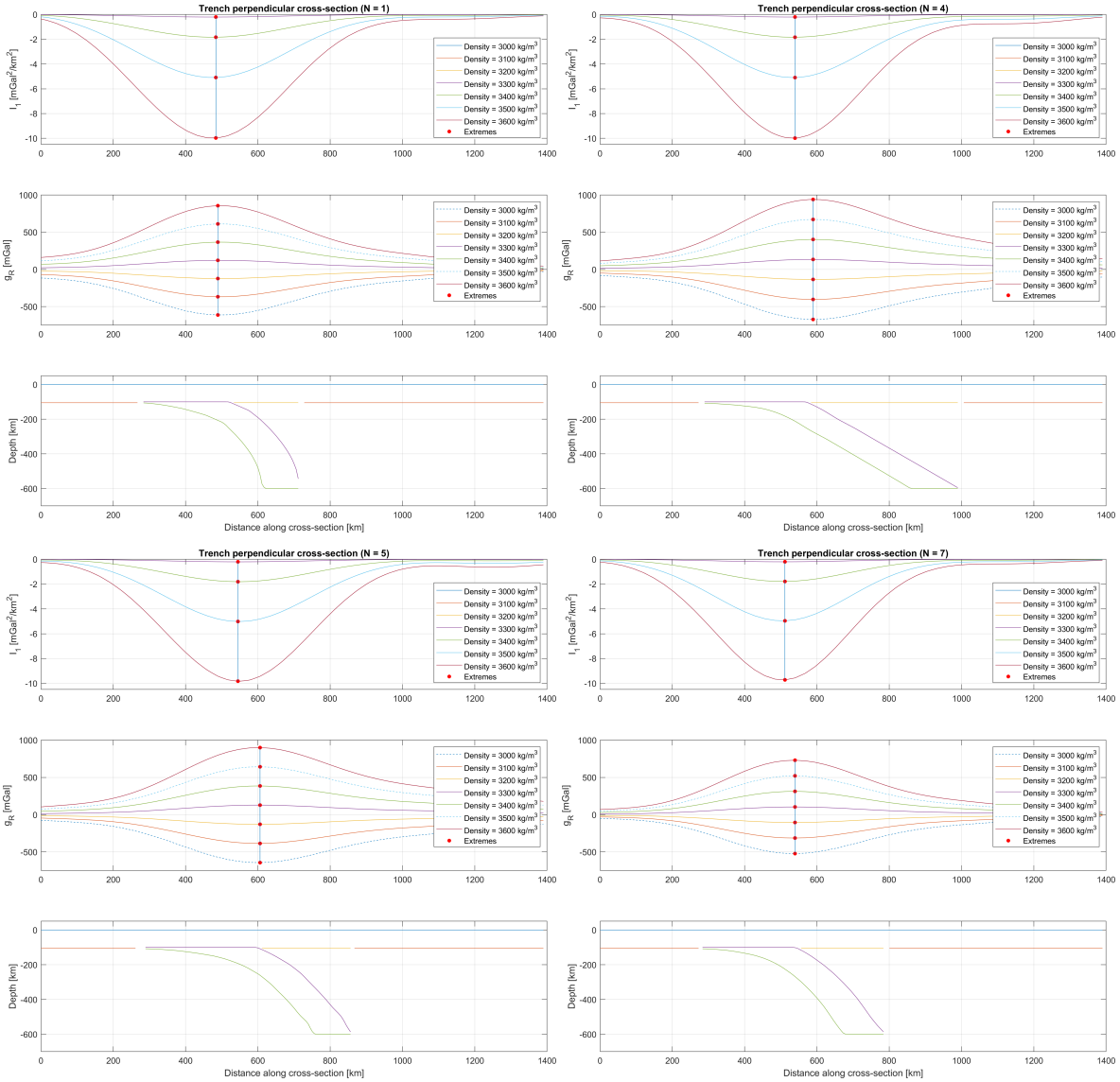

Figure 6.18: Gravity (g_R, I_1) cross-sectional results (GST3), where the dotted lines highlight the symmetry for g_R

To simplify the model, only a slab-mantle density contrast was applied, assuming a zero density contrast between the lithosphere and the slab. Two different density distributions were used in this sensitivity study, see Figure 6.19: a linearly increasing density distribution, and a diamond shaped density distribution. Both density distributions assume no density contrast between the slab and the lithosphere, therefore, the density contrast is zero until 100 km depth, which is the lithospheric base depth. The linear distribution assumes the maximum slab-mantle contrast (e.g. 10, 25, 50 kg/m^3) occurs at the slab bottom, whereas the diamond distribution applies this maximum contrast at 350 km. Those two density distributions were chosen to provide insight into the different density distributions and their effect on the gravity signal. Moreover, the diamond shaped density distribution will investigate the effect of placing the maximum density at a depth of 350 km. The different density distributions are referred to using the abbreviation Density distribution (*DD*). Figure 6.20 shows the residuals between the nominal model and the linear and diamond *DD*1. Using a density distribution significantly decreases the g_R and I_1 signal. The nominal model uses a constant density contrast of 50 kg/m^3 for the whole slab, which creates a much stronger signal for the shallow parts of the slab, where the *DD* apply small density contrasts. Moreover, the linear *DD* gives larger residuals than the diamond *DD*, which is related to the fact that the maximum density is applied for a shallower layer.

The cross-sectional results for both the *DD* are presented in Figure 6.21. Note that only the positive density distributions (*DD*1,*DD*3,*DD*5) are plotted. The negative density distributions (*DD*2,*DD*4,*DD*6) will simply give an equal but negative g_R signal and an identical I_1 signal. Analysing the difference between linear *DD* and diamond *DD*, three conclusions can be made with respect to the gravity results presented in Figure 6.21. Firstly, the g_R and I_1 signal's amplitude for diamond *DD* is larger than for linear *DD* because more mass is modelled around 350 km depth as a result of the higher density contrast. Secondly, this larger amount of mass between 200-400 km depth causes a very small movement of the g_R signal towards the trench, in the order of 5-30 km. This minimal movement is an indication that the segments above 400 km completely overpower the gravity signal from deeper segments. This is in line with the conclusion from GST0, that the signal between 100-300 km depth is 3 to 6 times larger than between 400-600 km depth, see Subsection 6.2.1. Between the linear and diamond *DD*, there is also a slight movement of the I_1 signal's minima towards the trench. Thirdly, the g_R signal for diamond *DD* declines slightly quicker for its down-going leg than for linear *DD*, which is seen when comparing linear *DD*1 with diamond *DD*1 in Figure 6.21. This shows that a negative density gradient effects the gravity signal's down-going leg. This difference is small as density contrasts below 400 km exercise negligible effect on the total gravity signal.

Changing the gradients in the linear and diamond density distributions only resulted in an increased signal amplitude but no change in peak location, see *DD*1, *DD*3, *DD*5. Therefore, no conclusions can be made on the interplay between density gradients and the gravity-depth effect. It was assumed that if a relatively higher density was applied to segments at larger depths, their gravity signal might become stronger, and therefore, the gravity-depth effect might be mitigated or decreased. This would translate into a movement of the peak. From this test it was concluded that linear density gradients (Figure 6.19) cannot mitigate the gravity-depth effect. Other gradients should be investigated, for example quadratic equations (Dziewonski et al., 1975).

A first-order correlation between dip-angle and signal amplitude is observed when comparing the different cross-sectional plots in Figure 6.21. For cross-sections N=3 and N=4, the dip-angle is lower than for N=6 and N=7, and therefore the amplitude of the signal is larger. The same correlation is observed for the steeper dipping slab at N=7, which has a lower signal amplitude than at N=6. At steeper dip-angle the segments have less volume, and therefore less mass and a less strong gravity signal.

6.2.6. GST5: Age-based along-trench thickness distribution for entire slab

This test will investigate the gravity effect of using a non-constant slab thickness distribution based on trench age data, see Figure 4.10a. The nominal slab model for GST1-GST4 includes a lithosphere which connects with the slab at the trench. In this test the slab thickness at the trench will vary along-strike. The subduction zone is characterized by oblique convergence. As explained in Subsection 4.4.2, an innovative way was chosen to use propagate the trench age data over the slab using the subduction direction and rate. After which, the plate thickness was computed using equations explained in Section 4.3.

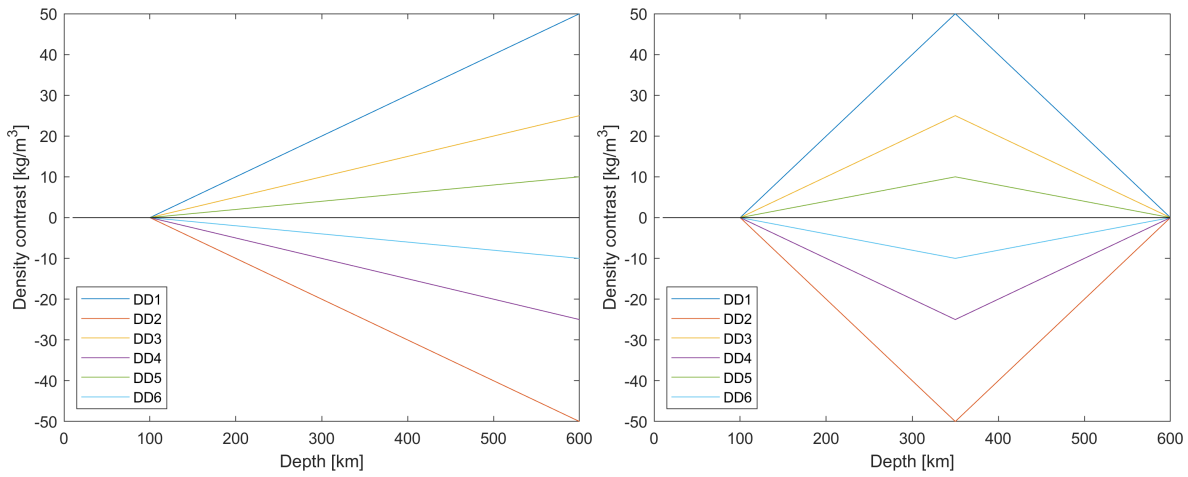

(a) Linear density distributions

(b) Diamond density distributions

Figure 6.19: Theoretical density distributions used for GST4

Normally, the algorithm would adjust the lithospheric thickness such that it connect perfectly with the slab at the trench. However, for this test, one is varying the slab thickness along the trench, therefore it is not possible to have a consistent fitting lithosphere. Therefore, a constant lithosphere thickness of 105 km is used, which is the same value as for the nominal model.

The half-space cooling model by Turcotte et al. (1978) was used to compute the thickness of the slab. The simulations were run for the weighted and unweighted HS, while investigating two values of thermal diffusivity, κ_{high} = 1E-6 and κ_{low} = 8E-7 m^2/s. Recall, that the thickness is constant in subduction direction of $\phi_{sub} = 30°$. The slab thickness plots are shown in Figure 6.22. Decreasing the thermal diffusivity decreases the slab thickness for the whole subduction zone proportionately to $\sqrt{\kappa}$, see Equation 3.3. No other effects are observed for changing $\sqrt{\kappa}$. The thickness for the weighted HS, see Figure 6.22d, shows a much smaller range of 86-106 km, whereas the original HS has a thickness range of 85-160 km.

The results for different cross-sections are shown in Figure 6.23, where the colours of bottom slab (bottom sub-plot) correspond to the colours of the gravity results (upper sub-plots). The nominal slab model and its gravity results are displayed using red dashed lines. As was observed for GST2, increasing the slab thickness results in the signal's maximum to swift towards the trench while increasing the overall amplitude of the signal, read Subsection 6.2.3. Moreover, the weighted HS curves for the bottom slab (bottom sub-plot) are close to the nominal model, which has a constant thickness of 100 km. This is because the weighting factor applied to the weighted HS equation causes it to convergence to a plate thickness of ~107 km, see Figure 3.5, whereas the original HS equation let's the plate thickness divergence with increasing age. N=3 shows that the amplitude of the gravity signal is lower than for the nominal signal, as the young age in this region correlates to a smaller slab thickness. The opposite is true for N=7, where amplitude of the gravity signal is higher than for the nominal model, due to the older thicker slab. As concluded before, different values of κ will only influence the amplitude, which is seen by the purely vertical increase for the maximum values of g_R and I_1 (red dots).

The effects of the age-based thickness distributions are better visible looking at the in-plane gravity residual with the nominal slab model, see Figure 6.24. The slab thickness models based on the original HS equation, see Figure 6.24a and 6.24b, give positive gravity anomalies south of Java, and negative anomalies at northern Sumatra, with minimum values of -16 and -35 mGal for κ_{high} and κ_{low}, respectively. The weighted HS models also show negative anomalies at northern Sumatra, with minimum values of -19 and -37 mGal for κ_{high} and κ_{low}, respectively. The positive anomaly has completely disappeared for Figure 6.24d. Quantitative analysis showed that a decrease of 2E-7 m^2/s for the thermal diffusivity decreases the overall gravity signal's amplitude in the subduction zone by ~20 mGal.

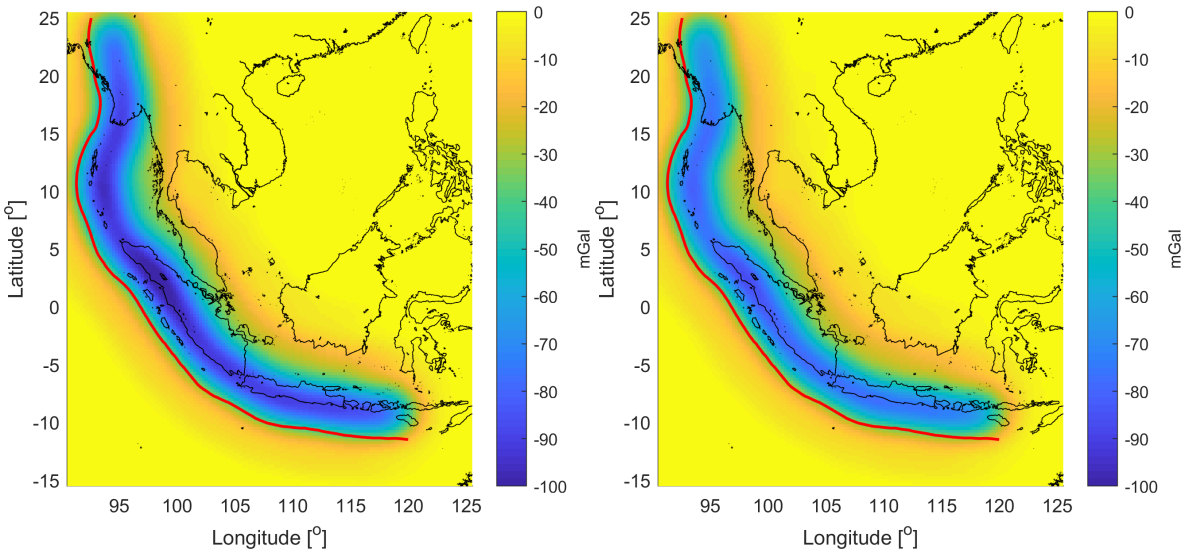

(a) g_R results for linear density distribution (DD1)

(b) g_R results for diamond density distribution (DD1)

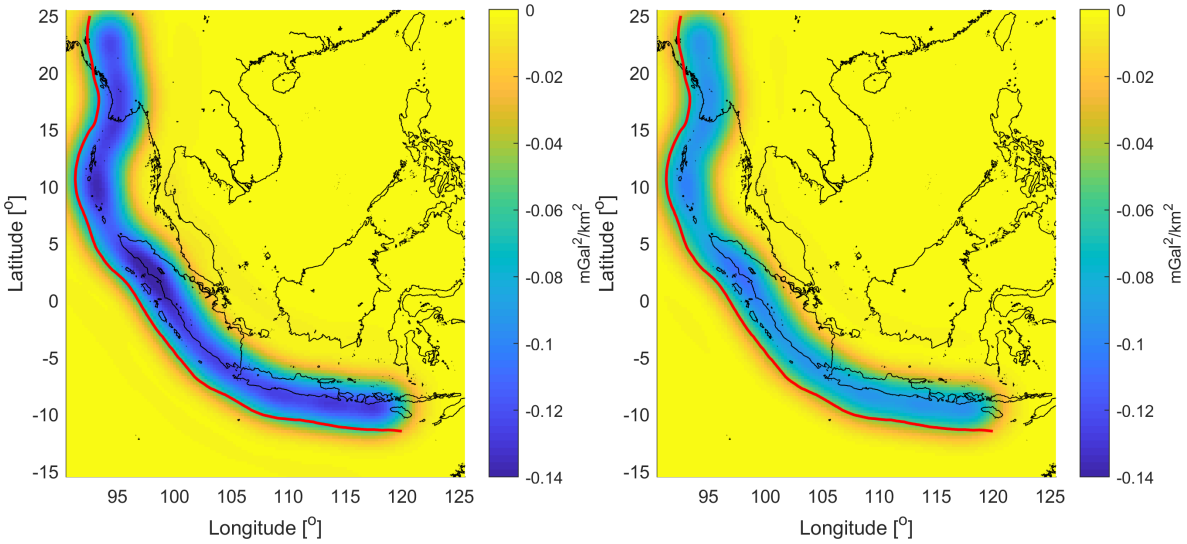

(c) I_1 results for linear density distribution (DD1)

(d) I_1 results for diamond density distribution (DD1)

Figure 6.20: Residual plots (g_R, I_1) comparing different density distributions with nominal model (GST4)

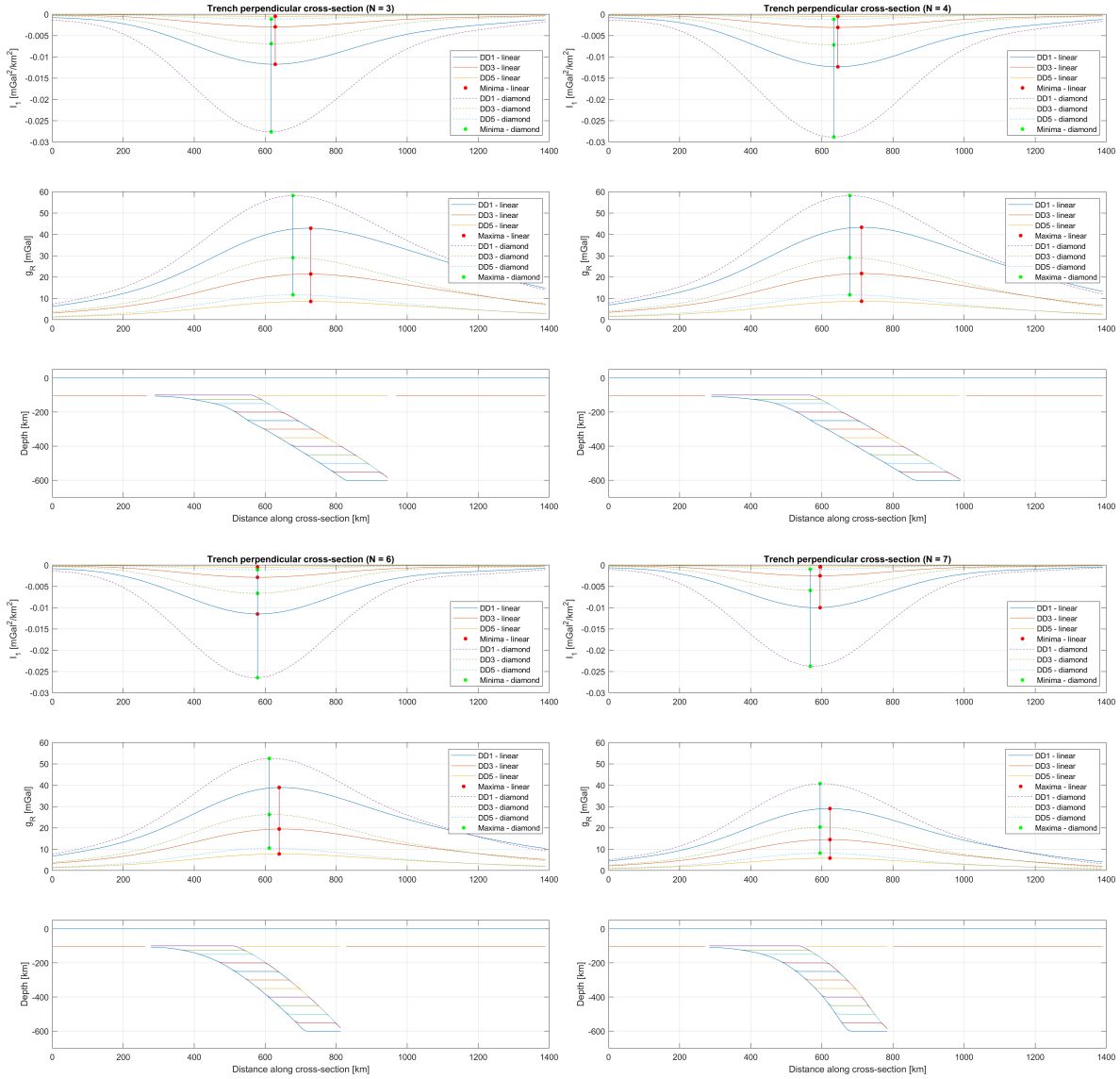

Figure 6.21: Gravity (g_R, I_1) cross-sectional results (GST4)

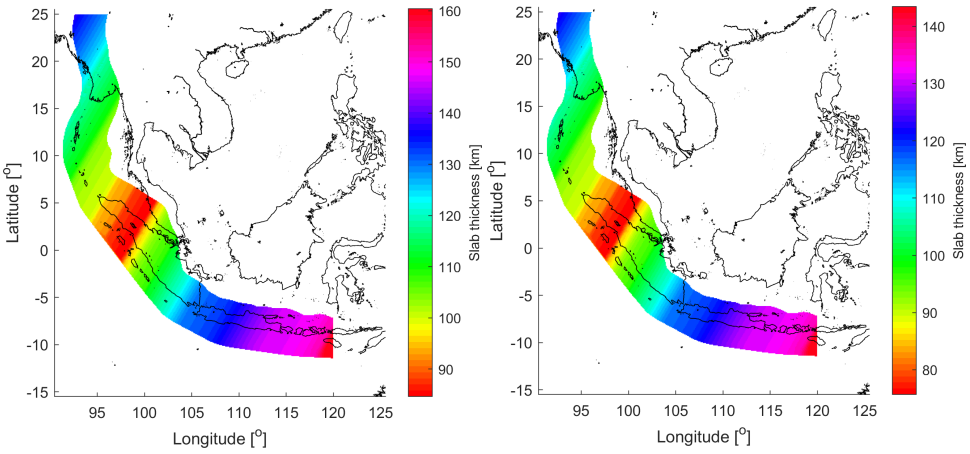

(a) HS, κ_{high} =1E-6 m^2/s

(b) HS, κ_{low} =8E-7 m^2/s

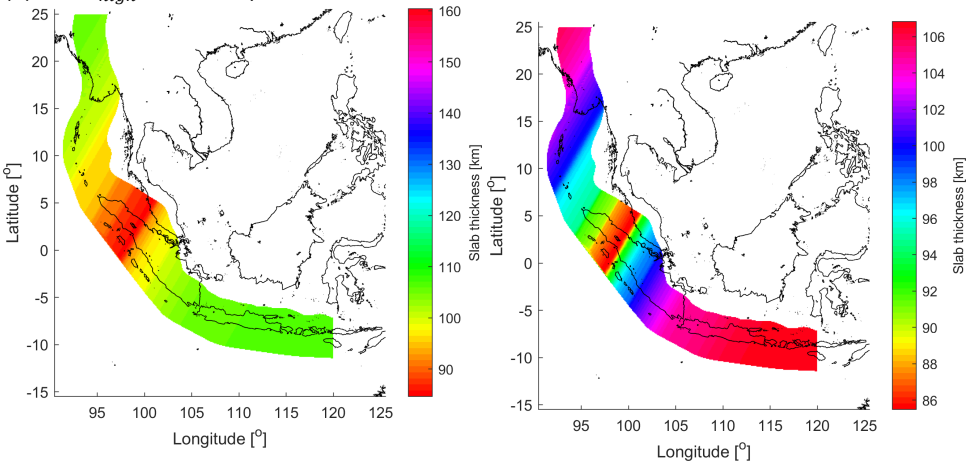

(c) Weighted HS, κ_{high} =1E-6 m^2/s, equal colorbar

(d) Weighted HS, κ_{high} =1E-6 m^2/s

Figure 6.22: Thickness distributions for GST5

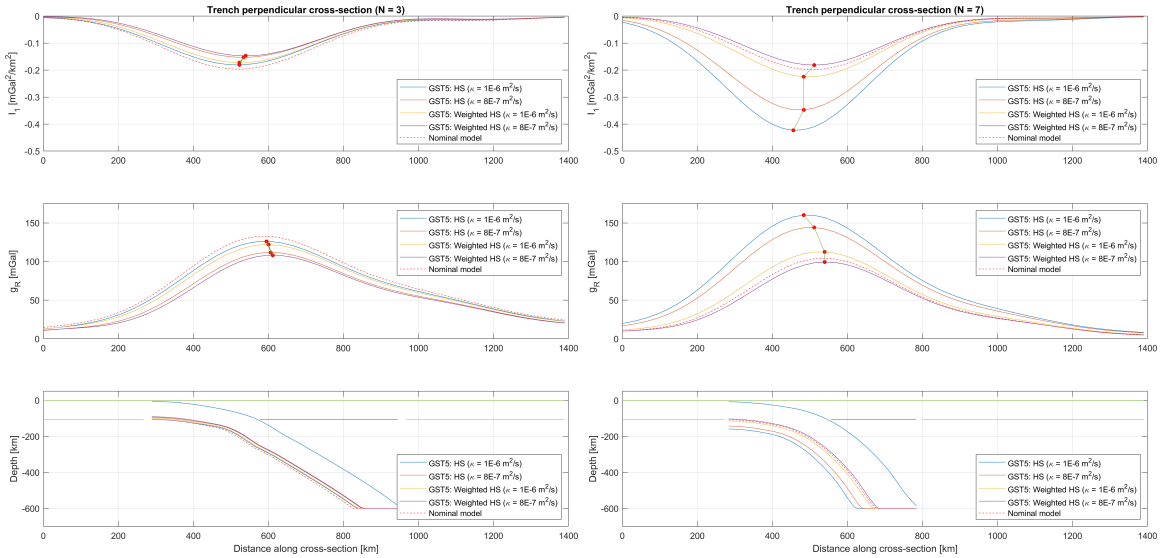

Figure 6.23: Gravity (g_R, I_1) cross-sectional results (GST5), dashed red lines depict nominal slab model (constant 100 km slab thickness)

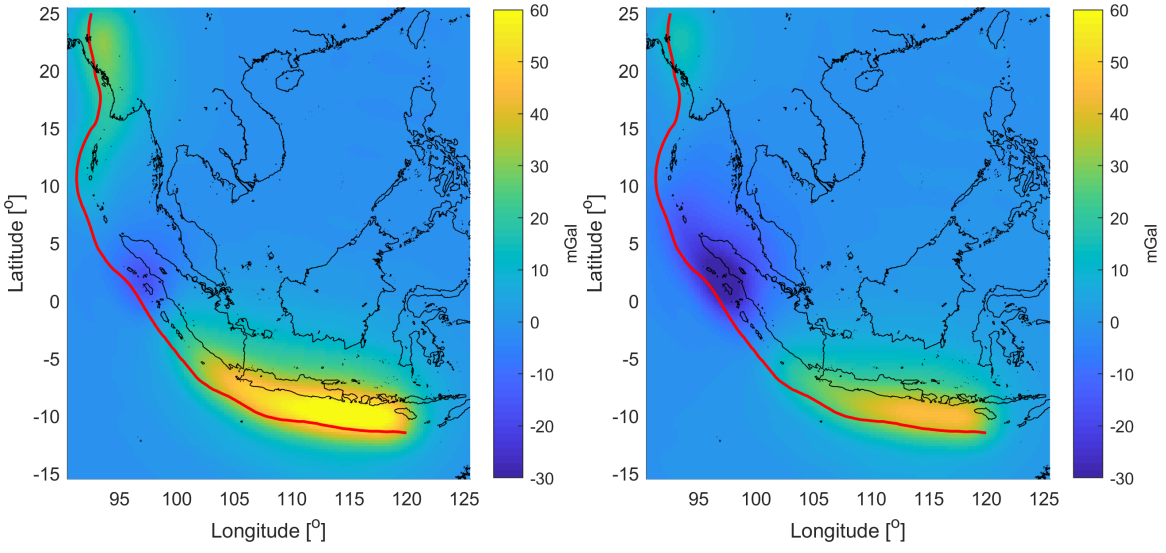

(a) HS, κ_{high} =1E-6 m^2/s

(b) HS, κ_{low} =8E-7 m^2/s

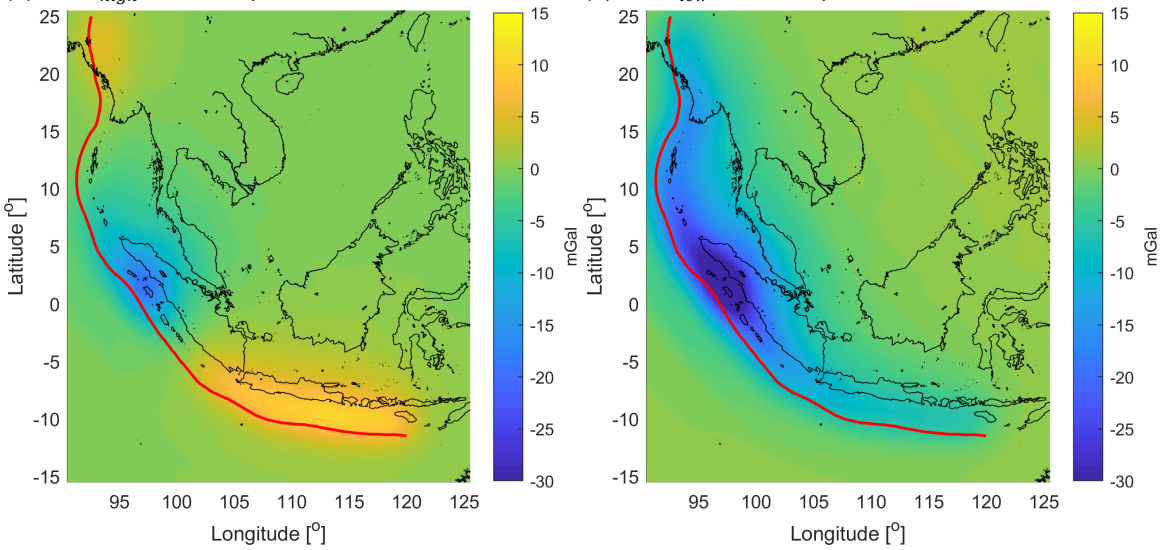

(c) Weighted HS, κ_{high} =1E-6 m^2/s

(d) Weighted HS, κ_{low} =8E-7 m^2/s

Figure 6.24: Residual plots (g_R) comparing with nominal model (GST5)

The second invariant residuals (I_1) for the original HS models also show an anomaly at northern Sumatra. When decreasing κ_{high} to κ_{low}, the second invariant increases from -0.008 to -0.2 mGal^2/km^2 in northern Sumatra, whereas the signal decreases from -0.07 to -0.035 mGal^2/km^2 in the Java region. For the weighted HS model the anomaly south of Java is virtually absent, having values of -0.001 and -0.0008 mGal^2/km^2 for κ_{high} and κ_{low}, which are accompanied by increasing I_1 extreme values of -0.008 and -0.2 mGal^2/km^2 for northern Sumatra. Concluding, the I_1 residuals support the same observations which were made for g_R, in the previous paragraph. The second invariant is more sensitive to mass anomalies than the radial gravity. Therefore, the second invariant shows saturated results more quickly, which in turn obliterate smaller anomalies and give larger magnitude differences between different anomalies.

6.2.7. GST6: Age-based thickness distribution varying in dip-direction based on subduction rate/direction

The addition of a more sophisticated slab thickness model based on lithospheric ageing in subduction direction will be investigated with respect to its residual gravity signal with the nominal model. Whereas GST5, see Subsection 6.2.6, used a constant age in subduction direction, this test will use the age dis-

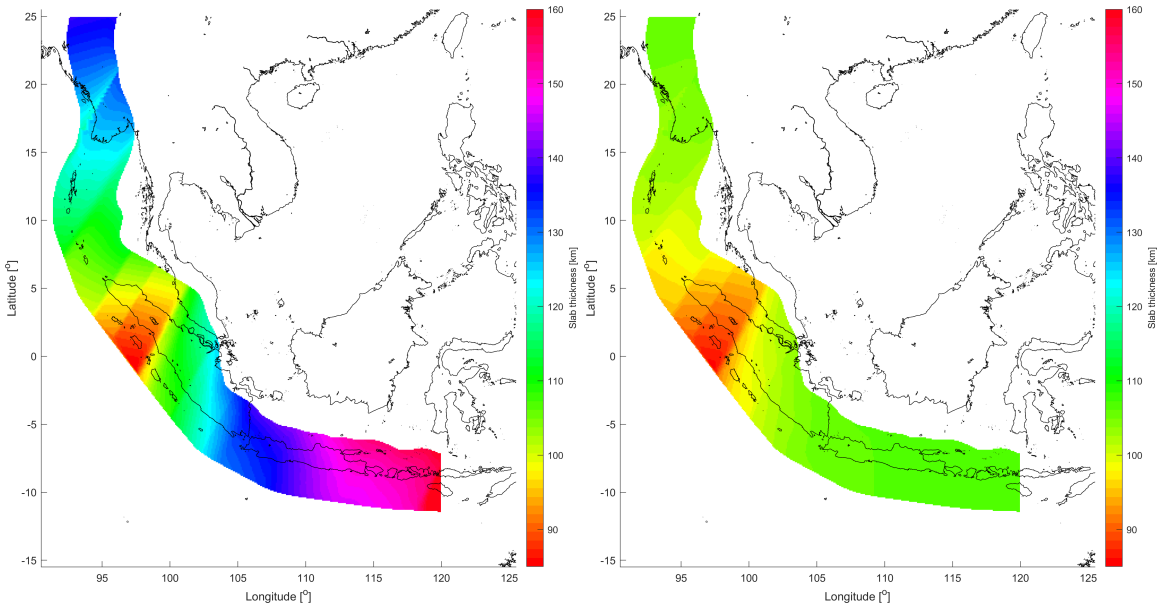

(a) HS, κ_{high} =1E-6 m^2/s (b) Weighted HS, κ_{high} =1E-6 m^2/s

Figure 6.25: Thickness distributions for GST6

tribution given in Figure 4.10b, which was derived using the methodology explained in Subsection 4.4.2. For reasons explained in GST5, a constant lithospheric thickness of 105 km is used.

As was concluded in GST5, increasing the thermal diffusivity (κ) will solely increase the slab thickness, but not add any new features to the slab model. The slab thickness models for HS and weighted HS for κ_{high} are given in Figure 6.25. The models for κ_{low} are not given here. Including ageing primarily impacts the region between middle and northern Sumatra, which is again the shallow dip-angle region, recall Figure 4.4b. Comparing Figure 6.22a and 6.25a, one sees that the thickness in the region around Java is increased and expanded. Moreover, the slab thickness is increased by ~20 km in the region where the subduction zone reaches Thailand. This is due to the fact that those slab segments have travelled the longest distance from the trench, and therefore have the largest increment in age with respect to the trench age, assuming the given subduction direction of 30° is correct. To recall the algorithm that is used to compute the age increment, see Figure 4.9. This large increment in age translates directly into a large increment in slab thickness under Thailand compared to the constant age slab thickness model of GST5.

Including slab ageing leads to a slight increase in both the g_R and I_1 signal, which is observed when comparing N=3 in Figure 6.23 6.26. For N=7, no significant change is observed between GST5 and GST6.

The in-plane gravity residuals between the age-based slab model and the nominal model will be similar to the results presented in Subsection 6.2.6. Therefore, it is more intuitive to investigate changes in gravity signal from GST5 to GST6, which are shown in Figure 6.27. This figure shows the residual signal for the original and weighted HS using κ_{high}. Figure 6.27 shows that including ageing into the slab model leads to added mass in two locations, northern Sumatra and where the subduction zone reaches Thailand. The subduction zone extending between 15° and 25° is not based on real data, but on extrapolation of trench data (Broerse et al., 2014). Therefore, those gravity anomalies should be treated with caution, and will not be discussed here. The anomaly at northern Sumatra has a maximum residual of 11 and 6 mGal for the original and weighted HS model, respectively. The second invariant (I_1) shows the same residuals pattern for northern Sumatra, with minima's of 1.1×10^{-3} and -4.1×10^{-4} mGal^2/km^2, for the original and weighted HS models.

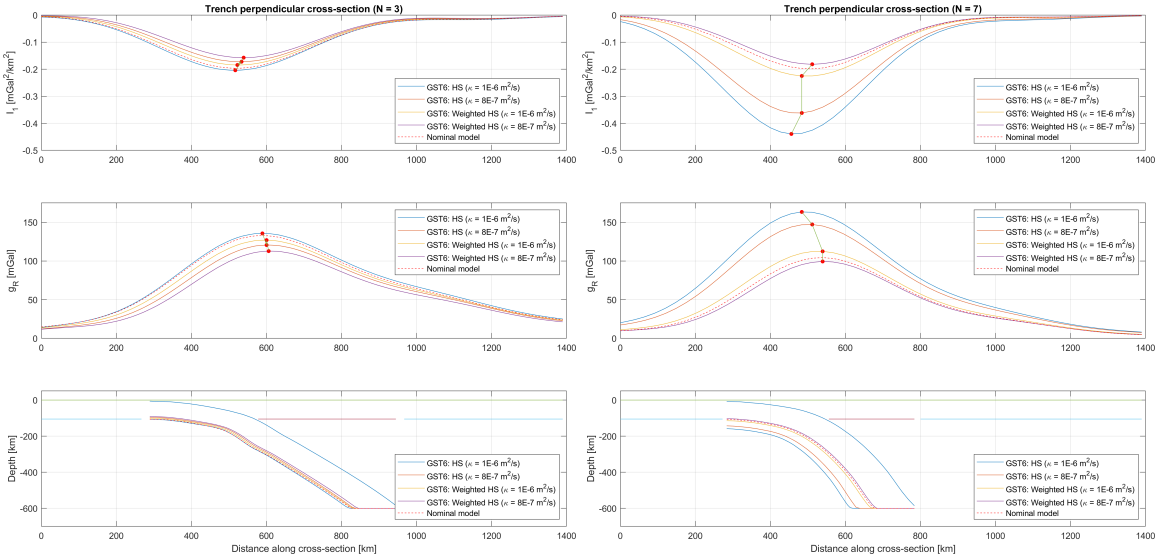

Figure 6.26: Gravity (g_R, I_1) cross-sectional results (GST6), dashed red lines depict nominal slab model (constant 100 km slab thickness)

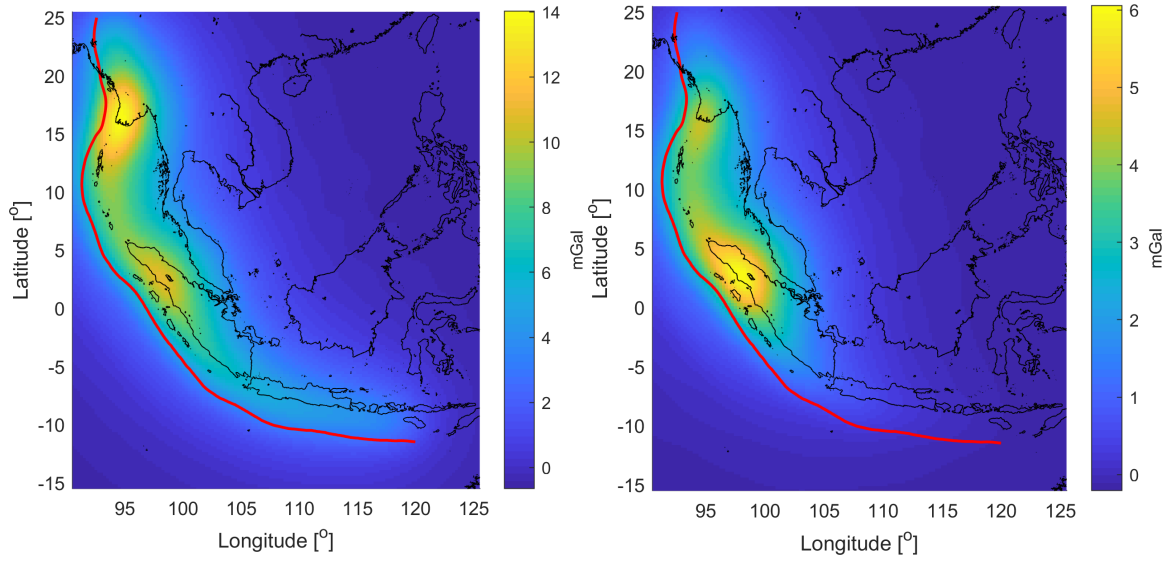

(a) HS, κ_{high} =1E-6 m^2/s

(b) Weighted HS, κ_{high} =1E-6 m^2/s

Figure 6.27: Residual plots (g_R) comparing GST5 and GT6

6.3. GST related to slab features

The following three gravity sensitivity tests (GST) will investigate the effect of different slab features on the gravity signal. The following tests will be performed:

GST7: Isostatic compensation at various depths using different layers

GST8: Addition of slab tear

GST9: Addition of subducting eclogite crust

6.3.1. GST7: Isostatic compensation at various depths using different layers

This test will investigate the effect of isostatic compensation based on Pratt's hypothesis, which assumes that isostatic equilibrium is achieved through lateral density variations. In the classic case, the lithosphere is used as rigid compensating layer that is floating on the denser asthenosphere (Kaban et al., 2004; Fowler, 2005). This classic case will be tested, together with two other cases, crustal compensation, and sub-lithosphere compensation. Compensation in the sub-lithospheric layer assumes that a certain layer of the asthenosphere sustains isostatic equilibrium. The three different compensating layers are highlighted (green) in Figure 6.29. Some important simplifications were applied. First of all, the compensating layer does not need to border with compensation depth. Secondly, only the compensating layer is used to establish isostatic equilibrium.

To create a realistic isostatic model, not only the slab was included, but also models for topography, bathymetry, sediments, crust, and lithosphere. Those models were introduced in Chapter 5. The nominal slab model is used, recall the constant thickness of 100 km, maximum depth of 600 km, density contrast of 50 kg/m^3. The isostatic reference mass column consists a 30 km crust of 2850 kg/m^3, a 70 km lithosphere of 3300 kg/m^3, and a 900 km mantle of 3250 kg/m^3, see Figure 6.28. The mass of the reference column is computed as follows:

$$m_{reference} = t_{crust}\rho_{crust} + t_{litho}\rho_{litho} + t_{mantle}\rho_{mantle} \tag{6.5}$$

Where t is the layer thickness, and ρ the layer density. The reference column is adjusted in accordance with the compensation depth. For example, a compensation depth of 300 km would lead to a reference column of 300 km, consisting of 30 km crust, 70 km lithosphere, and 200 km mantle. For a compensation depth of 100 km, no mantle will be included in the reference column. The actual mass column is computed as follows:

$$m = \sum_{i=1}^{N_{models}} t_i\rho_i \tag{6.6}$$

In this test, seven different models were used: topography, bathymetry, sediments, crust, lithosphere, slab, and mantle. The isostatic density is computed using the thickness (t_{comp}) of the compensating layer :

$$\rho_{iso} = \frac{m_{reference} - m}{t_{comp}} \tag{6.7}$$

Isostatic equilibrium is achieved by adding the isostatic density (ρ_{iso}) to the nominal density of the compensating layer.

Three different compensation depths are tested, 100, 300, and 600 km. Using a compensation depth of 100 km the assumption is made that the slab is not compensated at all. This is based on the situation where the subducting slab under 100 km finds itself in a fluid-like mantle, which cannot compensate the slab mass (Kaban et al., 2004). Therefore, only the upper 100 km (topography, bathymetry, sediments, crust, lithosphere) will be compensated. For a compensation depth of 300 km, the most substantial part of the slab signal will be compensated, recall from GST1 that 80% of the slab g_R signal is between 0 and 300 km depth. Compensation down to 600 km will allow for the whole slab to be in isostatic equilibrium. Only the radial gravity (g_R) will be investigated. The second invariant is neglected in this test, because of its insensitivity to masses below 200 km, recall Table 6.1.

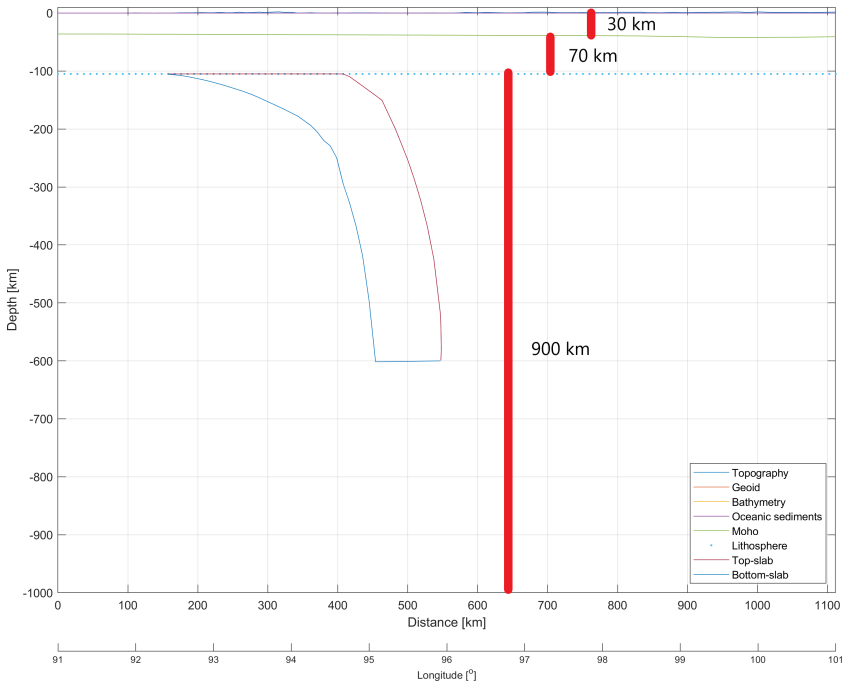

Figure 6.28: Reference mass column for isostatic equilibrium: 30 km crust of 2850 kg/m^3, 70 km lithosphere of 3300 kg/m^3, and 900 km mantle of 3250 kg/m^3 (GST7)

Compensating lithosphere

The compensating lithosphere, shown (green) in Figure 6.29a, is defined between the Moho and the base of the lithosphere. The isostatic densities range from -150 to 250 kg/m^3, see Figure 6.30. Applying compensation down to a depth of 100 km, does not equilibrate the gravity signal of the slab. The opposite is true, because shallow Earth layers (topography, bathymetry, etc.) are being compensated, the gravity anomaly related to the slab is less obstructed and therefore more visible, especially in the Andaman Sea. From Java to northern Sumatra, the nominal slab signal in Figure 6.14a is clearly observed as the positive anomaly in compensated signal, see Figure 6.30b. Increasing the compensation depth to 300 km results in almost the entire slab signal to be compensated, see Figure 6.30d. This is correspondence with GST1, where it was concluded that the top 300 km of the slab contributes most to the gravity signal. A weak positive anomaly following the Andaman Coast of Thailand is still visible, which is not related to the subduction zone.

Increasing the compensation depth to 600 km results in overcompensation. In essence, overcompensation reproduces the compensated mass anomaly into a gravity anomaly. The distinct negative gravity anomaly in Figure 6.30f, corresponds to the location of the lower slab. The lower slab is not being captured in the gravity signal. But when compensated in the lithosphere, a mass anomaly of opposite sign is added to the lithosphere at the same lateral location. The lithosphere is closer to the surface, and thus, has a larger effect on the gravity signal measured at sea-level. It is therefore possible that a negative mass anomaly deep in the Earth, results in a positive gravity anomaly, and vice versa, when a significantly large compensation depth is assumed.

Concluding, the lithosphere is able to compensate the slab down to 300 km depths. For deeper compensation depths, overcompensation of the slab results in large isostatic densities that explain the large negative gravity anomalies following along the subduction zone. For a compensation depth of 100 km, the slab is not compensated at all.

Compensating crust

The compensating crust (green) is shown in Figure 6.29b. In certain regions the oceanic sediments base would be positioned deeper than the Moho top, which would result in a negative thickness for the crust. Therefore, the compensating crust is defined between the bathymetry and Moho, and the sediment model is neglected.

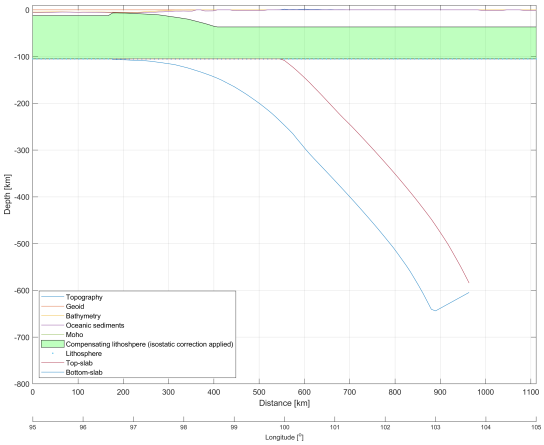

(a) Compensating lithosphere

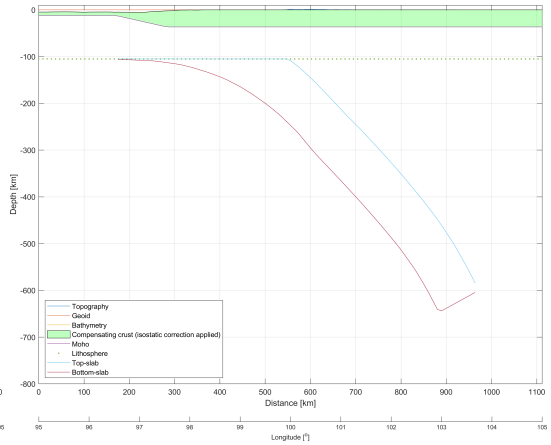

(b) Compensating crust

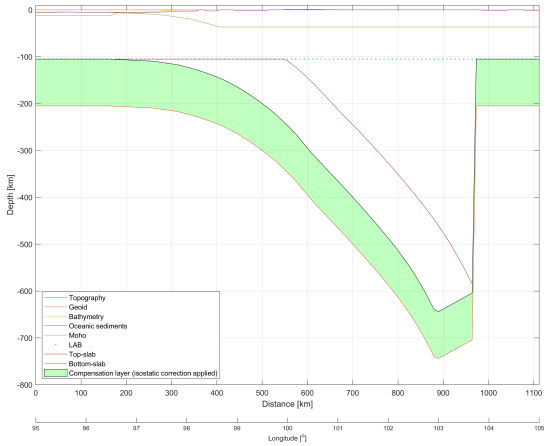

(c) Compensating sub-lithospheric layer

Figure 6.29: Model cross-sections (West-East) at $\phi = 0°$ (GST7)

The compensating crust shows a similar gravity signal for the different compensation depths as for the compensating lithosphere, see Figure 6.31. However, the isostatic densities are much larger, ranging from -400 to 600 kg/m^3 in the subduction zone. This is due to the much smaller compensating thicknesses (t_{comp}) of the crust. This is particularly true for oceanic crust, which has a thickness that ranges between 5 and 10 km, whereas the continental thickness is 35 km, see Figure 6.32. It is interesting to see the patterns of the North-South transform south of Sumatra, see Figure 6.31a. Transform faults and spreading centres are very local and short-wavelength features in the bathymetry (Hall and Spakman, 2015), and this test shows that the crust is able to compensate those features in the gravity signal.

Concluding, the crust is the most effective compensating layer for shallow mass anomalies. This is seen in the smooth gravity signal in the ocean south of the trench, see Figure 6.31b. However, the required crustal isostatic densities are unrealistic for the investigated compensation depths. Moreover, compensation depths below 300 km resulted in the slab being overcompensated.

Compensating sub-lithospheric layer

The compensating sub-lithospheric layer is defined with the LAB as top, and has a constant thickness of 100 km, see (green) in Figure 6.29c. From all three compensation depths, it is clear that the sub-lithospheric layer is unable to compensated the large positive mass anomaly at western Java, and the large negative mass anomaly in the Andaman Sea, see Figure 6.33. Both gravity anomalies decrease in amplitude with increasing compensation depth, because the slab signal is increasingly compensated. Those anomalies are not caused by the slab, but by the bathymetry, sediments, and the crust, see Chapter 5.
For a compensation depth of 600 km the slab signal has completely disappeared, see Figure 6.33d which has the same features as in Figure 5.7a.

The sub-lithospheric layer is the most effective layer for bringing the slab in isostatic equilibrium. As the sub-lithospheric neighbouring the slab, the overcompensation effect for the slab will be small. However, the sub-lithospheric layer is unable to compensated masses close to the surface.

When comparing all three different compensation types, several observations can be made. Firstly, the compensating thickness (t_{comp}) of the sub-lithospheric layer (100 km) is approximately the same as for the lithosphere (95 km) in oceanic regions. Moreover, $m_{reference}$ and m in Equation 6.7 are by definition equal for the compensating lithosphere and compensating sub-lithospheric layer, because the same full model is used. Therefore, the isostatic densities (ρ_{iso}) should be similar in oceanic regions, which is verified when comparing Figure 6.30e with Figure 6.33a. However, the crust is thicker in continental regions, resulting in a thinner compensating lithosphere thinner. Therefore, larger isostatic densities are present in continental regions. Secondly, all three compensation types result in an overall lower amplitude signal compared to the original signal (-150 to 500 mGal). Concluding, the compensating lithosphere is the most optimal compensating layer, having realistic isostatic density values, while being able to compensate both the slab and shallow mass anomalies for intermediate compensation depths (300 km).

6.3.2. GST8: Addition of slab tear

In this section, the effect of a slab tear on the gravity signal will be tested and described. As was discussed in the introduction, literature advocates either a slab tear or slab fold under Sumatra (Fauzi et al., 1996; Burke, 2006; Richards et al., 2007; Pesicek et al., 2010). The postulated slab tear is related to the subducting spreading ridge, see green in Figure 3.3b. The spreading ridge is said to subducted under the volcanic centre of Toba ($\phi = 2.5°$), which is the approximate location of the slab tear, although this has not been validated. For this test the effects of isostatic compensation are not considered.

Three different slab tear models will be tested. The models are similar in a sense that northward of the tear, the slab extends less deep than south of the tear (Hall and Spakman, 2015). The tear will be modelled in EW-direction (Richards et al., 2007). The latitude of the slab tear will be the varying parameter. A tear north and south of the volcanic centre of Toba will be tested, to test which location is most likely.

As a show-case, one tries to find a first-order qualitative fit between the slab model with tear and the positive anomaly in the observation model (XGM2016) in Sumatra and Java. No distinct I_1 anomaly is presented in XGM2016 that is identified for the nominal slab model, therefore, only the g_R anomaly

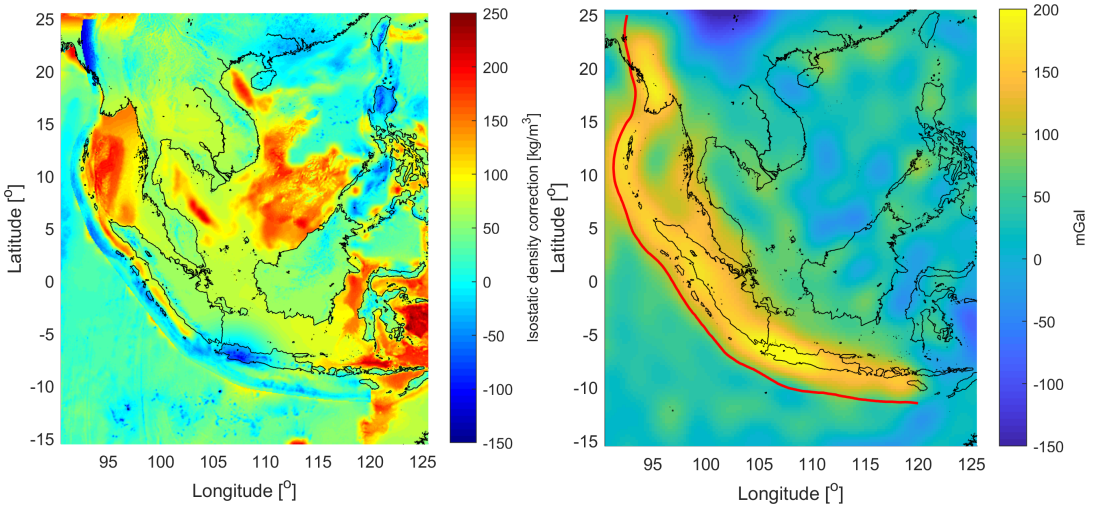

(a) ρ_{iso} for compensation depth = 100 km

(b) g_R for compensation depth = 100 km

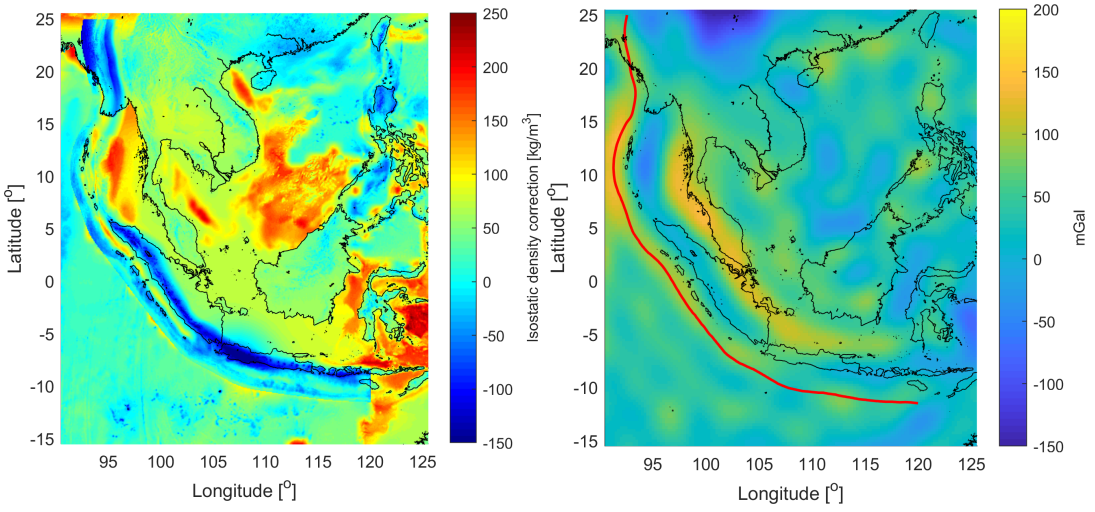

(c) ρ_{iso} for compensation depth = 300 km

(d) g_R for compensation depth = 300 km

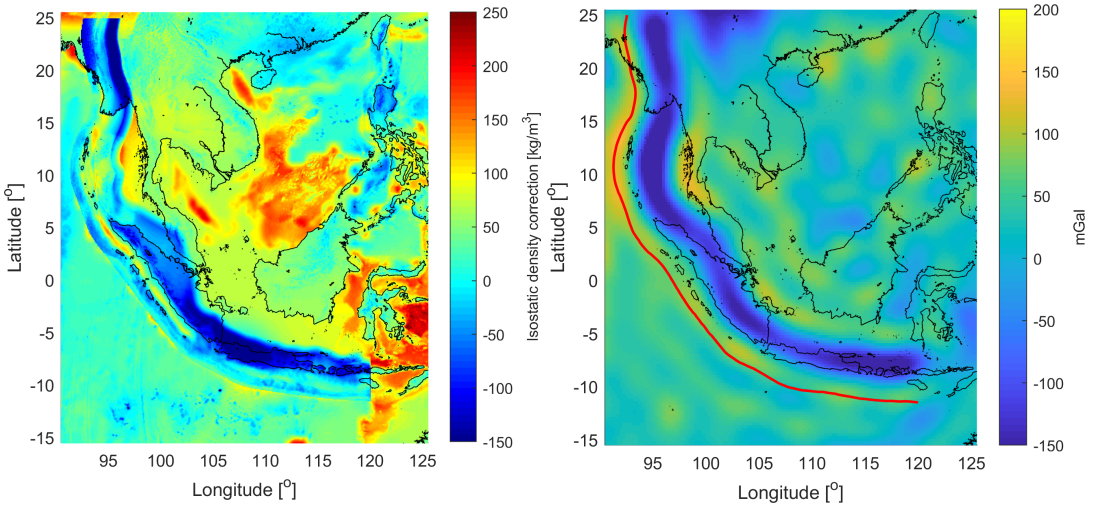

(e) ρ_{iso} for compensation depth = 600 km

(f) g_R for compensation depth = 600 km

Figure 6.30: Compensating lithosphere, SHC=3-90

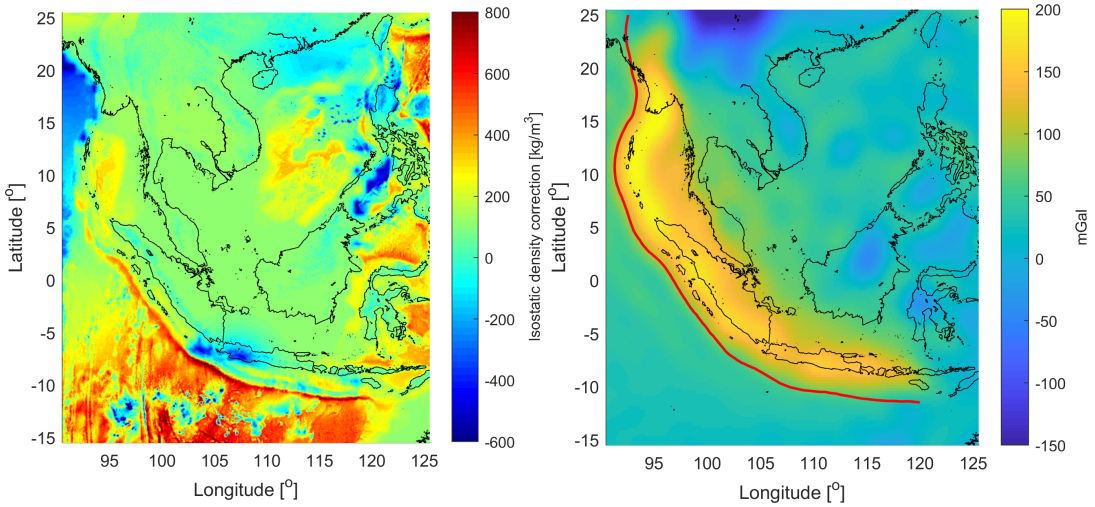

(a) ρ_{iso} for compensation depth = 100 km

(b) g_R for compensation depth = 100 km

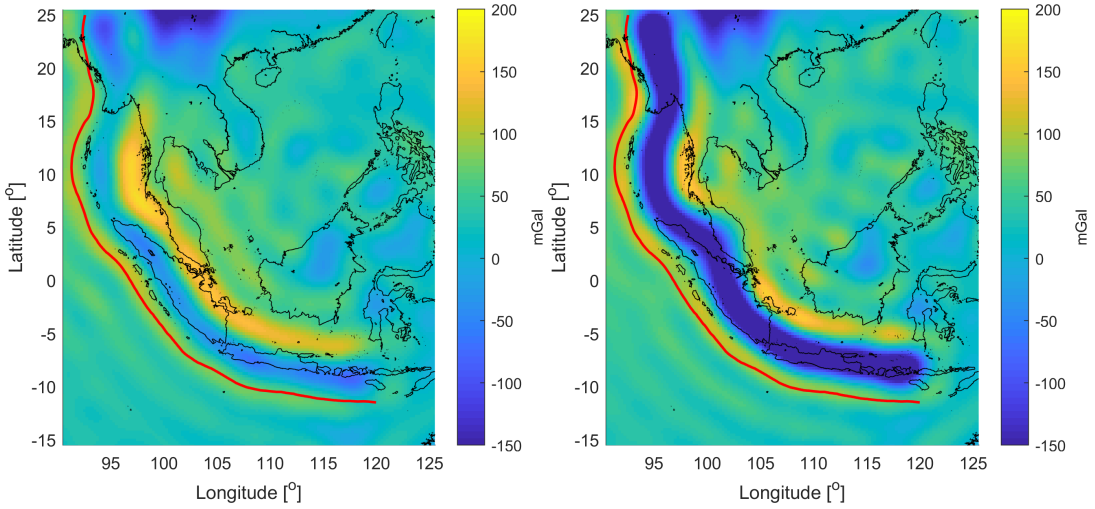

(c) g_R for compensation depth = 300 km

(d) g_R for compensation depth = 600 km

Figure 6.31: Compensating crust, SHC=3-90

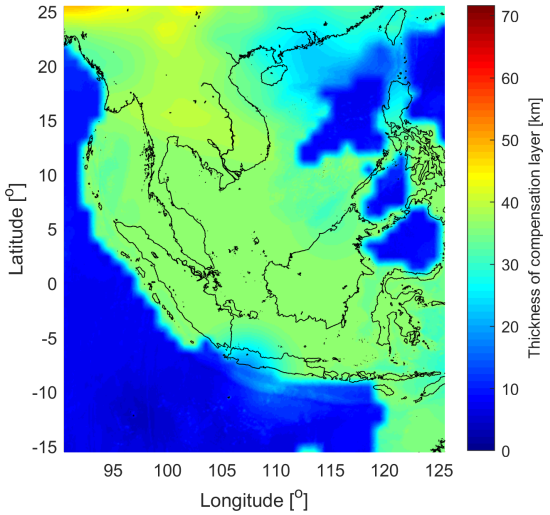

Figure 6.32: Thickness of compensating crust (t_{comp})

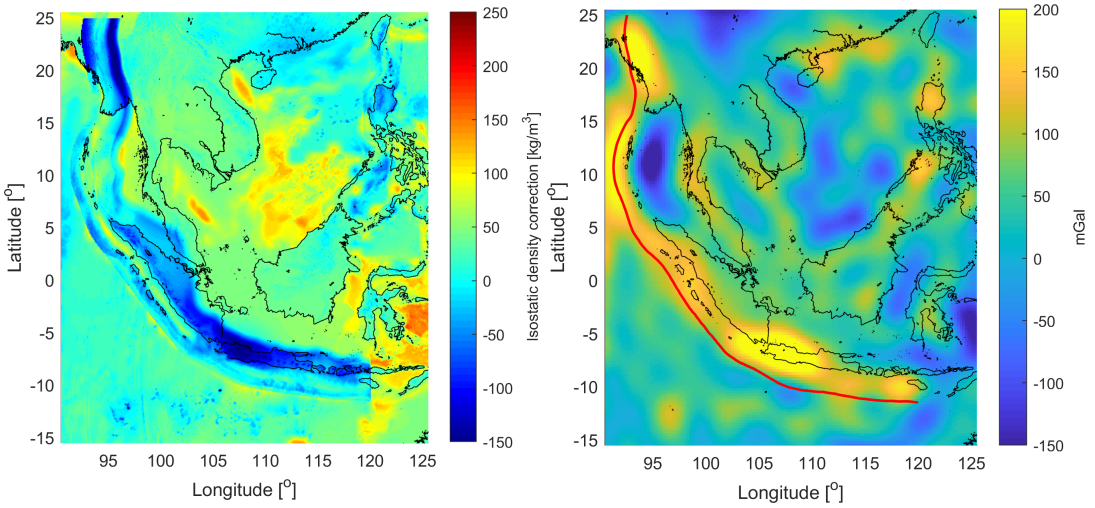

(a) ρ_{iso} for compensation depth = 600 km

(b) g_R for compensation depth = 100 km

(c) g_R for compensation depth = 300 km

(d) g_R for compensation depth = 600 km

Figure 6.33: Compensating sub-lithospheric layer, SHC=3-90

in XGM2016 will be used. The minimum, maximum, and average values for the different tests are summarized in Table 6.2.

For the first model, a slab tear is positioned at a latitude of 5°. The top-slab surface including a slab tear is shown in Figure 6.34a. North of the tear, the top-slab extends only down to 200 km, whereas south of the tear the full slab is modelled down to 600 km depth. The large positive g_R anomaly of the nominal model in the Andaman Sea, see Figure 6.14a, has decreased to weaker anomaly, see Figure 6.34c. The signal for Sumatra and Java remained the same.

For the second model, a slab tear at a latitude of 0° was tested. The positive anomaly extends less far north compared to the first slab tear model, see Figure 6.34d. Therefore, the positive slab anomaly corresponds better with the positive anomaly in XGM2016, which extends from Java to the middle of Sumatra.

The positive anomaly in XGM2016 was compared with the different slab segments that were tested in GST0. The XGM2016 anomaly is closely matched in location and shape by the signal of the 200-300 km slab segment. The third test will include only the 200-300 km slab segment, with a slab tear at a latitude of 0°, and no slab northward of the tear. The slab vertical thickness shows where the segment is positioned, see Figure 6.35a. Comparing Figure 6.35b with Figure 6.34b shows that the slab segment (∼30 mGal) does not have the same magnitude as the anomaly in XGM2016, which is about 100 mGal. The anomaly of the slab model is more smeared that the XGM2016 anomaly, which could result from the fact that the density contrasts are shallower than 200 km. GST0 showed that the gravity signal will become more smeared with increasing depth.

When assuming that the positive g_R anomaly in XGM2016 is caused by a subducting slab, the slab model with a slab tear at $\phi = 0°$ gives the best qualitative fit. The anomaly values for both models are in the same range of 100 mGal. The residual is given in Figure 6.39a.

6.3.3. GST9: Addition of subducting eclogite crust

As discussed in Section 3.4, the crust subducts together with the lithosphere. It is one of the most important contributors to the gravity anomalies in subduction zones (Fowler, 2005; Lowrie, 2007), therefore, its effects are investigated in this test. For this test the effects of isostatic compensation are not considered.

Shear heating by shear deformations on subduction zone interface results in a material phase change of the basalt crust. This basalt-eclogite phase change causes a density increase of 400 kg/m^3. Other literature gives a density estimate of 3560 kg/m^3 for the eclogite crust, assuming a nominal crust density between 2600 and 2900 kg/m^3 (Lowrie, 2007). Therefore, the range of uncertainty for the subducting crust density is between 3000 and 3560 kg/m^3. There is also no consensus on the maximum depth for the subducting crust, Fowler (2005) states a maximum depth of 80 km, whereas Lowrie (2007) assumes 150 km. The higher-density eclogite crust causes a significant gravity anomaly close to the trench. This addition feature to the slab model could allow for the modelling of the negative g_R anomaly following the trench in XGM2016, see Figure 6.34b. The case-study to fit a qualitative fit between signal of the slab model and the observations started in Subsection 6.3.2, will be continued for this test. The minimum, maximum, and average values for the different tests are summarized in Table 6.2, therefore, the counting of the tests is continued from GST8.

Four test are done for the subducting crust. The crust is modelled with a constant top-slab perpendicular thickness of 20 km. Figure 6.36a shows a cross-section for the slab model with the subducting crust, extending to a depth of 150 km. For the first test, an eclogite crust density of 3560 kg/m^3 results in a completely positive signal, see Figure 6.37a. The subducting signal (∼300 mGal) completely overpowers the nominal slab signal (∼140 mGal). Therefore, this model is not suitable to represent the negative-positive anomaly in XGM2016. To create the negative along-trench anomaly, the crust density should be lower than the lithospheric density (3300 kg/m^3). In the second test, the assumption is made that not enough shear heating is generated to bring about the basalt-eclogite transition, which can be related to the oblique subduction. Therefore, the subducting crust keeps its nominal density of 2900 kg/m^3. The g_R results are given in Figure 6.37b. Here, a negative-positive anomaly is visible. This configuration shows resemblance with the XGM2016 negative-positive anomaly for southern Sumatra and Java. The positive g_R anomaly comes from the slab, and the negative anomaly originates from

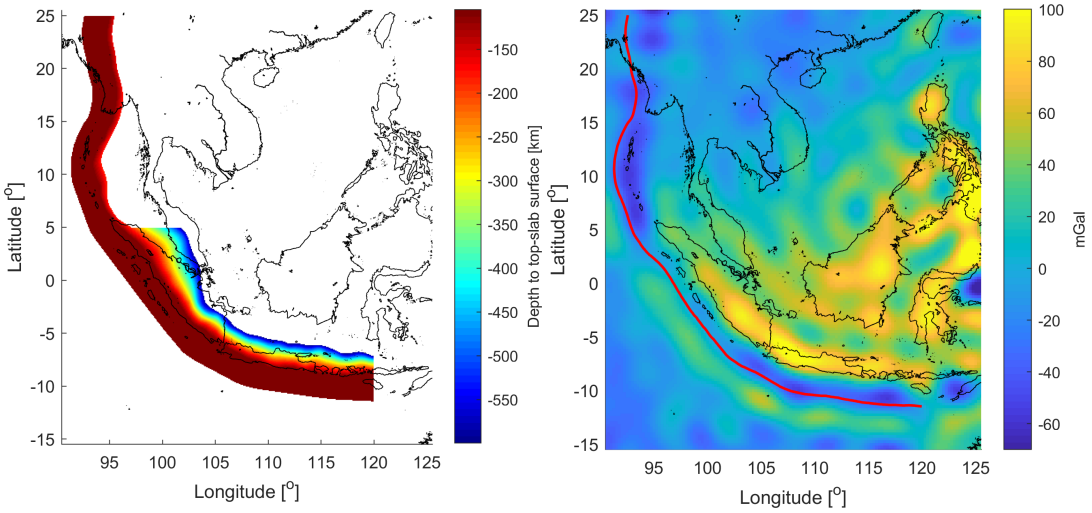

(a) Top-slab surface with tear at $\phi = 5°$

(b) g_R for XGM2016

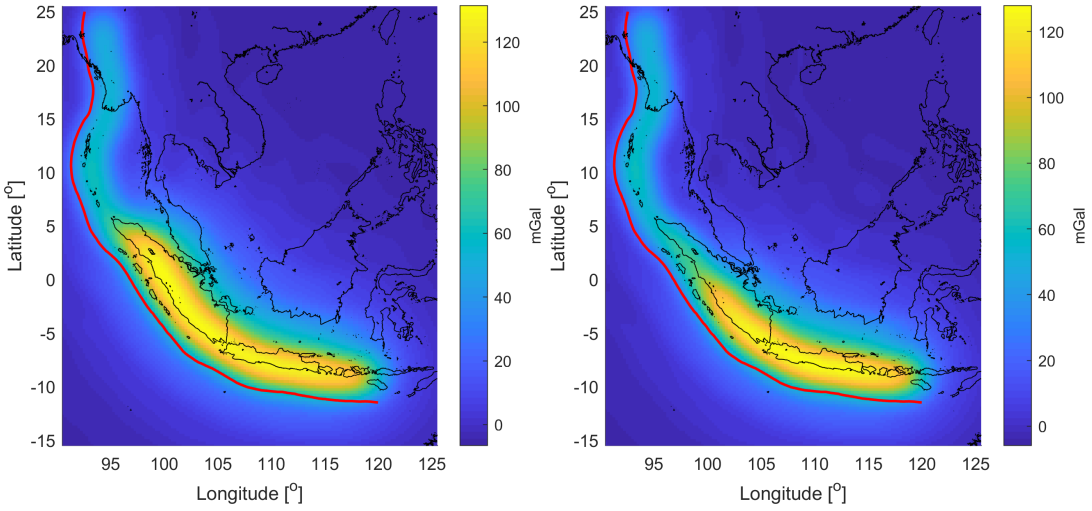

(c) g_R for slab model with tear at $\phi = 5°$

(d) g_R for slab model with tear at $\phi = 0°$

Figure 6.34: Slab models with tear, SHC=3-90

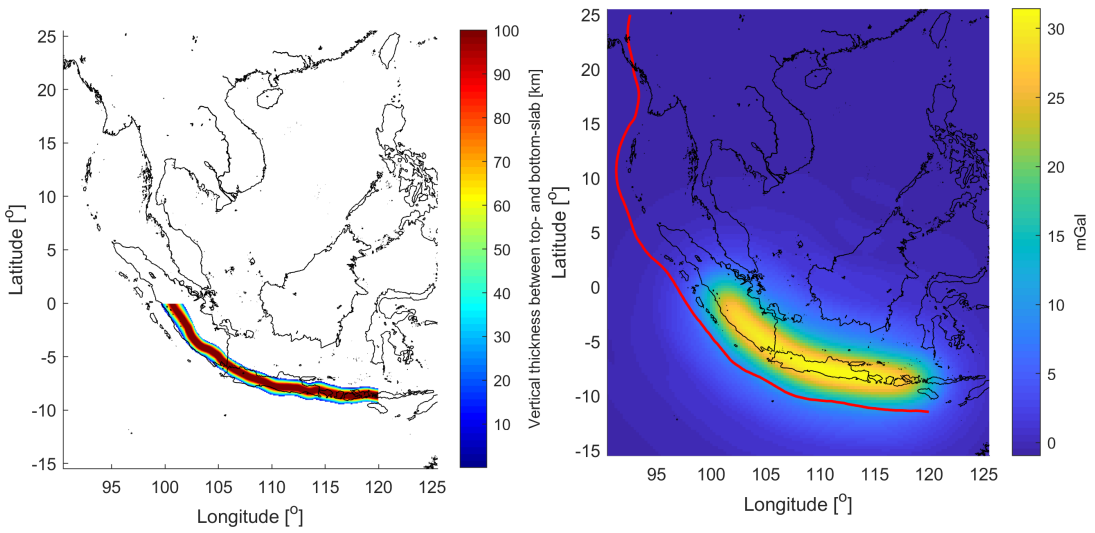

(a) Slab segment (200-300 km) with tear

(b) g_R for slab segment with tear

Figure 6.35: Slab segment (200-300 km) with tear at $\phi = 0°$, SHC=3-90

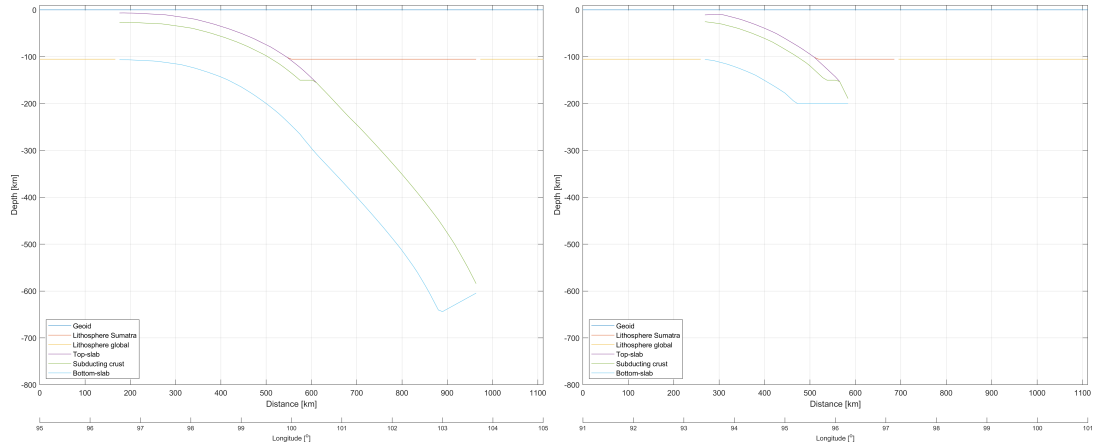

(a) Model at $\phi = 0°$

(b) Model with tear at $\phi = 18°$

Figure 6.36: Model cross-sections (West-East) (GST9)

the subducting crust. However, the negative anomaly has a much larger amplitude than observed in the observations, therefore, the crustal density needs to be increased. In the fifth and sixth test, the crustal density will be increased to 3100 kg/m^3, and the slab tear will be re-introduced at $\phi = 0^{/circ}$. This will allow for the along trench negative g_R anomaly in XGM2016 in the Andaman Sea to be represented by the subducting crust, without the positive anomaly from the slab. Figure 6.36b shows a slab cross-section northwards of the slab tear. The residual with the fifth text and XGM2016 is shown in Figure 6.39c. For the sixth test, the subducting slab will only down to 80 km. This is done to try to mitigate the positive residuals between northern Sumatra and the trench, see Figure 6.39c. This adjustment is partially effective, see residuals for the sixth test in Figure 6.39d, where the aforementioned residual has decreased.

6.3.4. Case-study: fit XGM2016 using slab tear (GST8) and subducting crust (GST9)

It is important to mention that this case-study only tries to show that the observation signal can be represented with a simple slab model, including a subducting crust and a slab tear. Recall from the introduction that additional constraints are crucial for the gravity modelling of subduction zones. However, the slab modelling for GST8 and GST9 has been done without additional constraints, and without

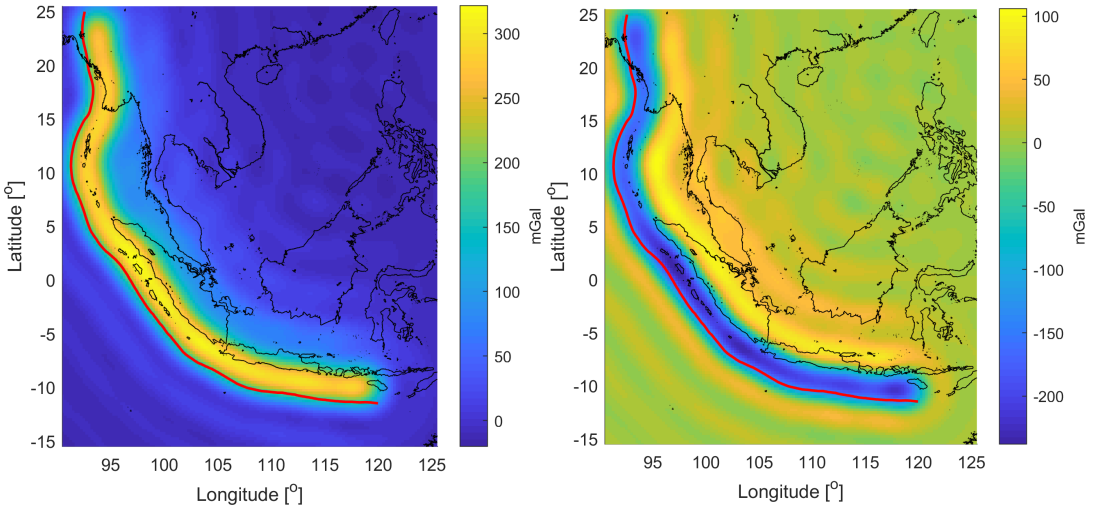

(a) $\rho_{crust} = 3560$ kg/m^3 (b) $\rho_{crust} = 2900$ kg/m^3

Figure 6.37: g_R for slab model with subducting crust with a depth of 150 km, SHC=3-90

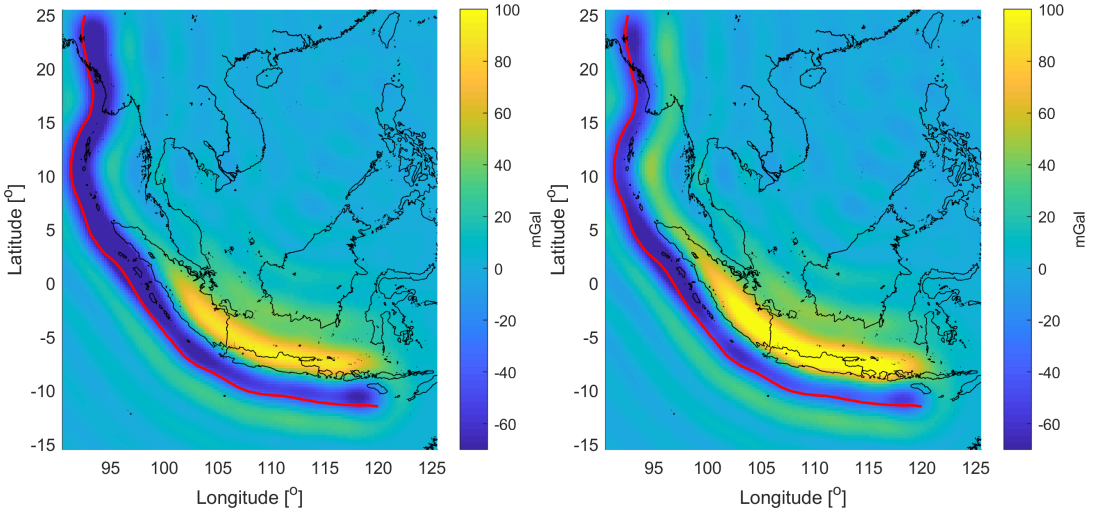

(a) Subducting crust down to 150 km (b) Subducting crust down to 80 km

Figure 6.38: g_R for model with tear and subducting crust, $\rho_{crust} = 3100$ kg/m^3, SHC=3-90

Table 6.2: Summary of residual benchmarks (min., max., avg.) between slab models (GST7, GST8) and XGM2016 within the Sumatra subduction zone, SHC=3-90

Test	Min. g_R [mGal]	Max. g_R [mGal]	Avg. g_R [mGal]
1. GST8: tear at $\phi = 5°$	-193.7	104.5	-8.5
2. GST8: tear at $\phi = 0°$	-193.1	106.6	**-6.6**
3. GST9: $\rho_{crust} = 3560$ kg/m^3, max. crust depth = 150 km	-398.0	79.7	-29.7
4. GST9: $\rho_{crust} = 2900$ kg/m^3, max. crust depth = 150 km	-118.1	260.9	14.3
5. GST9: $\rho_{crust} = 3100$ kg/m^3, tear at $\phi = 0°$, max. crust depth = 150 km	-83.6	160.2	6.8
6. GST9: $\rho_{crust} = 3100$ kg/m^3, tear at $\phi = 0°$, max. crust depth = 80 km	-115.5	123.5	**2.6**

considering isostasy. Therefore, the resulting models from the six different test cases are probably not realistic representations for the Sumatra subduction zone. This case-study serves as a starting point for further investigation.

The extreme values and averages of the g_R residuals are used as benchmarks to assess the theoretic fit of the models of GST8 and GST9 to XGM2016. Those benchmarks are only calculated within the Sumatra subduction zone. Table 6.2 shows that a subducting crust with either ρ_{crust}=2900 or 3560 kg/m^3 gives large ranges in residuals, in the order of 370 and 580 mGal. Moreover, it is seen that the decisions from test 3 to 6 each resulted in a decrease of the average residual. Moreover, Figure 6.39 also shows the increased fit with XGM2016 reflected in the decreasing residuals from test 2, 4 and 5 to test 6. This shows that making informed modelling adjustments can result in better fit with the observations. The sixth test has the lowest average residual of 2.6 mGal. This does not mean that this is the most realistic slab model, but it shows that this model has the best overall fit with XGM2016. The models that combine the slab tear and subducting crust, have the smallest ranges for the residuals, both in the order of 240 mGal. Concluding, modelling of the negative-positive along-trench anomalies in XGM2016 is best done using a subducting crust with a maximum depth of 80, crustal density of 3100 kg/m^3, and an East-West slab tear at $\phi = 0°$. The nominal slab is modelled southward of the tear, whereas north of the tear the slab only extends down to 200 km.

An average residual with observations of 2.6 mGal is good. However, a range of 240 mGal is very high. Including models for the topography, bathymetry, sediments, crust could resolve those high-frequency anomalies that are not related to the slab. For example, the positive residual in Figure 6.39d originates in crust. This is shown in Chapter 5. Although the results show good fit for a slab model with a tear, no definite conclusions can be made on the postulated slab.

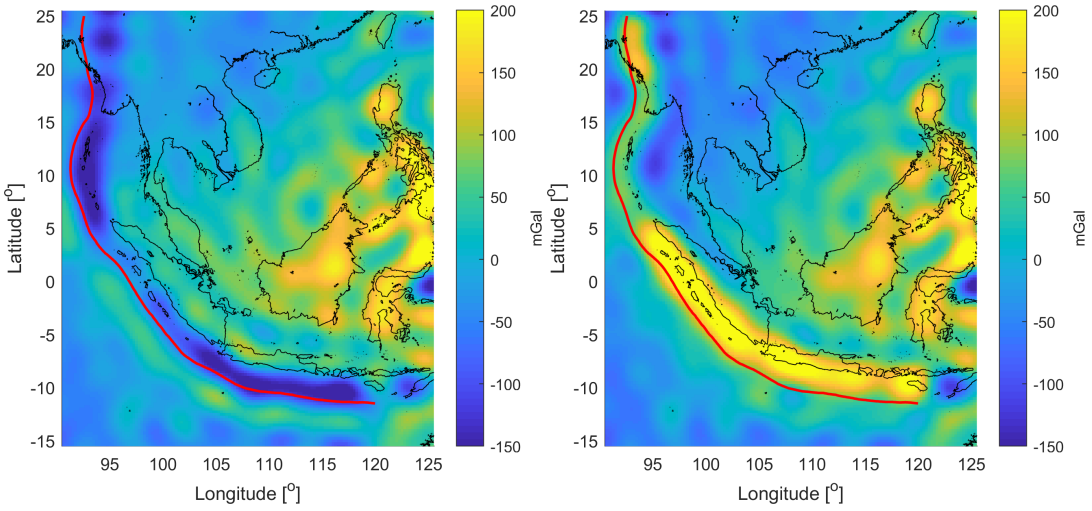

(a) 2. GST8: tear at $\phi = 0°$

(b) 4. GST9: $\rho_{crust} = 2900$ kg/m^3, max. crust depth = 150 km

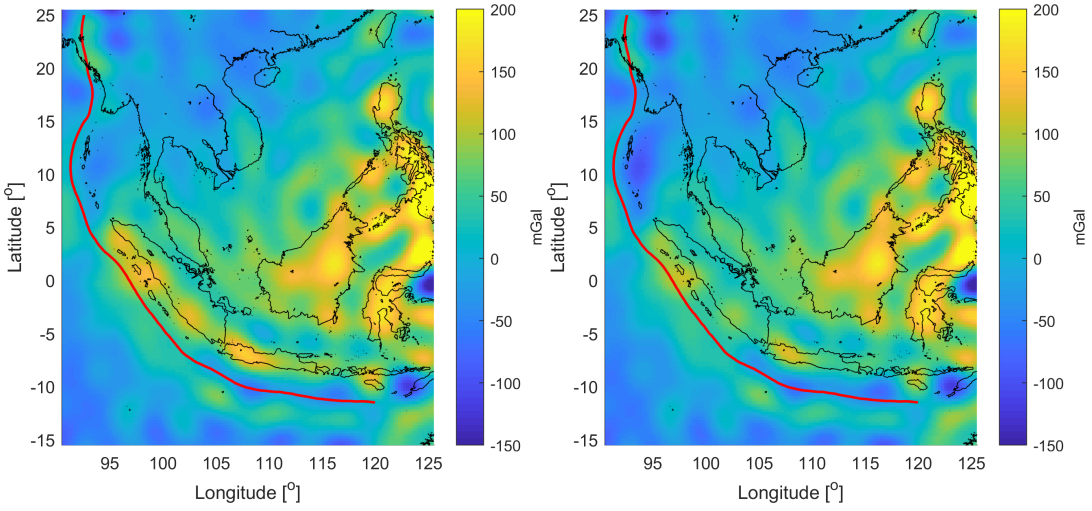

(c) 5. GST9: $\rho_{crust} = 3100$ kg/m^3, tear at $\phi = 0°$, max. crust depth = 150 km

(d) 6. GST9: $\rho_{crust} = 3100$ kg/m^3, tear at $\phi = 0°$, max. crust depth = 80 km

Figure 6.39: g_R residuals between slab models (GST8, GST9) and XGM2016, SHC=3-90

7

Conclusion

This conclusion will give the answers to the research questions and put the most important conclusions of this study in perspective with existing knowledge. In this thesis, gravity modelling of the subducting slab in the Sumatra subduction zone was studied. Subduction zones cause about 80% of all large earthquakes (Hayes and Wald, 2009). Subduction zone earthquakes occur on the interface between the overriding plate and the subducting slab. Modelling of subducting slabs is essential to better understand the causal mechanisms behind earthquakes. The top-slab geometry for the Sumatra subduction zone is known. However, earthquake prediction depends on dynamic modelling (e.g. FEM) (Gutknecht et al., 2012), for which a 3D slab geometry and density is required (Mansi et al., 2014). The 3D slab geometry and density can be obtained from gravity observations, when constraint with other data (Gutknecht et al., 2014; Bassett and Watts, 2015a). The gravity sensitivity to changes in slab geometry and density parameters were tested in this thesis.

Recent satellite missions, like GOCE, provided gravity and gravity gradient observation models with unprecedented resolution and homogeneous global coverage (Cadio et al., 2016). When combined with terrestrial gravity models, these can be used as additional constraints for 3D slab modelling. This thesis is the first time the Sumatra subduction zone is investigated using gravity gradients, and the first time that a gravity sensitivity study is done for a slab constrained by top-slab surface based on seismic and tomographic models. One other study on gravity sensitivities for subducting slabs was found (Krien and Fleitout, 2008). That study focused mainly on representing forces in theoretic subduction zones using geoid and radial gravity anomalies, and did not use either seismic or tomographic constraints. The research aim was to better understand the gravity signal coming from the subducting slab in the Sumatra subduction zone, starting from a top-slab surface (Broerse et al., 2015). This was done by modelling the subducting slab and investigating the gravity sensitivities to different individual slab model parameters and slab features. A spectral analysis identified the bandwidth in which most of the slab signal was present. Moreover, different isostatic compensation methods using Pratt's hypothesis were applied to the slab model.

My conclusions will assist future work on the Sumatra subduction zone, and subduction zones in general, to know which inputs are worthwhile to investigate and improve. The gravity signal of many subduction zones has been modelled using synthetic slab models. However, no study has been done relating the change in gravity with the change in slab parameters. In a physical sense, those sensitivities are not useful, as the slab parameters of a subduction zone are relatively constant over time, and therefore, no change in gravity signal will be observed for short time-scales. However, when using terrestrial and satellite gravimetry to constrain slab models, knowledge on those sensitivities is essential. Because those modelling methods all operate using degrees of freedom in the slab models, and some even include non-slab related parameters in the optimization to find a model that fits gravity observations.

This study was the first time that gravity gradient invariants were investigated for the Sumatra subduction zone. The second invariant (I_1) combines all the different gravity gradient components while being non-directional. The non-directionality attribute is useful for the modelling of the curved subduction zone of Sumatra. The research questions will be answered below.

What slab parameters and slab features need to be included to generate a simple slab model?

For a simple slab model, three slab parameters are required: slab maximum depth, slab thickness, and slab constant density. Seven additional features were added to create a more realistic simple slab model: density distribution, thickness distribution, ageing, isostatic compensation, slab tear, and a subducting crust. The remainder of this section will discuss the main conclusions with respect slab modelling.

Seismic and tomographic models provide accurate representations of top-slab surfaces (Hayes et al., 2012b). Therefore, a combined top-slab model was used as starting point for the simple slab model (Broerse et al., 2014). The used combined top-slab model is based on Slab1.0 (Hayes et al., 2012b), RUM (Gudmundsson and Sambridge, 1998) and UU-P07 (Amaru, 2007). Slab maximum depth, slab thickness, and slab constant density were sufficient to generate a simple slab model (Krien and Fleitout, 2008). Inclusion of a slab density distribution, a lithospheric age-based thickness distributions and accounting for slab ageing resulted in more realistic slab models (Müller et al., 2008; Jacob et al., 2014). Isostatic compensation was also added to the slab model. To control the regional gravity anomalies better, a slab tear and a subducting crust were added to the slab model.

Applying a vertical thickness to the top-slab surface would lead to inaccurate slab models. Considering the dip and strike-angles resulted in a bottom-slab surface with a thickness defined perpendicular to the top-slab surface. Delaunay triangulation was used for the 3D interpolation from slab contour lines to a meshed surface (Amidror, 2002). The *linear* method is best suited to obtain an accurate top-slab surface, while providing the benefit of being the most computationally efficient method. It was shown that the *nearest neighbour* method generated unacceptable errors, and should therefore not be used for slab interpolation.

A weighted HS using a thermal diffusivity of $1{\times}10^{-6}\ m^2/s$ resulted in the most accurate thickness-age distribution with respect to surface wave dispersion studies. The HS weighting factor comprises the depth parameters of the plate models PSM and GDH1, and introduces boundedness to the HS. The weighted HS was preferred over plate models, due to the simplicity of the mathematical description, while having a realistic asymptotic lithospheric thickness of 110 km. The weighted HS is only accurate for lithospheric ages above 10 Ma. Increasing the thermal diffusivity led to an increase in lithospheric thickness. It was concluded that decreasing the thermal diffusivity by $2{\times}10^{-7}$ m^2/s resulted in an overall decrease of 20 mGal for g_R. The effect of changing the thermal diffusivity on I_1 was not uniform.

Assuming a constant slab thickness was invalid assumption, oceanic lithospheric age data shows large age differences at the trench of the Sumatra subduction zone (Müller et al., 2008). Therefore, a trench age distribution was computed, which ranged from 40 Ma at northern Sumatra to 150 Ma south-east of Java. Converting to oceanic lithospheric thickness using the weighted HS, resulted in thicknesses ranging from 85 to 108 km. The younger lithosphere at northern Sumatra is lighter and therefore resists subduction, which was correlated to indentation of the trench at this location (Jacob et al., 2014).

The subducting slab does not have a constant thickness for the whole Sumatra subduction zone. Two methodologies were constructed to strive for a more realistic slab thickness distribution. Firstly, a simple methodology was tested utilizing the top slab contour lines together with scaling factors for the slab thickness at certain depths. However, this method provided no means to incorporate information on the subduction rate and direction, and was therefore neglected. A second more advanced method was constructed and used. This method accounted for slab ageing, using a constant subduction direction of 30° and a constant subduction rate of 55 km/Ma. Inclusion of slab ageing let to a maximum increment in slab thickness of 20 km at a depth of 600 km.

What is the optimal spherical harmonic bandwidth that isolates the slab model signal?

An advanced spectral analysis of a 3D slab model based on Slab1.0 showed that truncating the lower SHC limit is not favourable. Firstly, most of the slab signal (~45%) is present between SHC d/o 0 and 20. Secondly, to compensate for the loss of signal due to lower SHC limit truncation significant additional higher order SHC are required, which drastically decreased the computational efficiency of the synthesis. An optimal lower limit of d/o 3 was selected. A simple spectral analysis was done for the

combined slab model. The second invariant signal spans a wider SHC bandwidth, which corresponds to observations that the second invariant is more sensitivity to short-wavelength density anomalies closer to the surface. An optimal truncation setting of SHC=3-90 was determined, which results in 99% of the g_R signal and 80% of the I_1 signal to be present for the slab model. To obtain 99% of the I_1 slab signal, the upper limit needs to be increased to d/o 180. The optimal SHC bandwidth also provides a distinct slab signal in the observation dataset (XGM2016).

What are the qualitative and quantitative sensitivities of the radial gravity and second gravity gradient invariant to different slab parameters and slab features?

Ten slab parameters and slab features were investigated for their effect on the gravity signal. The outcome is a qualitative and quantitative summary on the gravity sensitivity to different slab parameters and slab features applicable to the Sumatra subduction zone. Slab parameters (depth, thickness, density) were best investigated using cross-sections, whereas slab features (ageing, isostatic compensation, slab tear, subducting crust) were analysed in-plane. The magnitude and location of extreme values for g_R and I_1, and the difference between cross-sections were proven to be useful metrics for gravity sensitivity analysis. GST0 to GST6 are discussed here, whereas GST7 to GST9 will be discussed when answering consecutive research questions.

The first test (GST0) investigated the gravity effect of slab segments at different depths. The deeper slab segments give a more long-wavelength signal which moves away from the trench with increasing depth. The extreme values for g_R and I_1 decrease with increasing segment depth. The slab between 0 and 300 km is responsible for 80% of the g_R signal, and 98% of the I_1 signal. Slab segments below 300 km depth have a negligible effect on the second invariant, as they are almost completely overpowered by the signal from segments closer to the surface. For the radial gravity component, the slab segments between 300-600 km still make up 20% of the total signal. Therefore, the sensitivity of g_R extends to at least a slab depth of 600 km. For this test, a density contrast of 50 kg/m^3 was used. Changing the density contrast does not influence the percentages discussed before. Only the absolute values of the gravity signal will be affected, but the relative signal from the different segments remains unchanged. This statement is validated in GST3. A linear relation was observed between segment's density contrast and g_R signal. When computing the radial gravity signal at GOCE altitude (225 km) assuming a noise level of 1 mGal, a density contrast of 5 kg/m^3 would be detectable down to 600 km depth. For segments between 0-100 and 100-200 km depth, the detectable density contrast is approximately 1 kg/m^3.

The second test (GST1) shows a shift of the g_R anomaly away from the trench for increasing slab depth, which is in line with the observations from the first test. The shift for the I_1 anomaly is negligible. A slab model providing a g_R accuracy of 1 mGal requires the slab depth to be known with a precision of 3.5 km for 200 km depth, and 9 km for 600 km depth, assuming a slab-mantle density contrast of 50 kg/m^3.

Varying the slab thickness (GST2) caused both the g_R and I_1 signal to move away from the trench. When changing the slab thickness from 20 to 60 km, the signal moves 60 km away from the trench for both g_R and I_1. Moreover, increasing the slab thickness results in a wider and larger amplitude g_R and I_1 signal, with the largest effect in the northern Sumatra and Andaman Sea regions. This is related to the shallower dip-angle for those regions, compared to the Burma or Java region. The thickness needs to be modelled with an accuracy of 0.7, 1.2 and 2 km for slab thicknesses of 20, 60 and 100 km to obtain a gravity error of 1 mGal. Changing the slab thickness (GST2) has a more profound effect on the magnitude of the gravity signal than changing the slab depth (GST1). On average, a 1 km increase in slab thickness causes the g_R signal to increase by 0.91 mGal, whereas a 1 km increase in slab depth will only produce a 0.19 mGal increase. For I_1, the slab thickness also has larger effect than the slab depth.

Changing the slab constant density does not affect the location of the signal's maximum amplitude (GST3). Three interesting observation were made for a slab with constant density. Firstly, the g_R peak can be used to locate the intersection between the top-slab and the lithosphere. This is true anywhere in the Sumatra subduction zone, except in the Burmese region. This characteristic might be useful for identifying the location of the mantle wedge or estimating the continental lithospheric thickness. Secondly, the I_1 peak can be used to located where the slab base is at 200 km depth. This characteristic was consistent for the whole Sumatra subduction zone. Thirdly, the difference in position

between the peaks of g_R and I_1 can be used to estimate the dip-angle, where large differences in peak positions were found for shallow dip-angles, and steep dip-angles were observed together with small differences in peak position. Adding a density distribution to the slab (GST4), showed that steeper linear gradients in the density distribution only caused the amplitude of the signal to increase. This implied that the gravity-depth effect cannot be cancelled using linear gradients.

Accounting for the oblique convergence in the Sumatra subduction zone, two slab thickness distributions were constructed based on subduction direction and rate. For the first thickness distribution slab ageing was neglected. This distribution adds a negative anomaly of approximately -19 mGal at northern Sumatra, and a more long-wavelength positive anomaly of 10 mGal south of Java. Incorporating lithospheric ageing when modelling the slab thickness (GST6) impacted the gravity signal for the middle and northern Sumatra region the most. Moreover, a large increment in slab thickness and therefore gravity signal was observed under coastal region of Thailand, due to its large distance with respect to the trench and therefore large ageing effect. Incorporating ageing resulted in an additional signal of 6 mGal in northern Sumatra compared to the non-ageing case (GST5).

What isostatic compensation method yields the most realistic compensation density values and provides a realistic gravity signal?

A compensating lithosphere together with a compensation depth of 300 km is best suited to compensate the subducting slab. The minimum isostatic density values in the subduction zone are in the range of -150 kg/m^3. Increasing the compensation depth beyond 300 km results in overcompensation of the slab. When extending the compensation depth down to 600 km, the positive mass anomaly of the slab result in a negative gravity anomaly. Overcompensation is a term that is introduced to describe the situation where a mass anomaly results in a gravity anomaly of opposite sign. The sub-lithospheric layer is not suitable for the compensation of shallow mass anomalies. However, the sub-lithospheric layer is the most effective layer for compensating the slab, especially at a compensation depth of 600 km. Isostatic equilibrium for shallow masses is best achieved with a compensating crust, at the cost of overcompensating the slab. Unrealistic isostatic densities were computed for the crust, in the range of -400 to 600 kg/m^3. Therefore, this compensation type should only be investigated for much shallower compensation depths than 100 km.

Can a simple slab model incorporating the different slab parameters and features explain the corresponding gravity anomalies in XGM2016?

A simple slab model including a subducting crust together with a slab tear was able to produce a first-order fit with XGM2016. An average residual of 2.6 mGal was achieved after several iterations of the crustal density and the maximum depth of the subducting slab. An eclogite crust of 2900 or 3560 kg/m^3 resulted in very large residuals. The lowest residual of 2.6 mGal was obtained for model with a subducting crust of 3100 kg/m^3 extending down to 80 km, and a slab tear located approximately at the volcanic centre of Toba (Hall and Spakman, 2015). However, those results cannot be used to provide evidence for either slab tear or window, as no additional constraints were used. Additional Earth models should be incorporated for a more detailed assessment of the presence of a slab tear in the Sumatra subduction zone.

8

Recommendations

With respect to presented thesis work, some recommendations are given for the continuation of this thesis' research, and hopefully, future new work. The recommendations are divided into two categories: improvements for slab modelling, and recommendations for future gravity sensitivity studies.

8.1. Improvements on slab modelling

In GST0 and GST1 it was concluded that the gravity signal originating from shallow parts of the slab is much stronger than for the deeper slab. Therefore, it is hard to distinguish the signal for deep slab segments when modelling the full slab. Those deeper slab segments are of special interesting for gravity modelling, as seismic and tomographic data is of low-resolution, scarce or unavailable at deeper depths. Beneath southern Sumatra earthquake epicentres are traced down to depths of 500 km. For northern Sumatra and more north-west regions (Andaman, Burma) very scarce seismic data is available deeper than 300 km. Therefore, it is recommended to investigate the deeper parts of the slab separately from the shallow parts. First, a separate spectral analysis should be done for the shallow and deeper slab segments. Secondly, the shallow and deep slab-related signal should be independently extracted from gravity observations. Thirdly, efforts should be made to find a slab geometry corresponding with gravity observations, while keeping the slab model constrained with other datasets. An outcome of such as analysis could be that there is no slab in regions with scarce or no seismicity, which would also be a significant scientific contribution to the discussion if there is a slab in the Andaman Sea.

In GST3 and GST4, the gravity sensitivity with respect to different slab density distribution was tested. However, those distributions are over-simplifications of the complex density structures that are present the subducting slab. More sophisticated density models need to be constructed. Usage could be made of the density-pressure and temperature-pressure gradients. Different density distributions have been identified that might be useful as a starting point: PEM-O, AK135-F, PREM500, and STW105. Those are all density distributions for oceanic lithosphere.

It is recommended adding additional subduction zone characteristics in the slab modelling. Subduction zones have several distinguished surface features, a deep oceanic trench, an accretionary wedge, a fore-arc basin and a volcanic arc on the overriding continental plate. In thesis, the trench, fore-arc basin and volcanic arc were modelled using external models (ETOPO1). The accretionary wedge is an important feature of the Sumatra subduction zone (Franke et al., 2008; McNeill and Henstock, 2014; Bassett and Watts, 2015b; Yadav, 2017), however, it has not been included yet in the slab model. Moreover, Hall and Spakman (2015) modelled a slab window under east Java, and different studies anticipate a slab window or slab tear under Burma (Fauzi et al., 1996; Huang and Zhao, 2006; Li et al., 2008; Burke, 2006; Pesicek et al., 2010). It is recommended to extend the slab modelling algorithm to include an accretionary wedge and slab window, and to perform corresponding gravity sensitivity studies. Doing so will result in a more realistic slab model for the Sumatra subduction zone.

As was stated in the introduction, forces within subduction zones create a dynamic gravity signal that cannot be translated into density contrasts. In subduction zones, a significant part of the gravity ob-

servations comes from the dynamic signal (Bassett and Watts, 2015a). Before comparing the gravity signal of Earth models with gravity observations the dynamic signal should be removed. Therefore, it is recommended to investigate how this dynamic signal can be estimated for the Sumatra subduction zone.

8.2. Recommendations for future gravity sensitivity studies

The gravity sensitivity tests were all done using slab models that were based on the same combined top-slab model (Broerse et al., 2014). This combined model has low quality for some regions, especially in the Andaman Sea. It would be useful to test the sensitivities for different top-slab parameters as well. Top-slab parameters that could be investigated are: strike-angle, dip-angle and depth. When trying to minimize the model residuals with observations, the top-slab should also be a degree-of-freedom in the slab modelling algorithm. This could potentially increase the quality of top-slab model in regions with large uncertainties. When doing so, it is important to stay within the uncertainty of the top-slab depth estimation (Hayes et al., 2012b).

It is recommended to create an overview of all the uncertainties in the input models and quantify the corresponding uncertainty in the gravity signal (g_R, I_1). This should be done for the depth and density data of topography, bathymetry, sediments, crust, lithosphere, top-slab, asthenosphere, and mantle. When trying to fit the model's signal to gravity observations, those uncertainties could be used as ranges to find better parameters for either layer depths or densities. However, one should not use an excessive amount of degrees-of-freedom in Earth modelling. It is recommended to vary parameters for input models that have the highest uncertainty, and accurate input models fixed. Crust, LAB and sediment models are known to have large uncertainties (Mooney and Kaban, 2010; Root et al., 2017).

A

Understanding gravity, gravity gradients, and invariants

Understanding the interplay between the three gravity components, the six gravity gradient components, and the two invariant components is difficult. To increase understanding, N-S cross-sections are made through the gravity observations dataset (XGM2016) at the dashed red line in Figure A.1. The observations are forward modelled between SHC d/o 3 and 90. The cross-sectional gravity results are given in Figure A.2, where the red and green line show the locations of the South and North coast of Java, respectively.

A few quick observations:

1. Moving along the x-axis means moving in positive Y-direction, therefore, the steep down-going gradient at g_X coincides with the peak in T_{XY}.
2. The signal of g_Z, T_{ZZ}, and I_0 are very similar
3. The peak of g_Z coincides with T_{ZZ}, which makes sense. The peak in g_Z is probably caused by a positive mass anomaly, above a large positive mass anomaly g_Z will increase more rapidly moving towards the mass anomaly than for a small mass anomaly, moving towards the mass anomaly is along the Z-axis, and therefore the T_{ZZ} is also larger

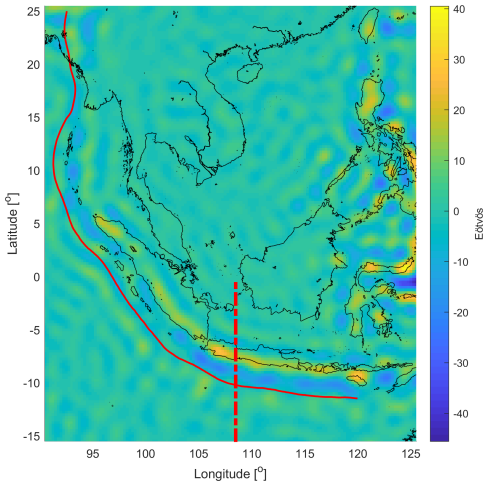

Figure A.1: T_{RR} for XGM2016 showing cross-section using red dashed line, SHC=3-90

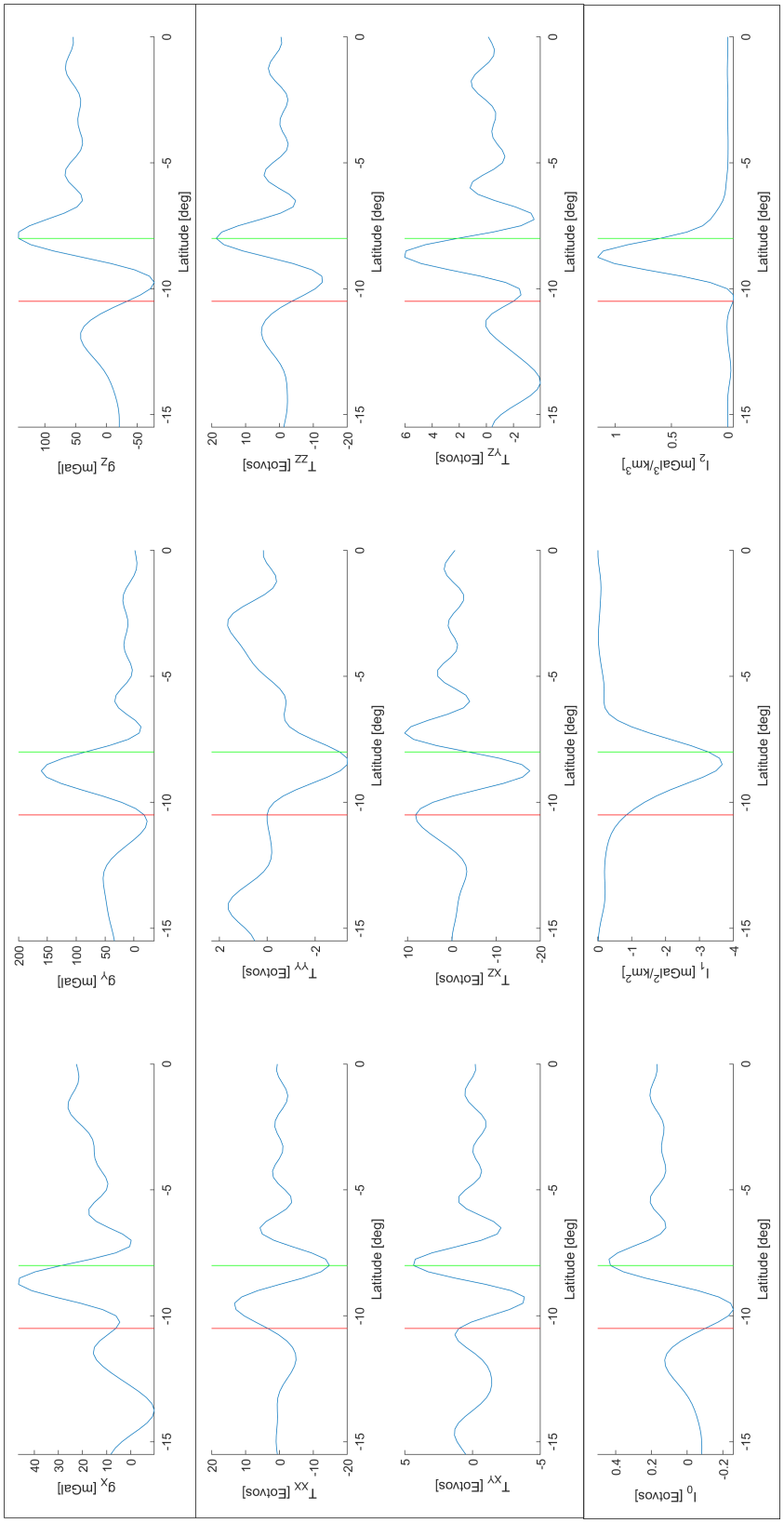

Figure A.2: Cross-sectional results for XGM2016, red and green line correspond to South and North coast of Java, SHC=3-90

B

Density for oceanic lithosphere

Different models for the 1D density distribution for the oceanic lithosphere can be used:

- **Oceanic Parametric Earth Model (PEM-O):** 1D density distribution for the oceanic upper mantle, below 420 km this model is identical to the continental model (PEM-C) (Dziewonski et al., 1975)
- **AK135-F:** a variant of the ak135 velocity model (Kennett et al., 1995), which is obtained by augmenting it with the density and Q (quality factor) model of Montagner and Kennett (1996). Upper mantle properties should be treated with caution, because the negative density gradient around 220 km might be an model artefact, see Figure B.1, where the AK135-Q deviates from baseline models IASP-Q and SP6-Q between 220 and 440 km
- **Modified Preliminary Reference Earth Model (PREM500):** average Earth model that incorporates anelastic dispersion and anisotropy and therefore it is frequency-dependent and transversely isotropic for the upper mantle, based on PREM (Dziewonski and Anderson, 1981; Panning and Romanowicz, 2006)
- **Reference Earth Model (STW105/REF):** transversely isotropic reference Earth model based on PEM (Dziewonski et al., 1975; Kustowski et al., 2008)

The different density models were interpolated to fit the user-defined slab segmentation, which resulted in the 1D density distributions given in Figure B.2.

There are two important phase changes in the lithosphere, which result in a significant density increase. The olivine-spinel phase change is an exothermic phase change, which increases the density between ~6-10% (~300 kg/m^3) at 410 km depth. The spinel-postspinel phase change is endothermic, and increases the density by ~8-10% (~220 kg/m^3) at a depth of 660 km. For subduction zones the spinel-olivine phase change occurs at a shallower depth of 325 km , and the spinel-postspinel phase change occurs a deeper depth of 700 km (Stern, 2002; Fowler, 2005). Thirdly, the subduction also causes the crust to change from basalt to eclogite due to shear heating. Shear heating is caused by shear deformations between continental and oceanic plates and the corresponding frictional heating (Lowrie, 2007). This basalt-eclogite phase change results in a much heavier subducting crust between 30 and 90 km, with an increased crustal density of 400 kg/m^3 (Fowler, 2005). Those differences in depth for the olivine-spinel and spinel-postspinel phase changes in subduction zones could be used to construct a realistic density distribution for the subduction zone, based on a nominal oceanic lithosphere. Combining this knowledge with the given density distributions, might be innovative way of modelling the slab density distribution.

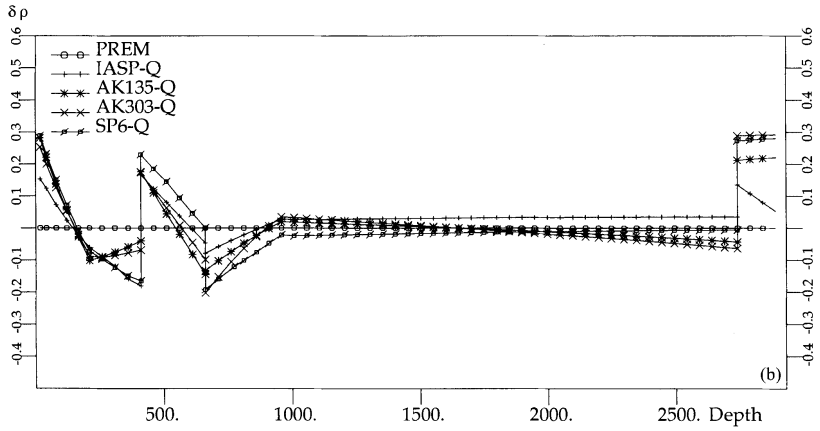

Figure B.1: 1D density model perturbations with respect to PREM (Montagner and Kennett, 1996, Fig. 4)

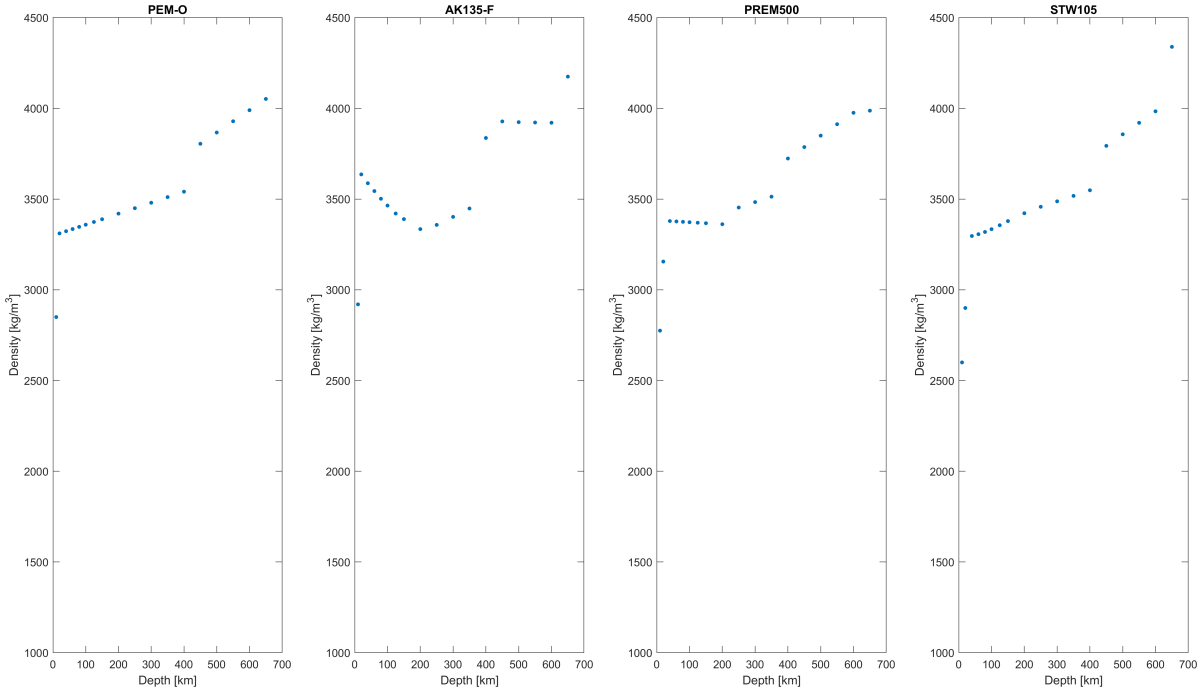

Figure B.2: Different 1D Earth density distributions interpolated for slab modelling: PEM-O (Dziewonski et al., 1975), AK135-F (Montagner and Kennett, 1996), PREM500 (Panning and Romanowicz, 2006), STW105 (Kustowski et al., 2008)

C

Poster - European Geosciences Union

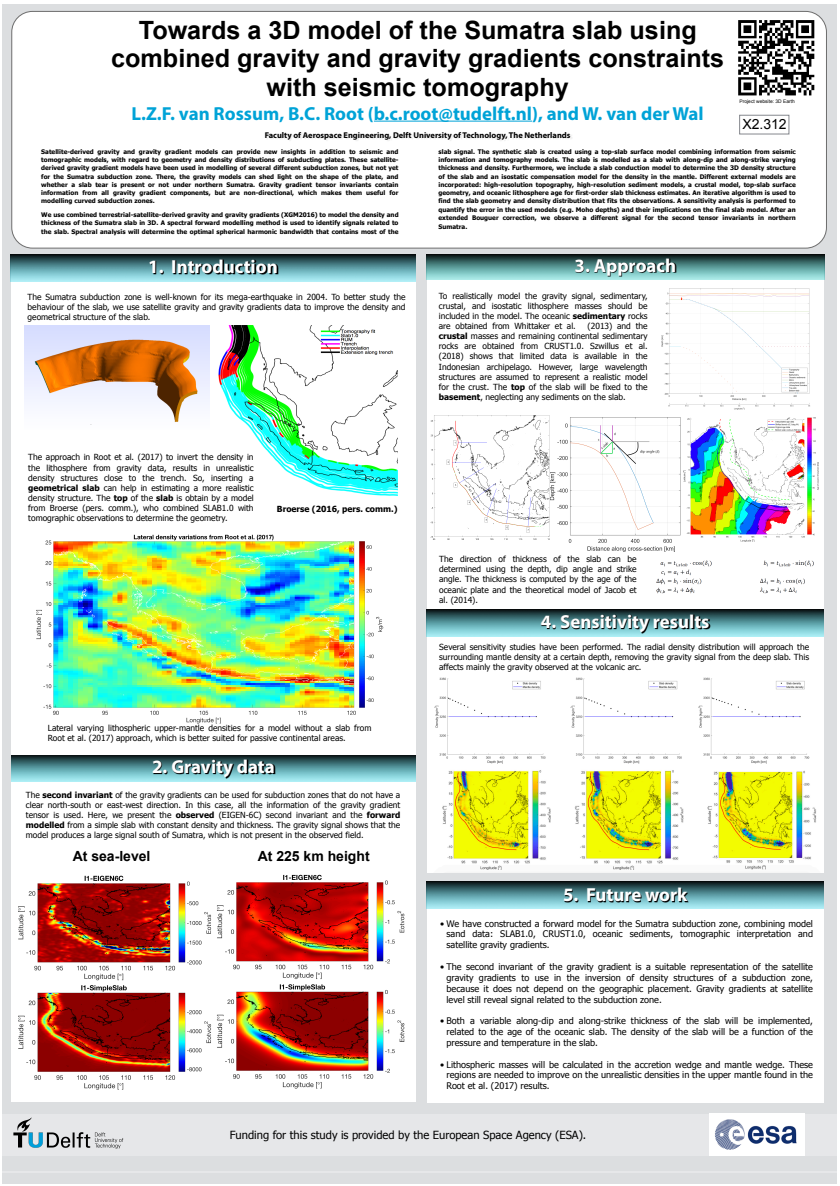

Figure C.1: Poster presentation at EGU General Assembly 2018 (Van Rossum et al., 2018)

Bibliography

Alvarez, O., M. Gimenez, C. Braitenberg, A. Folguera, A. Ramos, D. Poiré, E. Baldo, J. Dahlquist, and C. Rapela
2012. GOCE satellite derived gravity and gravity gradient corrected for topographic effect in the South Central Andes region. *Geophysical Journal International*, 190(2):941–959.

Alvarez, O., M. Gimenez, A. Folguera, S. Spagnotto, E. Bustos, W. Baez, C. Braitenberg, M. Gimenez, A. Folguera, S. Spagnotto, E. Bustos, W. Baez, and C. Braitenberg
2015. New evidence about the subduction of the Copiapó ridge beneath South America, and its connection with the Chilean-Pampean flat slab, tracked by satellite GOCE and EGM2008 models. *Journal of Geodynamics*, 91:65–88.

Amante, C. and B. W. Eakins
2009. ETOPO1 1 Arc-Minute Global Relief Model: Procedures, Data Sources and Analysis. *NOAA Technical Memorandum*, 24(March):19.

Amaru, M. L.
2007. *Global travel time tomography with 3-D reference models*. Doctoral dissertation, Utrecht University.

Amidror, I.
2002. Scattered data interpolation methods for electronic imaging systems: a survey. *Journal of Electronic Imaging*, 11(2):157.

Balmino, G., K. Lambeck, and W. M. Kaula
1973. A spherical harmonic analysis of the Earth's topography. *Journal of Geophysical Research*, 78(2):478–481.

Barthelmes, F.
2013. Definition of Functionals of the Geopotential and their calculation from Spherical Harmonic Models: Theory and formulas used by the calculation service of the International Centre for Global Earth Models (ICGEM). Technical report, GFZ German Research Centre for Geosciences, Potsdam.

Barthelmes, F. and W. Köhler
2016. International Centre for Global Earth Models (ICGEM). In *The Geodesist's Handbook 2016*, H. Drewes, F. Kuglitsch, J. Adám, and S. Rózsa, eds., volume 90, Pp. 907–1205. Journal of Geodesy (2016).

Bassett, D. and A. B. Watts
2015a. Gravity anomalies, crustal structure, and seismicity at subduction zones: 1. Seafloor roughness and subducting relief. *Geochemistry Geophysics Geosystems*, 16:1541–1576.

Bassett, D. and A. B. Watts
2015b. Gravity anomalies, crustal structure, and seismicity at subduction zones: 2. Interrelationships between fore-arc structure and seismogenic behavior. *Geochemistry Geophysics Geosystems*, 16:1541–1576.

Beiki, M. and L. B. Pedersen
2010. Eigenvector analysis of gravity gradient tensor to locate geologic bodies. *Geophysics*, 75(6):I37–I49.

Bouman, J., J. Ebbing, and M. Fuchs
2013. Reference frame transformation of satellite gravity gradients and topographic mass reduction. *Journal of Geophysical Research: Solid Earth*, 118(2):759–774.

Brackenridge, J. B., I. B. Cohen, and A. Whitman
2000. *Isaac Newton - The Principia: Mathematical Principles of Natural Philosophy (1726)*, volume 33, 3rd edition. Berkeley: University of California Press.

Braitenberg, C., P. Mariani, J. Ebbing, and M. Sprlak
2011. The enigmatic Chad lineament revisited with global gravity and gravity-gradient fields. *Geological Society, London, Special Publications*, 357(1):329–341.

Brocher, T. M.
2005. Empirical relations between elastic wavespeeds and density in the Earth's crust. *Bulletin of the Seismological Society of America*, 95(6):2081–2092.

Broerse, T., R. Govers, and R. Riva
2014. Lateral rheological variability in southeast Asia: combining gravity and GPS after the 2004 Sumatra megathrust event.

Broerse, T., R. Riva, W. Simons, R. Govers, and L. L. A. Vermeersen
2015. Postseismic GRACE and GPS observations indicate a rheology contrast above and below the Sumatra slab. *Journal of Geophysical Research B: Solid Earth*, 120(7):5343–5361.

Burke, K.
2006. Sumatra: Geology, resources and tectonic evolution. *Journal of Asian Earth Sciences*, 28(4-6):480.

Cadio, C., A. Saraswati, R. Cattin, S. Mazzotti, H. C. Berg, M. Mandea, R. L. Wesson, and G. Ekstrom
2016. A new approach to assess isostatic compensation of topography in continental domain from GOCE gravity gradients. *Geophysical Journal International*, 207(2):645–654.

Capitanio, F. A., A. Replumaz, and N. Riel
2015. Reconciling subduction dynamics during Tethys closure with large-scale Asian tectonics: Insights from numerical modeling. *Geochemistry, Geophysics, Geosystems*, 16(3):962–982.

Chesner, C. A.
1998. Petrogenesis of the Toba Tuffs, Sumatra, Indonesia. *Journal of Petrology*, 39(3):397–438.

Chesner, C. A.
2012. The Toba Caldera Complex. *Quaternary International*, 258:5–18.

Cloos, M.
1993. Lithospheric buoyancy and collisional orogenesis: Subduction of oceanic plateaus, continental margins, island arcs, spreading ridges, and seamounts. *Geological Society of America Bulletin*, 105(6):715.

Davies, G. F.
1981. Regional compensation of subducted lithosphere: effects on geoid, gravity and topography from a preliminary model. *Earth and Planetary Science Letters*, 54(3):431–441.

Divins, D. L.
2003. *Total Sediment Thickness of the World's Oceans and Marginal Seas*. Boulder, CO: NOAA National Geophysical Data Center.

Dziewonski, A. M. and D. L. Anderson
1981. Preliminary reference Earth model. *Physics of the Earth and Planetary Interiors*, 25(4):297–356.

Dziewonski, A. M., A. L. Hales, and E. R. Lapwood
1975. Parametrically simple earth models consistent with geophysical data. *Physics of the Earth and Planetary Interiors*, 10(1):12–48.

Engdahl, E. R., A. Villasenor, H. R. DeShon, and C. H. Thurber
2007. Teleseismic Relocation and Assessment of Seismicity (1918-2005) in the Region of the 2004 Mw 9.0 Sumatra-Andaman and 2005 Mw 8.6 Nias Island Great Earthquakes. *Bulletin of the Seismological Society of America*, 97(1A):S43–S61.

Fauzi, R. McCaffrey, D. Wark, Sunaryo, and P. Y. Prih Haryadi
1996. Lateral variation in slab orientation beneath Toba Caldera, northern Sumatra. *Geophysical Research Letters*, 23(5):443–446.

Fecher, T., R. Pail, and T. Gruber
2016. The combined satellite gravity field model GOCO05c. In *EGU General Assembly 2016 Geophysical Research Abstracts*, Vienna. Institute of Astronomical and Physical Geodesy, Technical University of Munich.

Floberghagen, R., M. Fehringer, D. Lamarre, D. Muzi, B. Frommknecht, C. Steiger, J. Piñeiro, and A. da Costa
2011. Mission design, operation and exploitation of the gravity field and steady-state ocean circulation explorer mission. *Journal of Geodesy*, 85(11):749–758.

Forsyth, D. and S. Uyeda
1975. On the Relative Importance of the Driving Forces of Plate Motion. *Geophysical Journal International*, 43(1):163–200.

Fowler, C. M. R.
2005. *The Solid Earth: An Introduction to Global Geophysics*, volume 10, 2nd edition. New York: Cambridge University Press.

Franke, D., M. Schnabel, S. Ladage, D. R. Tappin, S. Neben, Y. S. Djajadihardja, C. Müller, H. Kopp, and C. Gaedicke
2008. The great Sumatra-Andaman earthquakes - Imaging the boundary between the ruptures of the great 2004 and 2005 earthquakes. *Earth and Planetary Science Letters*, 269(1-2):118–130.

Goes, S., R. Agrusta, J. Van Hunen, and F. Garel
2017. Subduction-transition zone interaction: A review. *Geosphere*, 13(3).

Grevemeyer, I. and V. M. Tiwari
2006. Overriding plate controls spatial distribution of megathrust earthquakes in the Sunda-Andaman subduction zone. *Earth and Planetary Science Letters*, 251(3-4):199–208.

Gudmundsson, Ó. and M. Sambridge
1998. A regionalized upper mantle (RUM) seismic model. *Journal of Geophysical Research: Solid Earth*, 103(B4):7121–7136.

Gutknecht, B. D., H. J. Götze, T. Jahr, G. Jentzsch, R. Mahatsente, and S. Zeumann
2014. Structure and State of Stress of the Chilean Subduction Zone from Terrestrial and Satellite-Derived Gravity and Gravity Gradient Data. *Surveys in Geophysics*, 35(6):1417–1440.

Gutknecht, B. D., H. J. Götze, N. Köther, O. Lücke, and R. Mahatsente
2012. Poster presentation: Sensitivity of GOCE along the Andean subduction zone. In *GOCE Solid Earth Workshop*, Enschede. Institute of Geosciences, Christian-Albrechts-Universität Kiel.

Hall, R. and W. Spakman
2015. Mantle structure and tectonic history of SE Asia. *Tectonophysics*, 658:14–45.

Hamza, V. M. and F. P. Vieira
2012. Global distribution of the lithosphere-asthenosphere boundary: A new look. *Solid Earth*, 3(2):199–212.

Hayes, G. P., M. Bernardino, F. Dannemann, G. Smoczyk, R. Briggs, H. M. Benz, K. P. Furlong, and A. Villaseñor
2013. Seismicity of The Earth 1900–2012 Sumatra and Vicinity. *U.S. Geological Survey Open-File Report*, 2010(1083-L):1.

Hayes, G. P. and D. J. Wald
2009. Developing framework to constrain the geometry of the seismic rupture plane on subduction interfaces a priori - A probabilistic approach. *Geophysical Journal International*, 176(3):951–964.

Hayes, G. P., D. J. Wald, and R. L. Johnson
2012a. Online portal for Slab1.0: A three-dimensional model of global subduction zone geometries.

Hayes, G. P., D. J. Wald, and R. L. Johnson
2012b. Slab1.0: A three-dimensional model of global subduction zone geometries. *Journal of Geophysical Research: Solid Earth*, 117(1):1–15.

Hosse, M., R. Pail, M. Horwath, N. Holzrichter, and B. D. Gutknecht
2014. Combined Regional Gravity Model of the Andean Convergent Subduction Zone and Its Application to Crustal Density Modelling in Active Plate Margins. *Surveys in Geophysics*, 35(6):1393–1415.

Huang, J. and D. Zhao
2006. High-resolution mantle tomography of China and surrounding regions. *Journal of Geophysical Research: Solid Earth*, 111(9):1–21.

ICGEM
2017. ICGEM Service Frequently Asked Questions (FAQs). Technical report, Helmholtz Centre Potsdam, GFZ German Research Centre for Geosciences, Potsdam.

Jacob, J., J. Dyment, and V. Yatheesh
2014. Revisiting the structure, age, and evolution of the Wharton Basin to better understand subduction under Indonesia. *Journal of Geophysical Research: Solid Earth*, 119(1):169–190.

Kaban, M. K., P. Schwintzer, and C. Reigber
2004. A new isostatic model of the lithosphere and gravity field. *Journal of Geodesy*, 78(6):368–385.

Kaban, M. K., M. Tesauro, and S. Cloetingh
2010. An integrated gravity model for Europe's crust and upper mantle. *Earth and Planetary Science Letters*, 296(3-4):195–209.

Kennett, B. L. N., E. R. Engdahl, and R. Buland
1995. Constraints on seismic velocities in the Earth from traveltimes. *Geophysical Journal International*, 122(1):108–124.

Kirby, S. H., S. Stein, E. A. Okal, and D. C. Rubie
1996. Metastable mantle phase transformations and deep earthquakes in subducting oceanic lithosphere. *Reviews of Geophysics*, 34(2):261–306.

Klokočník, J., J. Kalvoda, J. Kostelecký, and A. Bezděk
2014. Gravity Disturbances, Marussi Tensor, Invariants and Other Functions of the Geopotential Represented by EGM 2008. *Journal of Earth Science Research*, 2(3):88–101.

Kopp, H.
2002. Crustal structure of the Java margin from seismic wide-angle and multichannel reflection data. *Journal of Geophysical Research*, 107(B2):2156–2202.

Kopp, H., E. R. Flueh, D. Klaeschen, J. Bialas, and C. Reichert
2001. Crustal structure of the Central Sunda margin at the onset of oblique subduction. *Geophysical Journal International*, 147(2):449–474.

Köther, N., H. J. Götze, B. D. Gutknecht, T. Jahr, G. Jentzsch, O. H. Lücke, R. Mahatsente, R. Sharma, and S. Zeumann
2012. The seismically active Andean and Central American margins: Can satellite gravity map lithospheric structures? *Journal of Geodynamics*, 59-60:207–218.

Krien, Y. and L. Fleitout
2008. Gravity above subduction zones and forces controlling plate motions. *Journal of Geophysical Research: Solid Earth*, 113(9):1–20.

Kustowski, B., G. Ekström, and A. M. Dziewoński
2008. Anisotropic shear-wave velocity structure of the earth's mantle: A global model. *Journal of Geophysical Research: Solid Earth*, 113(6):1–23.

Li, C., R. D. Van der Hilst, A. S. Meltzer, and E. R. Engdahl
2008. Subduction of the Indian lithosphere beneath the Tibetan Plateau and Burma. *Earth and Planetary Science Letters*, 274(1-2):157–168.

Lowrie, W.
2007. *Fundamentals of Geophysics*, 2nd edition. New York: Cambridge University Press.

Ludwig, W. J., J. E. Nafe, and C. L. Drake
1970. Seismic refraction. *The Sea*, 4(Wiley-Interscience):53–84.

Lüschen, E., C. Müller, H. Kopp, M. Engels, R. Lutz, L. Planert, A. Shulgin, and Y. S. Djajadihardja
2011. Structure, evolution and tectonic activity of the eastern Sunda forearc, Indonesia, from marine seismic investigations. *Tectonophysics*, 508(1-4):6–21.

Mansi, A. H., M. Reguzzoni, and D. Sampietro
2013. Subduction Plate Characterization from GOCE Gravity Gradients. In *American Geophysical Union, Fall Meeting 2013*, San Fransicso. Politecnico di Milano, DICA, Geomatics Laboratory.

Mansi, A. H., D. Sampietro, and M. Reguzzoni
2014. Exploiting along-track GOCE gravity gradients for the modeling of subduction plates. In *European Geosciences Union, General Assembly 2014*, volume 16, Vienna. Politecnico di Milano, DICA, Geomatics Laboratory.

Martinec, Z., K. Pěč, and M. Burša
1989. The Phobos gravitational field modeled on the basis of its topography. *Earth, Moon and Planets*, 45(3):219–235.

Mayer-Gürr, T.
2015. Conference presentation: The new combined satellite only model GOCO05s. In *European Geosciences Union, General Assembly*, Vienna.

McCaffrey, R.
2009. The Tectonic Framework of the Sumatran Subduction Zone. *Annual Review of Earth and Planetary Sciences*, 37(1):345–366.

McNeill, L. C. and T. J. Henstock
2014. Forearc structure and morphology along the Sumatra-Andaman subduction zone. *Tectonics*, 33(2):112–134.

Meinesz, F. A. V.
1931. By Submarine Through the Netherlands East Indies. *The Geographical Journal*, 77(4):338–348.

Meinesz, F. A. V.
1954. Indonesian Archipelago: A Geophysical Study. *Geological Society of America Bulletin*, 65(2):143.

Mikhailov, V., G. Pajot, M. Diament, and A. Price
2007. Tensor deconvolution: A method to locate equivalent sources from full tensor gravity data. *Geophysics*, 72(5):I61–I69.

Mikhailov, V., S. Tikhotsky, M. Diament, I. Panet, and V. Ballu
2004. Can tectonic processes be recovered from new gravity satellite data? *Earth and Planetary Science Letters*, 228(3-4):281–297.

Montagner, J. P. and B. L. Kennett
1996. How to reconcile body-wave and normal-mode reference earth models. *Geophysical Journal International*, 125(1):229–248.

Mooney, W. D. and M. K. Kaban
2010. The North American upper mantle: Density, composition, and evolution. *Journal of Geophysical Research*, 115(B12):B12424.

Müller, R. D., M. Sdrolias, C. Gaina, and W. R. Roest
2008. Age, spreading rates, and spreading asymmetry of the world's ocean crust. *Geochemistry, Geophysics, Geosystems*, 9(4):1–19.

Oruç, B.
2010. Depth Estimation of Simple Causative Sources from Gravity Gradient Tensor Invariants and Vertical Component. *Pure and Applied Geophysics*, 167(10):1259–1272.

Pail, R.
2012. GOCE gravity models. Technical report, Institude of Astronomical and Physical Geodesy, TU München.

Pail, R., S. Bruinsma, F. Migliaccio, C. Förste, H. Goiginger, W. D. Schuh, E. Höck, M. Reguzzoni, J. M. Brockmann, O. Abrikosov, M. Veicherts, T. Fecher, R. Mayrhofer, I. Krasbutter, F. Sansò, and C. C. Tscherning
2011. First GOCE gravity field models derived by three different approaches. *Journal of Geodesy*, 85(11):819–843.

Pail, R., T. Fecher, D. Barnes, J. F. Factor, S. A. Holmes, T. Gruber, and P. Zingerle
2016. The Experimental Gravity Field Model XGM2016. In *International Symposium on Gravity, Geoid and Height Systems 2016*, Thessaloniki. International Association of Geodesy.

Panning, M. and B. Romanowicz
2006. A three-dimensional radially anisotropic model of shear velocity in the whole mantle. *Geophysical Journal International*, 167(1):361–379.

Parsons, B. and J. G. Sclater
1977. An analysis of the variation of ocean floor bathymetry and heat flow with age. *Journal of Geophysical Research*, 82(5):803.

Pavlis, N. K. and R. H. Rapp
1990. The development of an isostatic gravitational model to degree 360 and its use in global gravity modelling. *Geophysical Journal International*, 100(3):369–378.

Pedersen, L. B. and T. M. Rasmussen
1990. The gradient tensor of potential field anomalies: Some implications on data collection and data processing of maps. *Geophysics*, 55(12):1558–1566.

Pesicek, J. D., C. H. Thurber, S. Widiyantoro, E. R. Engdahl, and H. R. DeShon
2008. Complex slab subduction beneath northern Sumatra. *Geophysical Research Letters*, 35(20):1–5.

Pesicek, J. D., C. H. Thurber, S. Widiyantoro, H. Zhang, H. R. DeShon, and E. R. Engdahl
2010. Sharpening the tomographic image of the subducting slab below Sumatra, the Andaman Islands and Burma. *Geophysical Journal International*, 182(1):no–no.

Richards, S., G. Lister, and B. L. N. Kennett
2007. A slab in depth: Three-dimensional geometry and evolution of the Indo-Australian plate. *Geochemistry, Geophysics, Geosystems*, 8(12):1–11.

Root, B. C., J. Ebbing, W. van der Wal, R. W. England, and L. L. A. Vermeersen
2017. Comparing gravity-based to seismic-derived lithosphere densities: A case study of the British Isles and surrounding areas. *Geophysical Journal International*, 208(3):1796–1810.

Root, B. C., P. Novák, D. Dirkx, M. K. Kaban, W. van der Wal, and L. L. A. Vermeersen
2016. On a spectral method for forward gravity field modelling. *Journal of Geodynamics*, 97:22–30.

Root, B. C., W. van der Wal, P. Novák, J. Ebbing, and L. L. A. Vermeersen
2014. Glacial isostatic adjustment in the static gravity field of Fennoscandia. *Journal of Geophysical Research: Solid Earth*, 120:503–518.

Rossi, L., A. H. Mansi, M. Reguzzoni, and D. Sampietro
2017. Poster Presentation: Gravity inversion of the Kermadec-Tonga subduction zone by GOCE data and seismic information. In *European Geosciences Union, General Assembly 2017*, Vienna. European Geosciences Union.

Rummel, R., R. H. Rapp, H. Suenkel, and C. C. Tscherning
1988. Comparisons of global topographic/isostatic models to the Earth's observed gravity field. Technical Report March, The Ohio State University & National Aeronautics and Space Administration (NASA), Columbus, Ohio, United States.

Sandwell, D. T.
2001. *Cooling of The Oceanic Lithosphere and Ocean Floor Topography*.

Scheidegger, A. E.
1982. *Principles of Geodynamics*. Berlin, Heidelberg: Springer Berlin Heidelberg.

Shulgin, A., H. Kopp, C. Mueller, E. Lueschen, L. Planert, M. Engels, E. R. Flueh, A. Krabbenhoeft, and Y. S. Djajadihardja
2009. Sunda-Banda arc transition: Incipient continent-island arc collision (northwest Australia). *Geophysical Research Letters*, 36(10):2–7.

Sieh, K.
2006. The Sunda Megathrust : Past, Present and Future. *Journal of Earthquake and Tsunami*, 1(1):1–17.

Sieh, K. and D. Natawidjaja
2000. Neotectonics of the Sumatran fault, Indonesia. *Journal of Geophysical Research: Solid Earth*, 105(B12):28295–28326.

Simoes, M., J. P. Avouac, R. Cattin, and P. Henry
2004. The Sumatra subduction zone: A case for a locked fault zone extending into the mantle. *Journal of Geophysical Research B: Solid Earth*, 109(10).

Stein, C. A. and S. Stein
1992. A model for the global variation in oceanic depth and heat flow with lithospheric age. *Nature*, 359(6391):123–129.

Stein, S. and C. A. Stein
2013. Thermo-Mechanical Evolution of Oceanic Lithosphere: Implications for the Subduction Process and Deep Earthquakes. In *Subduction: Top to Bottom*, Pp. 1–17. American Geophysical Union (AGU).

Steinberger, B. and T. W. Becker
2016. A comparison of lithospheric thickness models. *Tectonophysics*, Pp. 1–14.

Stern, R. J.
2002. Subduction zones. *Reviews of Geophysics*, 40(4).

Švarc, M., M. Herceg, and F. Cammarano
2016. Poster presentation: Subduction zones seen by GOCE gravity gradients. In *ESA Living Planet Symposium 2016*, Prague.

Szwillus, W.
2018. ESA 3D-Earth: Kriging Inpolated Crustal Thickness and Uncertainty Grids [online].

Tarr, A. C., H. M. Benz, R. L. Dart, A. Villaseñor, G. P. Hayes, K. P. Furlong, and S. Rhea
2010. Poster: Seismicity of the earth 1900–2007, Kuril-Kamchatka arc and vicinity: U.S. Geological Survey Open-File Report.

Toksöz, M. N. and M. Nafi
1975. The Subduction of the Lithosphere. *Scientific American*, 233(5):88–98.

Turcotte, D. L., D. C. McAdoo, and J. G. Caldwell
1978. An elastic-perfectly plastic analysis of the bending of the lithosphere at a trench. *Tectonophysics*, 47(3-4):193–205.

Turcotte, D. L. and G. Schubert
1982. *Geodynamics: Applications of Continuum Physics to Geological Problems*. New York: John Wiley.

Van Rossum, L., B. Root, and W. Van Der Wal
2018. Towards a 3D model of the Sumatra slab using combined gravity and gravity gradients constrained with seismic tomography. *Geophysical Research Abstracts*, 20(19690).

Vaníček, P., M. Najafi, Z. Martinec, L. Harrie, and L. E. Sjöberg
1995. Higher-degree reference field in the generalized Stokes-Helmert scheme for geoid computation. *Journal of Geodesy*, 70(3):176–182.

Vere-Jones, D.
1995. Forecasting earthquakes and earthquake risk. *International Journal of Forecasting*, 11(4):503–538.

Vermeersen, L. L. A.
2015. *AE3-E01: The Solid Earth – A Short Introduction [Lecture Notes]*. Delft: Delft University of Technology.

Watts, A. B.
2001. *Isostasy and Flexure of the Lithosphere*. New York: Cambridge University Press.

Watts, A. B. and M. Talwani
1975. Gravity Effect of Downgoing Lithospheric Slabs beneath Island Arcs. *GSA Bulletin*, 86(1).

Whittaker, J. M., A. Goncharov, S. E. Williams, R. D. Müller, and G. Leitchenkov
2013. Global sediment thickness data set updated for the Australian-Antarctic Southern Ocean. *Geochemistry, Geophysics, Geosystems*, 14(8):3297–3305.

Wilson, L.
2007. Planetary Volcanism. In *Encyclopedia of the Solar System*, Pp. 829–848. Elsevier.

Wu, J., J. Suppe, R. Lu, and R. Kanda
2016. Philippine Sea and East Asian plate tectonics since 52 Ma constrained by new subducted slab reconstruction methods. *Journal of Geophysical Research: Solid Earth*, 121(6):4670–4741.

Yadav, R.
2017. *3D Density Structure and Dynamics of Andaman Subduction Zone*. Doctoral thesis, National Geophysical Research Institute, Telangana, India.

Yu, J. H. and D. M. Zhao
2010. The gravitational gradient tensor's invariants and the related boundary conditions. *Science China Earth Sciences*, 53(5):781–790.

Zhang, Q., F. Guo, L. Zhao, and Y. Wu
2017. Geodynamics of divergent double subduction: 3-D numerical modeling of a Cenozoic example in the Molucca Sea region, Indonesia. *Journal of Geophysical Research: Solid Earth*, 122(5):3977–3998.

Zhao, D., T. Matsuzawa, and A. Hasegawa
1997. Morphology of the subducting slab boundary in the northeastern Japan arc. *Physics of the Earth and Planetary Interiors*, 102(96):89–104.